Characterization of the magnetic state of layered magnets using neutron diffraction and muon spin rotation

Daniel Potashnikov

Characterization of the magnetic state of layered magnets using neutron diffraction and muon spin rotation

Research Thesis

In Partial Fulfillment of The Requirements for the Degree of Master of Science in Physics

Daniel Potashnikov

Submitted to the Senate of the Technion - Israel Institute of Technology

Shvat 5782, Haifa, January 2022

This Research Thesis was done under the supervision of Professor Amit Keren in the Department of Physics and Dr. Oleg Rivin from the Nuclear Research Center Negev.

Parts of this work are available in the following list of publications.
Peer reviewed journals:

1. D. Potashnikov, E. N. Caspi, A. Pesach, Q. Tao, J. Rosen, D. Sheptyakov, H. A. Evans, C. Ritter, Z. Salman, P. Bonfa, T. Ouisse, M. Barbier, O. Rivin, and A. Keren. Magnetic structure determination of high-moment rare-earth-based laminates. *Phys. Rev. B*, 104(17):174440, 2021.

2. D. Potashnikov, E.N. Caspi, A. Pesach, S. Kota, M. Sokol, L.A. Hanner, M.W. Barsoum, H.A. Evans, A. Eyal, A. Keren, and O. Rivin. Magnetic properties of $(Fe_{1-x}Mn_x)_2AlB_2$ and the impact of substitution on the magnetocaloric effect. *Physical Review Materials*, 4(8):084404, 2020.

3. Q. Tao, J. Lu, M. Dahlqvist, A. Mockute, S. Calder, A. Petruhins, R. Meshkian, O. Rivin, D. Potashnikov, E.N. Caspi, H. Shaked, A. Hoser, C. Opagiste, R. Galera, R. Salikhov, U. Wiedwald, C. Ritter, A.R. Wildes, B. Johansson, L. Hultman, M. Farle, M.W. Barsoum, and J. Rosen. Atomically Layered and Ordered Rare-Earth i-MAX Phases: A New Class of Magnetic Quaternary Compounds. *Chemistry of Materials*, 31(7):2476-2485, 2019.

4. D. Potashnikov, E.N. Caspi, A. Pesach, A. Hoser, S. Kota, L. Verger, M.W. Barsoum, I. Felner, A. Keren, and O. Rivin. Magnetic ordering in the nanolaminar ternary Mn_2AlB_2 using neutron and X-ray diffraction. *Journal of Magnetism and Magnetic Materials*, 471:468474, 2019.

Conference proceedings:

1. D. Potashnikov, A. Pesach, E.N. Caspi, O. Rivin, Q. Tao, J. Rosen, D. Sheptyakov, H. Luetkens, P. Bonfa and A. Keren, The magnetic structure of a potentially 2D magnet explored by neutrons and muons. Talk given at the 66^{th} annual meeting of the Israel physical society, 2021.

2. D. Potashnikov, O. Rivin, A. Pesach, E.N. Caspi, A. Hoser, S. Kota and M.W. Barsoum. Magnetic Ordering Investigation in Mn_2AlB_2 using Neutron Diffraction. Talk given at the 14^{th} international ceramics congress, 2018.

3. D. Potashnikov, O. Rivin, A. Pesach, E.N. Caspi, A. Hoser, S. Kota and M.W. Barsoum. Magnetic ordering investigation in Mn_2AlB_2 using powder neutron diffraction. Talk given at the 18^{th} Israel materials engineering conference, 2018.

4. D. Potashnikov, O. Rivin, A. Hoser, S. Kota, M. Barsoum and E. Caspi. Magnetic ordering investigation in Mn_2AlB_2 using neutron diffraction. Poster presented at the 63^{rd} annual meeting of the Israel physical society, 2017.

Funding for this research was partially provided by the

PAZY grant.

Contents

List of Figures

List of Tables

Abstract

Functional magnetic materials are widely used in different applications which range from data storage, spintronics to magnetic refrigeration. In the future, the range of applications might extend and two-dimensional magnetic materials could be incorporated into Van der Waals based heterostructures. In this work, the magnetic ground states and properties of two families of layered magnetic materials are investigated using bulk as well as microscopic magnetic probes. Each of the two families studied in this work presents a separate topic.

The first family are the MAB phases – a class of ternary borides with the formula M_2AlB_2 where M is a transition metal. Interest in these phases spurred recently with the discovery of a near room temperature magnetocaloric effect in Fe_2AlB_2. Herein, the magnetic phase diagram of the $(Fe_{1-x}Mn_x)_2AlB_2$ solid solution is investigated using neutron diffraction and magnetization measurements. Three different ground states are found as function of x: a ferromagnetic state for $x \leq 0.1$, a canted antiferromagnetic state for $0.1 < x \leq 0.5$ and a simple antiferromagnetic state for $x > 0.5$. The observed phase diagram in the x–T plane is qualitatively reproduced using a mean field calculation. Addition of Mn into the solution is found to decrease the magnetocaloric effect but broaden its temperature range, thus enabling control and tuning of its relative cooling power. Introduction to the MAB phases is given in section 1.1 while results and analysis are given in chapter 5.

The second family of materials are the rare-earth containing i-MAX phases. These are a family of layered ceramics with the formula $(Mo_{2/3}RE_{1/3})_2AlC$, where RE is a rare-earth. These are newly discovered materials which serve as potential parent compounds for 2D derivatives. The magnetic ground states of $(Mo_{2/3}RE_{1/3})_2AlC$ with RE = Nd, Tb, Ho and Er are identified as transverse spin density waves using neutron powder diffraction, however the same technique cannot be used on RE = Gd as it is a strong neutron absorber. Muon spin rotation measurements on these compounds with the addition of RE = Gd reveal that only in RE = Nd or Gd the magnetic moments are static over a time scale of a few µs. The possible magnetic structures of RE = Gd are obtained by combining muon spin rotation results with (DFT) based muon site calculations, magnetic symmetry analysis and neutron diffraction results on sister compounds. Two possible magnetic configurations for RE = Gd are found with a magnetic moment of $6.5 \pm 0.5\,\mu_B$ at 1.5 K. Analysis of the temperature dependence of the magnetization gives a ratio of $\approx 10^{-9}$ between out-of-plane and in-plane interaction energies, thus identifying the RE = Gd compound as a nearly two dimensional antiferromagnet. Thus, RE = Gd is identified as the best candidate for providing a high moment 2D magnet from the currently available i-MAX compounds. Background information on the i-MAX phases is given in section 1.2 while results and analysis are given in chapter 6.

Symbols and Abbreviations

Abbreviations

μSR	Muon spin rotation
AFM	Antiferromagnetism / Antiferromagnetic
BT	Base temperature
DFT	Density functional theory
FM	Ferromagnetism / Ferromagnetic
MC	Magnetocaloric
MFT	Mean field theory
NPD	Neutron powder diffraction
PM	Paramagnet
RCP	Relative cooling power
RT	Room temperature
SBMFT	Schwinger boson mean field theory
SDW	Spin density wave
TM	Transition metal
XRD	X-ray diffraction

Symbols

β	Inverse temperature
$\beta_{\vec{k},\sigma}$	Bogoliubov operators
χ_D	Character of representation D
Δ	Variational gap parameter
$\frac{d\sigma}{d\Omega}$	Differential scattering cross section
Γ	Magnetic representation
γ_n, γ_μ	Neutron, muon gyromagnetic ratios
$\gamma_{\vec{k}}$	Band dispersion
Λ	Molecular field constant
λ	X-ray or neutron wavelength

$\mathbb{J}$	Total angular momentum
$\mathbb{L}$	Orbital angular momentum
$\mathbb{S}$	Scattering function
$\mathcal{F}_{hkl}$	Structure factor
$\mathcal{G}$	Gibbs free energy
$\mathcal{P}$	Projection operator
$\mathcal{R}$	Point group symmetry element
$\mathcal{S}$	Entropy
$\mathcal{T}$	Kinetic energy
$\mathcal{Z}$	Partition function
μ_B	Bohr magneton
μ_N	Nuclear magneton
ω	Energy transfer / Larmor frequency
$\omega_{\vec{k}}$	Spin wave dispersion relation
ρ	Electronic density
σ	Neutron scattering cross section
ϱ	Density of states
$\vec{\delta}$	Nearest neighbor / atomic position
$\vec{\kappa}$	Momentum transfer / scattering vector
$\vec{a}, \vec{t}, \vec{l}$	Lattice translation vector
$\vec{a}^*$	Reciprocal lattice vector
$\vec{B}$	Magnetic field
$\vec{k}, \vec{q}$	Lattice momentum / propagation vector
$\vec{Q}_\perp$	Magnetic interaction operator
ξ	Magnetic correlation length
$A(t)$	Muon asymmetry
b	Nuclear scattering length
$b_\uparrow, b_\downarrow$	Schwinger boson operator

c	Spin wave velocity
$C(T,h)$	Specific heat
D	Linear representation of a group
d_{hkl}	Interplane distance
E	Energy
e	Electron charge
F	Helmholtz free energy
$f(\vec{k})$	Electronic form factor
g	g-factor
$G_{\vec{k}}$	Propagation vector group / Little group of $\vec{k}$
H	Hamiltonian
h	Magnetic field strength
J	Exchange interaction
L	Lorentz factor
m_e	Electron mass
m_n	Neutron mass
m_{hkl}	Reflection multiplicty
N	Number of lattice sites / nuclei
$n_{\vec{k}}$	Bose occupation number
P	Muon polarization
Q	Heat
R	Atomic / nuclear position
S	Atomic spin
T	Temperature
V	Potential energy
W	Debeye-Waller factor
x	Concentration
Z	Atomic number
z	Coordination number

1 Introduction

1.1 The M_2AlB_2 compounds

The M_2AlB_2 compounds (M = Fe, Mn, Cr) belong to a family of ternary and quaternary transition metal (TM) borides which are called MAB phases [1]. They crystallize in the orthorhombic $Cmmm$ space group with the M, Al and B atoms occupying the $4j$, $2a$ and $4i$ sites, respectively (Figure 1.1). The unit cell contains two formula units which form layers of MB slabs separated by layers of Al.

Although these compounds were discovered during the 60's and 70's [2–4], they remained unexplored until recent years. Interest in the M_2AlB_2 was spurred with the discovery of room temperature (RT) ferromagnetism (FM) in Fe_2AlB_2 in 2011 [5]. Since Fe_2AlB_2 is composed of cheap and abundant elements and is FM below RT, it was seen as a potential material for magnetic refrigeration based on the magnetocaloric (MC) effect [6].

Initial magnetization measurements on arc melted Fe_2AlB_2 have resulted in an MC effect (adiabatic temperature change, see Sec. 3) of $\approx 2\,\mathrm{K}$ under an applied field of 2 T [6], with much more magnetic studies performed on differently synthesized samples (see Ref. [1] and references therein). In an attempt to find ways of influencing the magnetic properties of Fe_2AlB_2, additional studies were performed on other M_2AlB_2 compounds including $(Fe_{1-x}Mn_x)_2AlB_2$ ($0 \leq x \leq 1$) [7, 8], $(Fe_{1-x}Co_x)_2AlB_2$ ($0 \leq x \leq 0.3$) [9], and $Fe_2Al_{1.2-x}(Ge,Ga)_xB_2$ [10]. The admixture of Mn or Co into the M site was shown to decrease the transition temperature down to 43 K for 60% Mn, while addition of Ga and Ge into the Al site yielded more than a two-fold increase in the adiabatic temperature change.

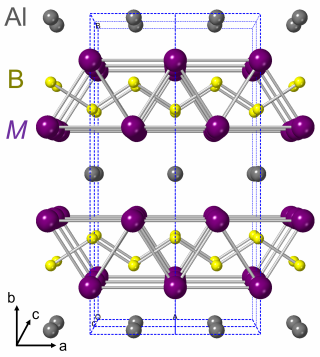

Figure 1.1: The layered structure of M_2AlB_2 (space group $Cmmm$).

Despite the numerous magnetization studies on Fe_2AlB_2, its magnetic structure was not known for a few years until it was observed by neutron powder diffraction (NPD) in 2016 [11]. It was found to be FM with a magnetic moment of $\approx 1.4\,\mu_B$ directed along the a axis. This result agreed with density functional

theory (DFT) calculations [12] which showed that the a axis is the easy axis in Fe_2AlB_2 and that the magnetic moment originates from a large spin polarization of the density of states at the Fermi level [7].

DFT calculations [12] have also predicted that Mn_2AlB_2 is antiferromagnetic (AFM) and that for $x > 0.2$ the ground state of $(Fe_{1-x}Mn_x)_2AlB_2$ changes from a FM to an AFM. AC susceptibility measurements of $(Fe_{1-x}Mn_x)_2AlB_2$ [8] as function of temperature have shown indications of a spin-glass state at $T_p \approx 40\,\mathrm{K}$ for $x = 0.25$. It was postulated that AFM interactions induced by the addition of Mn atoms, and the triangular arrangement of the M atoms in the ab plane (Figure 1.1) gives rise to frustration in the system. An additional magnetization study combined with DFT calculations of $(Fe_{0.5}Mn_{0.5})_2AlB_2$ has suggested that it is a disordered ferrimagnet [13] however the magnetic states of $(Fe_{1-x}Mn_x)_2AlB_2$ for any $x > 0$ have not yet been directly observed.

In this work we have set to investigate the magnetic phase diagram of $(Fe_{1-x}Mn_x)_2AlB_2$ in the x–T plane using NPD and magnetization measurements. The obtained results are analyzed in the framework of mean field theory (MFT). Finally, the impact of Mn substitution on the MC effect is analyzed, and possible ways to control the MC properties of the $(Fe_{1-x}Mn_x)_2AlB_2$ system are discussed.

Experimental details and a summary of this work can be found in Ref. [14] and [15], while the results are presented in Sec. 5. This work gives the first direct observation of the magnetic structure of Mn_2AlB_2 and its solid solutions, which was hypothesized but never observed, using NPD. The agreement between experiment and theory confirms the validity of DFT calculations on the $(Fe_{1-x}Mn_x)_2AlB_2$ system. Measurement of the MC properties of the solid solution adds to the growing database of MC materials [16], which will help in designing a working magnetic-cooling based refrigerator.

1.2 Rare earth based i-MAX phases

MAX phases [17] are a family of ternary carbides and nitrides with the genral formula $M_{n+1}AX_n$, where M is a metal, A is an A-group element (Al, Ge, Ga, Sn, etc...) and X is C or N with n ranging from 1 to 3. With over 150 variants [18] discovered as of recently, these compounds combine properties of metals and ceramics [19] and can serve as parent compounds for two dimensional derivatives called MXenes (graphene analog) [20].

While multiple M or A atoms can be introduced to create quaternary MAX phases, most of these phases form solid solutions and are thus chemically disordered. An exception to this rule is the newly discovered sub-group of MAX phases with in-plane chemical ordering, which is termed i-MAX [21]. Unlike regular MAX phases, where M is usually a transition metal, i-MAX phases with the formula $\left(Mo_{2/3}RE_{1/3}\right)_2AlC$ (also known as RE-i-MAX) where RE is a rare-earth have been synthesized [22]. The complex interactions between localized $4f$ electrons of the RE ion with delocalized d electrons give rise to varying magnetic properties in the RE-i-MAX phases [22].

The RE-i-MAX phases crystallize in the monoclinic $C2/c$ space group with

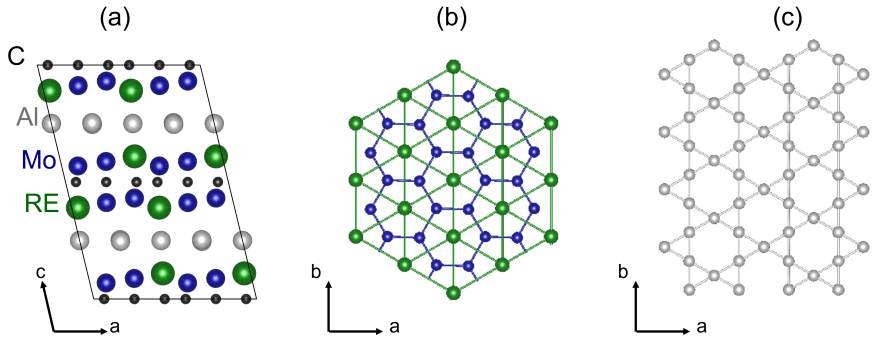

Figure 1.2: (a) Unit cell of $\left(Mo_{2/3}RE_{1/3}\right)_2 AlC$ projected in the a-c plane. (b) A projection of a single Mo-RE layer in the a-b plane. (c) A projection of a single Al layer in the a-b.

the RE occupying the $8j$ site [Figure 1.2(a)]. The Mo atoms are situated on a honeycomb lattice [Figure 1.2(b)], the RE atoms - on a triangular lattice, and the Al atoms form Kagomé-like patterns [Figure 1.2(c)]. Through the concept of "targeted etching", 2D sheets can be tailored to retain one or both of the M elements (RE and Mo) [23]. Since the chemical order is retained in the derived MXene, this makes RE-i-MAX phases potential parent materials for 2D magnetic sheets with high magnetic moments ($> 5\,\mu_B$) available from RE-based materials.

However, not much is known on the magnetic structure of the parent compounds, let alone on the potential 2D sheets. Temperature and field dependent magnetization and specific heat measurements [22] on $\left(Mo_{2/3}RE_{1/3}\right)_2 AlC$ have shown that most compounds are magnetically ordered with transition temperatures ranging from 3.6 K for RE = Er up to 28 K for RE = Tb. Curie-Weiss plots of inverse susceptibility versus temperature gave negative Weiss temperatures suggesting that the magnetic coupling is AFM. NPD measurements on samples with RE = Tb and Er [22] confirmed a spin density wave mangetic structure (SDW, see Figure 3.1) in these compounds.

In this work, the magnetic ground states of bulk $\left(Mo_{2/3}RE_{1/3}\right)_2 AlC$ with RE = Nd, Gd, Tb, Dy, Ho, and Er are explored using muon spin rotation (μSR). The series is also examined with NPD, excluding RE = Gd since it is a strong neutron absorber. From NPD, it is found that all compounds except RE = Gd develop transverse SDW magnetic ordering with their propagation vector directed along the b axis. Using DFT based muon site calculations, symmetry analysis, and information from the neutron data on RE = Nd, Tb, Ho, and Er, the magnetic structure of RE = Gd is also determined to be a simple AFM with an extremely small anisotropy ratio ($< 10^{-8}$) between out-of-plane and in-plane coupling. Moreover, only RE = Nd and Gd exhibit long-range static magnetic

order within the μSR time window (10 μsec). For the other REs, the magnetic order fluctuates on a time scale that is longer than the typical neutron scattering window of 10^{-12} s but shorter than the μSR time window. These fluctuations are observed down to a temperature of 1.5 K.

Experimental details and a summary of this work can be found in Ref. [22] and [24], while the results are presented in Sec. 6. This work gives the first observation and characterization of the magnetic structures of the newly discovered $\left(\mathrm{Mo}_{2/3}\mathrm{RE}_{1/3}\right)_2\mathrm{AlC}$ phases using NPD. In addition, a non-standard method of determining a magnetic structure using μSR measurements alone is presented for RE = Gd. Without this method, the magnetic structure of RE = Gd would have probably taken a long time to solve due to the difficulty in measuring Gd containing compounds using NPD. The identification of RE = Gd as the best candidate for deriving a 2D magnetic material will hopefully help focus future research on magnetic RE-based MXenes.

2 Research objectives

2.1 The M_2AlB_2 compounds

Research objectives in studying the $(Fe_{1-x}Mn_x)_2\,AlB_2$ system were the following:

a. Determine the magnetic phase diagram of $(Fe_{1-x}Mn_x)_2\,AlB_2$ as function of temperature T and Mn concentration x in the range $0 \leq x \leq 1$.

b. Measure magnetic properties of $(Fe_{1-x}Mn_x)_2\,AlB_2$ for different values of x and suggest how the solid solution can improve the magnetocaloric properties of Fe_2AlB_2.

2.2 Rare earth based *i*-MAX phases

Research objectives in the study of $\left(Mo_{2/3}RE_{1/3}\right)_2\,AlC$ compounds were the following:

a. Observe the magnetic structures of $\left(Mo_{2/3}RE_{1/3}\right)_2\,AlC$ phases.

b. Determine which RE based i-MAX phase has the highest potential to produce a 2D magnet.

3 Theory

3.1 Crystal structure and space groups

A general translation operator in the crystalline phase is given by

$$\vec{t} = \sum_{i=1}^{3} n_i \vec{a}_i, \tag{3.1}$$

where i labels different crystal directions, n_i are integers and $\vec{a}_i$ are lattice vectors. These discrete sets can be classified into 14 lattices called Bravais lattices [25]. Combining the 14 Bravais lattices with one of the 32 crystallographic point groups gives rise to 230 crystallographic space groups, which represent the possible symmetries of crystals [25]. A symmetry element of a space group is denoted by $\left\{\mathcal{R} \,|\, \vec{t}\right\}$, where $\mathcal{R}$ is a point group element.

Consider a single particle Hamiltonian in a periodic potential

$$H = -\frac{\hbar^2}{2m}\nabla^2 + V\left(\vec{r}\right). \tag{3.2}$$

If V has the periodicity of the lattice, then H commutes with all elements $\left\{\mathcal{R} \,|\, \vec{t}\right\}$ of the space group. This gives us a set of quantum numbers, which can be used to label the eigenstates of H [26]. In particular, if we consider only the translation elements $\left\{I \,|\, \vec{t}\right\}$, where I is the identity element, then we find that the wavefunctions can be labeled by vectors $\vec{k}$ with the corresponding eigenstates having the form of Bloch waves [27]

$$\Psi_{\vec{k}}\left(\vec{r}\right) = u_{\vec{k}}\left(\vec{r}\right) e^{-i\vec{k}\cdot\vec{r}}, \tag{3.3}$$

where $u_{\vec{k}}\left(\vec{r}-\vec{t}\right) = u_{\vec{k}}\left(\vec{r}\right)$. It is customary to introduce the reciprocal lattice, which is defined by three vectors $\vec{a}_i^*$ defined by

$$\vec{a}_i \cdot \vec{a}_j^* = 2\pi\delta_{ij}. \tag{3.4}$$

Following (3.1) a general vector in the reciprocal lattice is then defined by

$$\vec{q} = \sum_{i=1}^{3} m_i \vec{a}_i^*, \tag{3.5}$$

where m_i are integers. The action of a point group element $\left\{\mathcal{R} \,|\, \vec{0}\right\}$ on a general lattice vector $\vec{t}$ gives the vector $\mathcal{R}\vec{t}$, which itself is another lattice vector. Using (3.1), (3.4), (3.5) and the trasnformation properties of $\vec{t}$, one can show that the effect of $\mathcal{R}$ on a reciprocal lattice vector is

$$\left\{\mathcal{R}|\vec{0}\right\}\vec{q} = \mathcal{R}^{-1}\vec{q} \tag{3.6}$$

.

3.2 Magnetic structures

A magnet [27, 28] is a material in which some of the atoms possess a non-zero magnetic moment. The magnetic moment of an atom comes from the spin and angular momenta of its electrons. In a paramagnet (PM), the magnetic moments fluctuate randomly resulting in no average magnetic moment. However, in the presence of interactions between magnetic moments, the magnetic moment can become correlated producing a regular periodic configuration within the material. Such a periodic configuration is called a magnetic structure (Figure 3.1). The periodicity of the magnetic structure need not be the same as the under-

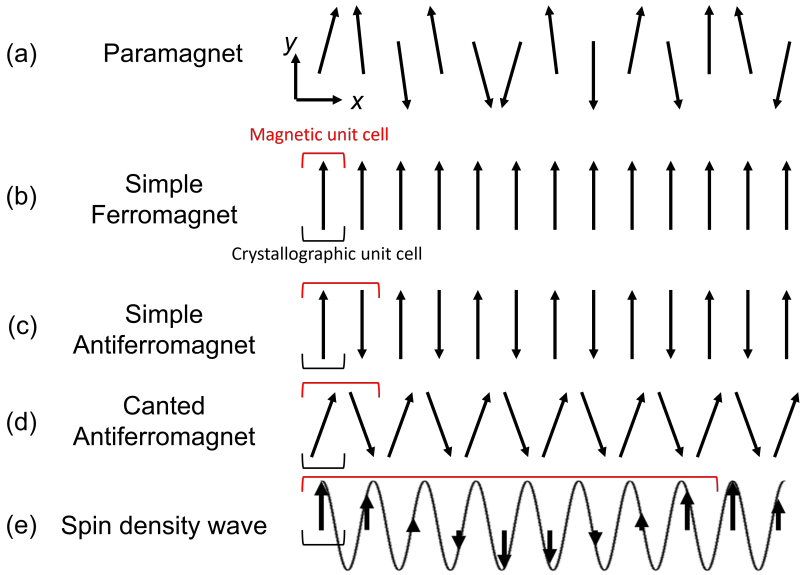

Figure 3.1: Examples of different magnetic structures (a) Paramagnet, (b) a simple ferromagnet, (c) a collinear antiferromagnet, (d) a canted antiferromagnet and (e) a spin density wave. Black square braces show the crystallographic unit cell while red braces show the magnetic unit cell in each type of structure.

lying crystallographic lattice. If the magnetic unit cell, the smallest repeating unit of the magnetic structure, coincides with an integer number of crystallographic unit cells, the magnetic structure is said to be commensurate with the crystal structure, otherwise it is incommensurate. If all the magnetic moments are parallel to each other, the structure is said to be collinear, otherwise it is called non-collinear.

Examples of collinear commensurate magnetic structures include a simple FM [Figure 3.1(b)] where all magnetic moments are parallel to each other and a simple AFM (also known as a Néel state) where the moments alternate between parallel and anti-parallel orientations [Figure 3.1(c)]. In the former case, the magnetic unit cell is equal to the crystallographic unit cell while in the latter

case, the magnetic unit cell is twice as large as the crystallographic unit cell. Simple FM and AFM structures are commonly found in transition metals and their compounds such as Fe, Ni, MnO and Cr_2O_3 [27]. An example of a non-collinear commensurate structure is the canted AFM [Figure 3.1(d)], where the structure is a combination of a simple FM along the x direction and a simple AFM along the y direction. An example of an incommensurate magnetic structure is the SDW [Figure 3.1(d)]. In the simplest case of a SDW, the magnitude of the magnetic moment is given by $m_0 \cos(kx)$, where m_0 is the SDW amplitude and k is the spacial frequency. Such magnetic configurations were observed for metallic Er and Tm [29].

In general, a magnetic structure can be described by specifying the x, y and z components of the spin operator[1] $\vec{S}_i$ on each magnetic site i. Since the periodicity of the magnetic structure can differ from the crystal periodicity, it is best to describe the magnetic structure in terms of its Fourier components

$$\vec{S}_{\vec{k}} = \sum_{i=1}^{N} \vec{S}_i e^{i\vec{k}\cdot\vec{r}}. \tag{3.7}$$

In this description, $\vec{S}_k$ are the analogues of the Bloch waves which appeared in (3.3) and the vectors $\vec{k}$, for which the Fourier component is non-zero, are called the propagation vectors of the magnetic structure. This description uses the reciprocal lattice to describe the magnetic structure in terms of its periodicites instead of specifying the magnetic moment on each direct lattice point. To describe the formation of magnetic structures and calculate their properties we shall introduce a general two-spin Hamiltonian. The energy of a periodic system with many spins can generally be written up to second order as

$$H\left(\left\{\vec{S}_i\right\}\right) = E_0 + \mu_B \sum_{i=1}^{N} \vec{B}^T \overleftrightarrow{g} \vec{S}_i - \frac{1}{2} \sum_{i,j} \vec{S}_i^T \overleftrightarrow{J} (\vec{r}_i - \vec{r}_j)\, \vec{S}_j, \tag{3.8}$$

where $\leftrightarrow$ is used to denote a matrix and T stands for transpose. The first term is a constant shift to the total energy and can be ignored, the second term describes the interaction of the spins with a constant external field and the third term describes the interaction between pairs of spins. While the atomic g-factor is a scalar that depends on the atomic type (see Sec. 4.4.2), some effective Hamiltonians [30–32] can result in anisotropic g-factors and therefore it is written as a matrix in (3.8) to represent the general case. The sign of the third term is chosen such that the system prefers an FM ordering for $J > 0$ and an AFM ordering for $J < 0$. For a periodic system, the interaction J depends only on the relative coordinate $\vec{\delta} \equiv \vec{r}_i - \vec{r}_j$. This enables us to simplify (3.8) by inserting the Fourier components (3.7)

$$H\left(\left\{\vec{S}_{\vec{k}}\right\}\right) = \mu_B \vec{B}^T \overleftrightarrow{g} \vec{S}_{\vec{0}} - \frac{1}{2N} \sum_{\vec{k}} \vec{S}_{\vec{k}}^T \overleftrightarrow{J}_{\vec{k}} \vec{S}_{-\vec{k}}, \tag{3.9}$$

[1] In the following we shall assume that the magnetic moment comes entirely from the spin angular momentum. This is common in transition metals where the angular momentum is quenched by the crystalline electric field [27].

where we have defined

$$\overleftrightarrow{J}_{\vec{k}} = \sum_{\vec{\delta}} \overleftrightarrow{J}\left(\vec{\delta}\right) e^{i\vec{k}\cdot\vec{\delta}} \tag{3.10}$$

and $\vec{\delta}$ runs over the relative positions of relevant pairs (i,j).

3.3 Magnetic symmetry and representation theory

In addition to translational invariance, Hamiltonian (3.8) is invariant under all symmetry operations of the crystallographic space group (when no external field is present). We can find the eigenstates of this Hamiltonian by using its symmetry properties [26]. From (3.3), the propagation vector is a good quantum number to label the eigenstates of (3.9). From the second term in (3.9) we see that the ground state of (3.8) will have a propagation vector that corresponds to the smallest component $J_{\vec{k}}^{\alpha\beta}$. For a Hamiltonian with periodic boundary conditions, the vectors $\vec{k}$ all lie in the first Brillouin zone – the unique primitive unit cell of the reciprocal lattice. After determining the propagation vector of the ground state, we need to determine the possible magnetic configurations $u_{\vec{k}}\left(\vec{r}\right)$ in (3.3). For this we define the propagation vector group (also known as little group of $\vec{k}$) $G_{\vec{k}}$ as the group containing all point group elements $\left\{\mathcal{R}|\vec{0}\right\}$ which leave $\vec{k}$ invariant or transform it (via (3.6)) into an equivalent vector $\vec{k}+\vec{q}$, where $\vec{q}$ is a reciprocal lattice vector

$$G_{\vec{k}} = \left\{\mathcal{R}\left|\mathcal{R}^{-1}\vec{k} = \vec{k}+\vec{q}\right.\right\}. \tag{3.11}$$

A linear representation D of a group G is a homomorphism given by [26]

$$\begin{aligned} D: \quad & G \to \mathrm{GL}\left(n,\mathbb{C}\right) \\ \forall \mathfrak{g}_1,\mathfrak{g}_2 \in G \quad & D\left(\mathfrak{g}_1\right) \bullet D\left(\mathfrak{g}_2\right) = D\left(\mathfrak{g}_1 * \mathfrak{g}_2\right), \end{aligned} \tag{3.12}$$

where $\mathrm{GL}\left(n,\mathbb{C}\right)$ is the general linear group of complex $n\times n$ matrices, $\mathfrak{g}$ denotes the elements of G, $*$ and $\bullet$ denote group multiplication in G and $\mathrm{GL}\left(n,\mathbb{C}\right)$, respectively. Linear representations are used to define the effect of group elements of G on wavefunctions, such as (3.3). A representation is called *reducible* when all elements of $D\left(\mathfrak{g}\right)$ can be trasnformed to have a block diagonal form, with blocks of the same size, otherwise it is called *irreducible*. Once $G_{\vec{k}}$ is known, the possible magnetic ground states with propagation vector $\vec{k}$ correspond to the irreducible representations of $G_{\vec{k}}$. An important property of representations is that wavefunctions, which transform under symmetry opeartors of G, by the same irreducible representation are degenerate. To find how a given representation can be decomposed into the irreducible representations of G we define the character [26] of a representation as

$$\chi_D\left(\mathfrak{g}\right) = \mathrm{Tr}\left[D\left(\mathfrak{g}\right)\right]. \tag{3.13}$$

We can define an inner product for characters via

$$\{\chi_{D_1}, \chi_{D_2}\} \equiv \frac{1}{|G|} \sum_{\mathfrak{g} \in G} \chi^*_{D_1}(\mathfrak{g}) \chi_{D_2}(\mathfrak{g}), \tag{3.14}$$

where $|G|$ denotes the number of elements in G. If D_1 and D_2 are irreducible representations, then $\{\chi_{D_1}, \chi_{D_2}\} = \delta_{D_1,D_2}$. A general representation D will decompose into irreducible representations D_i in the following form

$$D = \alpha_1 D_1 \oplus \cdots \oplus \alpha_m D_m \qquad \alpha_i = \{\chi_D, \chi_{D_i}\}. \tag{3.15}$$

To find the wavefunctions, which transform according to an irreducible representation D_i, we construct the projection operators

$$\mathcal{P}_i = \frac{d_i}{|G|} \sum_{\mathfrak{g} \in G} \chi^*_{D_i}(\mathfrak{g}) D(\mathfrak{g}), \tag{3.16}$$

where d_i is the dimension of D_i. By acting with $\mathcal{P}_i$ on a general wavefunction v we can project out the basis function $w = \mathcal{P}_i v$, which is an eigenstate of the Hamiltonian and transforms according to the irreducible representation D_i.

3.4 Mean-field theory of magnetism

To calculate thermodynamic properties of a Hamiltonian such as (3.8), we need to calculate the partition function

$$\mathcal{Z} = \mathrm{Tr}\left[e^{-\beta H}\right]. \tag{3.17}$$

Mean field theory [33] is an approximation that allows to convert a many body Hamiltonian into an effective single particle Hamiltonian. The approximation involves replacing the interaction term in (3.8) by $\vec{S}_i \overleftrightarrow{J}_{ij} \left\langle \vec{S} \right\rangle$, where $\langle\rangle$ denotes thermal averaging and is defined by

$$\left\langle \vec{S} \right\rangle = \mathrm{Tr}\left[\vec{S}_i \frac{e^{-\beta H}}{\mathcal{Z}}\right]. \tag{3.18}$$

The thermal average of a spin is related to the magnetization via

$$\vec{M} = -\mu_{\mathrm{B}} \overleftrightarrow{g} \left\langle \vec{S} \right\rangle, \tag{3.19}$$

where the negative sign comes from the negative charge of the electron. The resulting effective Hamiltonian describes a single spin in a mean field, and is given by

$$H^{\mathrm{MF}} = \mu_{\mathrm{B}} \vec{S}^T \overleftrightarrow{g} \vec{B}^{\mathrm{eff}}, \tag{3.20}$$

where the effective magnetic field is defined by [32]

$$\vec{B}^{\mathrm{eff}} = \vec{B} + \overleftrightarrow{\Lambda} \vec{M} \qquad \overleftrightarrow{\Lambda} = (\mu_{\mathrm{B}} \overleftrightarrow{g})^{-1} \left(\sum_c z_c \overleftrightarrow{J}_c \right) (\mu_{\mathrm{B}} \overleftrightarrow{g})^{-1}. \tag{3.21}$$

To obtain the mean field coefficient $\overleftrightarrow{\Lambda}$ in (3.21), we have re-written the sum over j in (3.8) as a sum over coordination shells c. Each coordination shell has z_c nearest neighbors with interaction strength $\overleftrightarrow{J}_c$. Using the definition of magnetization (3.19) together with (3.18), (3.20) and (3.21) we obtain the self-consistent equations for the magnetization

$$\vec{M} = \mu_{\mathrm{B}} \overleftrightarrow{g} S \mathrm{B}_S \left(\beta \mu_{\mathrm{B}} \left| \overleftrightarrow{g} \vec{B}^{\mathrm{eff}} \right| S \right) \frac{\overleftrightarrow{g} \vec{B}^{\mathrm{eff}}}{\left| \overleftrightarrow{g} \vec{B}^{\mathrm{eff}} \right|}, \tag{3.22}$$

where B_S is the Brillouin function defined by [33]

$$\mathrm{B}_S(x) \equiv \frac{2S+1}{2S} \coth\left(\frac{2S+1}{2S} x \right) - \frac{1}{2S} \coth\left(\frac{1}{2S} x \right). \tag{3.23}$$

3.5 Magnetocaloric effect

The MC effect refers to the adiabatic temperature change that results from the heating or cooling of a magnet under an application of an external field [34]. The thermodynamics of the MC cycle are depicted in Figure 3.2. The total entropy contains three contributions: the magnetic entropy, the lattice entropy and the electronic entropy

$$\mathcal{S}_{\mathrm{tot}}(T,h) = \mathcal{S}_m(T,h) + \mathcal{S}_{\mathrm{lat}}(T) + \mathcal{S}_{\mathrm{el}}(T). \tag{3.24}$$

A classical magnetic refrigeration Carnot cycle [16] consists of four steps: (a) an adiabatically applied field h_1 increases the temperature of the magnet from T_1 to T_2, (b) the system exchanges heat with a hot sink $Q_{\mathrm{hot}} = T_2 \Delta \mathcal{S}_m(T_2)$, (c) as the field is decreased back to h_0 the magnet is cooled back to T_1, (d) the system absorbs heat from the cold sink $Q_{\mathrm{cold}} = T_1 \Delta S_m(T_1)$. The characteristics of the MC effect can be obtained from the magnetization and its specific heat. The total entropy of the system can be calculated from [34]

$$\mathcal{S}_{\mathrm{tot}}(T,h) = \mathcal{S}_0 + \int_0^T \frac{C(T',h)}{T'} dT'. \tag{3.25}$$

Then $\Delta \mathcal{S}_m(T)$ and $\Delta T_{\mathrm{ad}}(T)$ can be obtained from the plot of $\mathcal{S}_{\mathrm{tot}}$ for different fields, as depicted in Figure 3.2. Alternatively, $\Delta \mathcal{S}_m$ and ΔT_{ad} can be directly expressed in terms of magnetization and heat capacity as

$$\Delta \mathcal{S}_m(T,h) = \int_0^h \left(\frac{\partial M}{\partial T} \right)_{h'} dh' \tag{3.26}$$

$$\Delta T_{\mathrm{ad}}(T,h) = -\int_0^h \frac{T}{C(T,h')} \left(\frac{\partial M}{\partial T} \right)_{h'} dh'. \tag{3.27}$$

The full derivation of these formulas is given in appendix A. In ferromagnets $\partial M / \partial T < 0$ near the transition temperature, therefore $\Delta \mathcal{S}_m$ is negative while

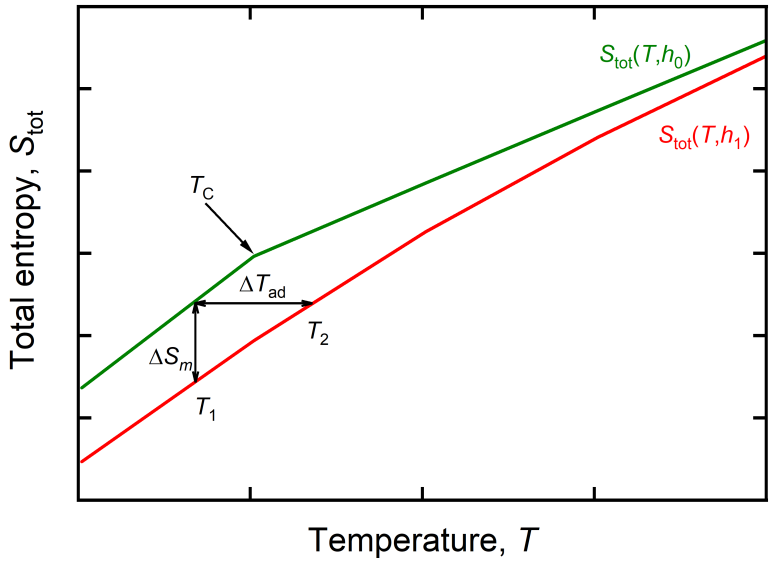

Figure 3.2: The $\mathcal{S}$–T diagram of a ferromagnet near its magnetic transition. The lines represent the total entropy at zero field $h_0 = 0$ and a finite field $h_1 > h_0$. The arrows represent the adiabatic temperature change ($\Delta T_{\rm ad}$) and isothermal entropy change ($\Delta \mathcal{S}_m$).

$\Delta T_{\rm ad}$ is positive. Furthermore, since $|\partial M/\partial T|$ is largest at the critical temperature (T_C), $\Delta \mathcal{S}_m$ peaks at the magnetic transition. Although the same can not be said about $\Delta T_{\rm ad}$, since the specific heat is also anomalous at T_C, it can be shown [35] that $\Delta T_{\rm ad}$ peaks at T_C for small fields. From this analysis, a magnetic refrigerator which works well at RT requires a material with a magnetic transition near RT.

3.6 Density functional theory

Density functional theory [36] is a method for claculating approximate solutions to the general many-body electronic Hamiltonian (3.28)

$$\hat{H} = \sum_{i=1}^{N_e} \frac{\hat{\vec{p}}_i^2}{2m_e} + \sum_{I=1}^{N_I} \frac{\hat{\vec{P}}_I^2}{2M_I} + \frac{1}{2}\sum_{i\neq j} \frac{e^2}{\left|\hat{\vec{r}}_i - \hat{\vec{r}}_j\right|} - \sum_{i,I} \frac{Z_I e^2}{\left|\hat{\vec{r}}_i - \hat{\vec{R}}_I\right|} + \frac{1}{2}\sum_{I\neq J} \frac{Z_I Z_J e^2}{\left|\hat{\vec{R}}_I - \hat{\vec{R}}_J\right|} \tag{3.28}$$

$$= \hat{\mathcal{T}}_e + \hat{\mathcal{T}}_I + \hat{V}_{ee} + \hat{V}_{eI} + \hat{V}_{II}, \tag{3.29}$$

where N_e and N_I are the number of electrons and positive ions, respectively, m_e is the electron mass, M_I is the mass of the I'th ion, e is the electron charge,

Z_I is the atomic number of the I'th ion, $\hat{\vec{p}}_i$ and $\hat{\vec{r}}_i$ are the momentum and position operators of the i'th electron and $\hat{\vec{P}}_I$ and $\hat{\vec{R}}_i$ are the momentum and position operators of the I'th ion. In this section, we denote operators using a hat to distinguish them from ordinary numbers. Since the mass of the ions is much larger than the mass of the electron, the ions can be considered as static which leads to the Born-Oppenheimer approximation $\hat{\vec{P}}_I = 0$ [36]. This, in turn, transforms $\hat{\vec{R}}_I$ from an operator into a regular vector, which is treated as a parameter in the reduced Hamiltonian

$$\hat{H}_{\mathrm{BO}} = \hat{\mathcal{T}}_e + \hat{V}_{ee} + \hat{V}_{eI} + U_{II}\left(\left\{\vec{R}_I\right\}\right), \tag{3.30}$$

where U_{II} is the ion-ion interaction which is now a constant.

Solving (3.30) requires finding the electronic wavefunctions $\psi_k\left(\{\vec{r}_i\}\right)$ and energies E_k which are related by the Schrödinger equation

$$\hat{H}_{\mathrm{BO}}\left|\psi_k\right\rangle = E_k\left|\psi_k\right\rangle. \tag{3.31}$$

One approach to find approximate solutions to ψ_k is the variational principle. In this approach, the energy of a trial wavefunction Ψ is calculated as

$$E\left[\Psi\right] = \frac{\left\langle \Psi \left| \hat{H}_{\mathrm{BO}} \right| \Psi \right\rangle}{\langle \Psi | \Psi \rangle} \tag{3.32}$$

and minimized by varying parameters which define Ψ. The resulting energy gives an upper bound on the ground state energy and the resulting wavefunction is an approximation to the true ground state wavefunction.

Since a wavefunction of N_e electrons is a function of $3N_e$ variables, minimizing (3.32) numerically is possible only for systems with a very small number of electrons. DFT overcomes this limitation by introducing the electron density

$$\rho\left(\vec{r}\right) = \left\langle \Psi \left| \hat{\rho}\left(\vec{r}\right) \right| \Psi \right\rangle = N_e \int \cdots \int \left|\Psi\left(\vec{r}, \vec{r}_2, \vec{r}_3, \ldots, \vec{r}_{N_e}\right)\right|^2 d\vec{r}_2 d\vec{r}_3 \ldots d\vec{r}_{N_e}, \tag{3.33}$$

where $\hat{\rho}\left(\vec{r}\right) = \sum_{i=1}^{N_e} \delta\left(\vec{r} - \hat{\vec{r}}_i\right)$ is the electron density operator. This is possible because the energy of the system is a unique functional of ρ, as stated by the Hohenberg-Kohn theorem [37] and the ground state density is found by minimizing this functional with respect to ρ. The energy functional is given by

$$E_{\mathrm{DFT}}\left[\rho\left(\vec{r}\right)\right] = \mathcal{T}_e\left[\rho\right] + E_{ee}\left[\rho\right] + E_{eI}\left[\rho\right] = F_{\mathrm{HK}}\left[\rho\right] + \int V_{eI}\left(\vec{r}\right)\rho\left(\vec{r}\right) d^3r \tag{3.34}$$

where F_{HK} contains the kinetic energy and electron-electron interaction energy and its explicit form is unknown. The classical (Hartree) part of E_{ee} can be written in terms of ρ and is given by

$$E_{\mathrm{H}}\left[\rho\right] = \frac{e^2}{2}\int\int \frac{\rho\left(\vec{r}\right)\rho\left(\vec{r}'\right)}{\left|\vec{r} - \vec{r}'\right|} d^3r d^3r', \tag{3.35}$$

however the non-classical (exchange) term does not have an explicit form and has to be approximated. To proceed, the density of the system is parameterized by a set of one-electron orbitals ϕ_k, which give the same density as the interacting system, and the non-interacting kinetic enery is calculated as

$$\mathcal{T}_0\left[\rho'\right] = \sum_k \int \phi_k^*\left(\vec{r}\right)\left(-\frac{\hbar^2\nabla^2}{2m_e}\right)\phi_k\left(\vec{r}\right)d^3r, \tag{3.36}$$

where the density is

$$\rho'\left(\vec{r}\right) = \sum_k \left|\phi_k\left(\vec{r}\right)\right|^2. \tag{3.37}$$

The difference

$$E_{\mathrm{xc}}\left[\rho'\right] = \mathcal{T}_e\left[\rho'\right] - \mathcal{T}_0\left[\rho'\right] + E_{ee}\left[\rho'\right] - E_{\mathrm{H}}\left[\rho'\right] \tag{3.38}$$

is called the exchange-correlation functional and is given by various approximations such as the local density approximation [38] or the generalized gradient approximation [39]. To obtain the one-electron wavefunctions, we use the variational principle on the density functional

$$E\left[\rho'\right] = \mathcal{T}_0\left[\rho'\right] + E_{\mathrm{H}}\left[\rho'\right] + E_{eI}\left[\rho'\right] + E_{xc}\left[\rho'\right] \tag{3.39}$$

under the orthonormality constraint $\langle\phi_k|\phi_{k'}\rangle = \delta_{kk'}$ which results in

$$\frac{\delta\left\{E\left[\rho'\right] - \sum_{k,k'}\varepsilon_{k,k'}\left[\int \phi_k^*\left(\vec{r}\right)\phi_{k'}\left(\vec{r}\right)d^3\vec{r} - \delta_{kk'}\right]\right\}}{\delta\phi_k^*} = 0, \tag{3.40}$$

where $\varepsilon_{k,k'}$ are Lagrange multiplers of the constraint. By choosing a suitable basis for ϕ_k where $\varepsilon_{k,k'}$ is diagonal, the variational equation results in the Kohn-Sham [40] equations

$$\left\{-\frac{\hbar^2\nabla^2}{2m} + \left[\int \frac{e\rho'\left(\vec{r}'\right)}{\left|\vec{r}-\vec{r}'\right|}d^3r' + V_{\mathrm{xc}}\left(\vec{r}\right) - \sum_I \frac{Z_I e^2}{\left|\vec{r}-\vec{R}_I\right|}\right]\right\}\phi_k\left(\vec{r}\right) = \varepsilon_k\phi_k\left(\vec{r}\right), \tag{3.41}$$

where the exchange-correlation potential V_{xc} is defined as $V_{\mathrm{xc}} = \frac{\delta E_{\mathrm{xc}}}{\delta\rho'}$. The total energy of the system $E_{\mathrm{tot}}\left(\rho', \left\{\vec{R}_I\right\}\right)$ can then be calculated from the single electron energies ε_k using

$$E_{\mathrm{tot}}\left(\rho', \left\{\vec{R}_I\right\}\right) = \sum_k \varepsilon_k - E_{\mathrm{H}}\left[\rho'\right] + E_{\mathrm{xc}}\left[\rho'\right] - \int V_{\mathrm{xc}}\left[\rho'\right]\rho'\left(\vec{r}\right)d^3r.$$

The forces acting on the ions are given by $\vec{F}_I = -\vec{\nabla}_{\vec{R}_I}E_{\mathrm{tot}}$, which would require solving the KS equations for different values of $\vec{R}_I$. A simpler method of calculating $\vec{F}_I$ is provided by the Hellmann-Feynman [41] theorem

$$\vec{F}_I = \left\langle\Psi'\left|-\vec{\nabla}_{\vec{R}_I}\hat{H}_{\mathrm{KS}}\right|\Psi'\right\rangle, \tag{3.42}$$

where $|\Psi'\rangle = \prod_k |\phi_k\rangle$ is the non-interacting electron gound state obtained from solving the KS equations and $\hat{H}_{\mathrm{KS}}$ is the KS Hamiltonian defined by (3.41). In this work, solution of the KS equations and calculation of ionic forces is performed using the Quantum Espresso software package [42].

3.7 Schwinger boson mean field theory

Schwinger boson mean field theory (SBMFT) [43, 44] is an approximation for treating quantum spin Hamiltonians, which combines the approach of traditional MFT with spin wave theory. The inclusion of quantum effects in SBMFT allows it to correctly describe lower dimensional systems where classical MFT fails. Compared to spin wave theory, SBMFT is usually valid for a larger temperature range relative to the transition temperature. We start from the Hamiltonian of a Heisenberg antiferromagnet on a square lattice ($J > 0$)

$$H = J \sum_{\langle ij \rangle} \vec{S}_i \cdot \vec{S}_j. \tag{3.43}$$

The Schwinger boson representation of the spins is obtained from the transformation

$$S^+ = b_\uparrow^\dagger b_\downarrow, \qquad S^z = \frac{1}{2}\left(b_\uparrow^\dagger b_\uparrow - b_\downarrow^\dagger b_\downarrow\right) \tag{3.44}$$

with the constraint

$$\sum_\sigma b_\sigma^\dagger b_\sigma = 2S, \tag{3.45}$$

where $\sigma \in \{\uparrow, \downarrow\}$, which assures a physical value for the spin. On a bipartite lattice consisting of sublattices A and B, we can rotate all spins on sublattice B around the y axis using

$$b_{\uparrow j} \to -b_{\downarrow j}, \qquad b_{\downarrow j} \to b_{\uparrow j}, \tag{3.46}$$

with $j \in B$. Then, by defining the AFM bond operator on the rotated spins

$$\mathcal{A}_{ij} = \sum_\sigma b_{i\sigma} b_{j\sigma} \tag{3.47}$$

we can write

$$H = -\frac{J}{2} \sum_{\langle ij \rangle} \mathcal{A}_{ij}^\dagger \mathcal{A}_{ij} + \frac{JzNS^2}{2} + \sum_i \nu_i \left(\sum_\sigma b_{i\sigma}^\dagger b_{i\sigma} - 2S \right), \tag{3.48}$$

where z is the number of nearest neighbors and N is the number of lattice sites. The last term in (3.48) is a Lagrange multiplier, which ensures constraint (3.45) is obeyed at each lattice site. The second term in (3.48) is a constant and we will drop it from now on. The SBMFT approximation consists of taking a uniform value for ν on all lattice sites as well as splitting the interaction term using the mean field approximation. Using

$$\mathcal{A}_{ij} = \langle \mathcal{A}_{ij} \rangle + \delta \mathcal{A}_{ij} \tag{3.49}$$

and dropping terms which are second order in $\delta\mathcal{A}_{ij}$ we obtain

$$H_{\text{SBMFT}} = -\frac{J}{2}\sum_{\langle ij\rangle}\left(-\left|\langle\mathcal{A}_{ij}\rangle\right|^2 + \langle\mathcal{A}_{ij}\rangle^\dagger\,\mathcal{A}_{ij} + \mathcal{A}_{ij}^\dagger\,\langle\mathcal{A}_{ij}\rangle\right) + \nu\sum_i\left(\sum_\sigma b_{i\sigma}^\dagger b_{i\sigma} - 2S\right). \tag{3.50}$$

We define $\mathcal{Q} \equiv -J\langle\mathcal{A}_{ij}\rangle/2$ and assume it to be real and bond independent in the mean field approximation. The Hamiltonian then reads

$$H_{\text{SBMFT}} = zN\frac{\mathcal{Q}^2}{J} - 2N\nu S + \mathcal{Q}\sum_{\langle ij\rangle\sigma}\left(b_{i\sigma}b_{j\sigma} + b_{i\sigma}^\dagger b_{j\sigma}^\dagger\right) + \nu\sum_{i\sigma} b_{i\sigma}^\dagger b_{i\sigma}. \tag{3.51}$$

After diagonalizing (3.51) using a Bogoliubov transformation, we obtain the final form of the SBMFT Hamiltonian

$$H_{\text{SBMFT}} = \sum_{\vec{k}\sigma}\omega_{\vec{k}}\left(\beta_{\vec{k}\sigma}^\dagger\beta_{\vec{k}\sigma} + \frac{1}{2}\right) + zN\frac{\mathcal{Q}^2}{J} - N\nu\left(2S+1\right), \tag{3.52}$$

where

$$\begin{aligned}
\omega_{\vec{k}} &= \sqrt{\nu^2 - \left(z\mathcal{Q}\gamma_{\vec{k}}\right)^2} \\
\gamma_{\vec{k}} &= \frac{1}{z}\sum_\delta e^{i\vec{k}\cdot\vec{\delta}} \\
\beta_{\vec{k}\sigma} &= \cosh\theta_{\vec{k}}\, b_{\vec{k}\sigma} - \sinh\theta_{\vec{k}}\, b^\dagger_{-\vec{k}\sigma} \\
\tanh\theta_{\vec{k}} &= -\frac{z\mathcal{Q}\gamma_{\vec{k}}}{\nu}.
\end{aligned} \tag{3.53}$$

To find $\mathcal{Q}$ and ν, the free energy is calculated as

$$F_{\text{SBMFT}} = \beta^{-1}\sum_{\vec{k}\sigma}\ln\left[2\sinh\left(\frac{\beta\omega_{\vec{k}}}{2}\right)\right] - N\nu\left(2S+1\right) + zN\frac{\mathcal{Q}^2}{J} \tag{3.54}$$

and minimized by requiring $\partial F/\partial\mathcal{Q} = \partial F/\partial\nu = 0$. This results in two self-consistency equations

$$\frac{1}{N}\sum_{\vec{k}}\frac{z^2\gamma_{\vec{k}}^2\mathcal{Q}}{\omega_{\vec{k}}}\left(n_{\vec{k}} + \frac{1}{2}\right) = \frac{z\mathcal{Q}}{J} \tag{3.55}$$

$$\frac{1}{N}\sum_{\vec{k}}\frac{\nu}{\omega_{\vec{k}}}\left(n_{\vec{k}} + \frac{1}{2}\right) = S + \frac{1}{2}, \tag{3.56}$$

where

$$n_{\vec{k}} = 1/\left(e^{\beta\omega_{\vec{k}}} - 1\right). \tag{3.57}$$

It is useful to define the spin-wave velocity c and energy gap Δ, such that the dispersion relation becomes

$$\omega_{\vec{k}} = c\sqrt{\left(1+\Delta\right)^2 - \gamma_{\vec{k}}^2}. \tag{3.58}$$

The effect of an external magnetic field along the z axis in (3.43) can be included by an additional term $-h\sum_i S_i^z$. The effect of an external field on the dispersion is to replace $\Delta \to \Delta + h$. The magnetization can then be computed from

$$M = -\lim_{N\to\infty}\left\langle \frac{\partial F}{\partial h}\right\rangle = S + \frac{1}{2} - 2c\int_0^1 \frac{1+\Delta+h}{\omega(\gamma)}\left(n(\omega(\gamma)) + \frac{1}{2}\right)\varrho(\gamma)\,d\gamma, \tag{3.59}$$

where

$$\varrho(\gamma) = \frac{2}{\pi^2}K\left(1-\gamma^2\right) \tag{3.60}$$

is the density of states of a square lattice, which enters from taking the continuum limit in the sum over $\vec{k}$ and K is an elliptic integral of the first kind.

4 Experimental methods

4.1 The samples

4.1.1 $(\mathbf{Fe}_{1-x}\mathbf{Mn}_x)_2\,\mathbf{AlB}_2$

Powder samples of $(Fe_{1-x}Mn_x)_2\,AlB_2$ were prepared [15] in two versions: natural B and isotopically enriched ^{11}B. All compositions were prepared via a two-step reactive powder metallurgy route in a horizontal alumina tube furnace under flowing Ar. Samples with ^{11}B (Cambridge Isotopes, 98%) were made with nominal Mn concentrations of $x = 0$, 0.05, 0.1, 0.2, 0.25, 0.5, and 1. Additionally, samples with natural B were made with nominal Mn concentrations of $x = 0.2$, 0.3, 0.5, 0.75, and 1.

4.1.2 RE-*i*-MAX

Powder samples of $\left(Mo_{2/3}RE_{1/3}\right)_2\,AlC$ with RE = Nd, Gd, Tb, Dy, Ho and Er were synthesized by pressureless sintering the following elemental powders: graphite (99.999%), Mo (99.99%) from Sigma-Aldrich, and Al (99.8%) from Alfa Aesar, and RE (99.9%) from Stanford Advanced Materials. Stoichiometric amounts of the elemental powders are manually mixed in an agate mortar, placed in an alumina crucible that is in turn inserted in an alumina tube furnace through which 5 sccm of Ar is flowing. The furnace is then heated, at 5 °C per minute, up to 1500 °C and held at 1500 °C for 10 h, before furnace cooling to RT. The loosely sintered powders are crushed into a fine powder that is directly used for further analysis.

$\left(Mo_{2/3}Gd_{1/3}\right)_2\,AlC$ single crystals were grown using a flux growth technique in an induction-heated growth reactor and a sealed graphite crucible. Sealing was mandatory for avoiding RE and Al evaporation, and implies to rely on spontaneous nucleation inside the flux in order to produce the crystals. Initial molar ratios x before carbon incorporation were $x_{Mo} = 0.1$, $x_{Gd} = 0.4$ and $x_{Al} = 0.5$. After applying a maximum temperature of 1800 °C for 1 h, required for melting the Mo element, the growth reactor was slowly cooled down to 1000 °C in 7 days. The source of C was the graphite crucible walls, and typical C concentrations in the flux ranged from $x_C = 0.2 - 0.4$, as estimated from weighting the crucible before and after growth. After growth, single crystals were extracted from the solidified flux by oxidizing the latter inside a chamber equipped with an air flux bubbling in water. Maximum lateral crystal size rarely exceeded one millimeter, and each growth resulted in hundreds of small single crystals with a wide distribution in size. Single crystals with a lateral size larger than 100 µm were selected. In addition to crystals grown in those optimal conditions, crystals produced with different growth conditions (cooling during 2 days and slightly different flux compositions) were also collected.

4.2 Powder X-ray diffraction

A typical X-ray diffraction (XRD) experiment consists of irradiating a powder sample using an X-ray beam and recording the scattered intensity as function of scattering angle 2θ. Crystallographic reflections are obtained when the scattering angle satisfies the Bragg condition [27]

$$\lambda = 2d_{hkl}\sin\theta, \tag{4.1}$$

where λ is the X-ray wavelength and

$$d_{hkl} = \frac{2\pi}{|\vec{\kappa}|},$$

is the distance between neighboring (hkl) planes with $\vec{\kappa} = h\vec{a}_1^* + k\vec{a}_2^* + l\vec{a}_3^*$ being the scattering vector. The angular dependence of the scattered intensity is given by [45]

$$I(2\theta) \propto m_{hkl}\left|\mathcal{F}_{hkl}\right|^2 P(2\theta)\, L(\theta), \tag{4.2}$$

where m_{hkl} is the multiplicty of the (hkl) reflection, $\mathcal{F}_{hkl}$ is the structure factor given by (4.3), $P(2\theta)$ is the polarization correction given by (4.4) and $L(\theta)$ is the Lorentz factor given by (4.5).

$$\mathcal{F}_{hkl}(\vec{\kappa}) = \sum_{\delta} f_\delta(\vec{\kappa})\, e^{-i\vec{\kappa}\cdot\vec{\delta}} e^{-W_\delta} \tag{4.3}$$

$$P(2\theta) = \frac{1}{2}\left(1 + \cos^2 2\theta\right) \tag{4.4}$$

$$L(\theta) = \frac{1}{\sin\theta\sin 2\theta} \tag{4.5}$$

In (4.3), δ runs over all atoms in the unit cell wth position $\vec{\delta}$ relative to the unit cell origin and f_δ is the atomic form factor given by

$$f(\vec{\kappa}) = r_0 \int n(\vec{r})\, e^{i\vec{\kappa}\cdot\vec{r}} d^3\vec{r}, \tag{4.6}$$

where $r_0 = 2.82 \times 10^{-5}$ Å is the calssical electron radius and $n(\vec{r})$ is the electronic number density. The additional W_δ term in (4.3) is the Debye-Waller factor and is expanded upon in Sec. 4.4.1. The polarization factor [45, 46] arises because the intensity of the measured X-rays depends on the angle between the polarization of the X-ray and the scattering direction. The Lorentz factor contains two contributions. The first, $1/\sin\theta$ comes from the fact that the directions of crystallites in the powder are randomly distributed in the unit sphere and represents the probability that a given crystallite will be correctly aligned as to satisfy the Bragg condition. The second term, $1/\sin 2\theta$ is the proportion of X-rays scattered into the Debeye-Scherrer cone [45] that are counted by the detector.

4.3 Magnetization measurements

A magnetization measurement [47] consists of moving a sample through a pickup coil. A moving magnetic moment produces a time-dependent magnetic field, which in turn induces an electric current in the pickup coil. An example of such a setup is depicted in Figure 4.1. In this example the detection coils contain four pickup loops with the two outer loops wound opposite to the two inner coils. Such a configuration is called a second order gradiometer and it measures the second time derivative of the magnetic field. The small current from the pickup coil is detected by a superconducting quantum interference device (SQUID), which is a current to voltage converter. In a DC magnetization measurement,

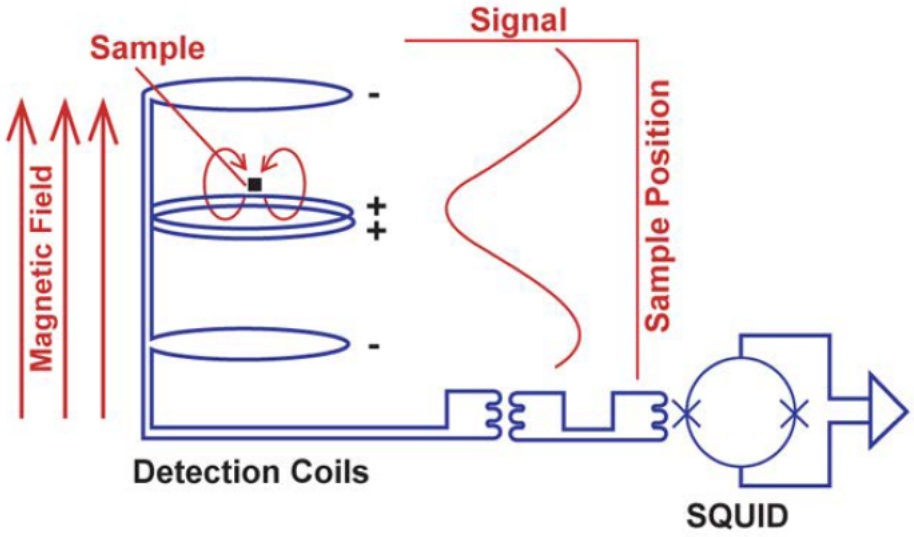

Figure 4.1: An example of a pickup coil in the Quantum Design MPMS3 magnetic measurement system.

the sample is moved at a constant velocity v through the pickup coils. Assuming the sample is small enough, its vector potential can be described in the dipole approximation as

$$\vec{A} = \frac{\vec{M} \times \vec{r}}{r^3}, \tag{4.7}$$

where $\vec{M}$ is the magnetic moment of the sample. The magnetic flux passing through the pickup coil can be calculated using Ampere's law

$$\phi = \int \vec{B} \cdot d\vec{a} = \int \vec{A} \cdot d\vec{l}. \tag{4.8}$$

For a magnetic moment aligned parallel to the axis of the coil and moving along it, this gives

$$\phi(t) = 2\pi \frac{MR^2}{\left[(vt)^2 + R^2\right]^{3/2}}, \tag{4.9}$$

where R is the radius of the coil, v is the velocity of the sample and t is time. By fitting the measured signal from the pickup coil to $\phi''(t)$ the magnetic moment M can be extracted.

4.4 Neutron scattering

Since the neutron does not possess an electric charge, it does not interact with the electrons in matter and therefore has a large penetration depth. However, the spin of the neutron turns it into a sensitive probe for magnetism, by interacting with the magnetic moments produced by electrons in matter. The mass of the neutron $m_n = 1.675 \times 10^{-27}$ kg results in a de-Broglie wavelength of several angstroms, which is comparable with interatomic distances in solids. Moreover, the spin of the neutron gives it a magnetic moment of $\mu_n = -1.913\,\mu_N$ which gives magnetic scattering comparable in intensity to nuclear scattering. The energy of thermal neutrons (≈ 25 meV) is comparable to excitation energies of dynamical processes in solids and allow the study of phonons and magnons [48].

In a general scattering experiment, a neutron beam with momentum $\vec{p_i}$ and flux Φ is incident upon a sample. A detector measures the intensity of neutrons scattered into a solid angle $d\Omega$. The quantity of interest is the differential scattering cross section

$$\frac{d\sigma}{d\Omega} = \frac{\text{number of neutrons scattered into } d\Omega}{\Phi d\Omega}. \tag{4.10}$$

The scattering cross section depends on properties of the system under study and thus its measurement allows to determine crystallographic and magnetic properties of the system.

4.4.1 Nuclear neutron scattering

The scattering of the neutron by the nucleus [49, 50] occurs through the strong interaction. Although an exact formula for the potential due to the strong interaction is not known, we know that it has a very short range (on the order of a few fm). It was therefore proposed to approximate the neutron-nucleus interaction with the Fermi pseudopotential

$$V^{(1)}(\vec{r}) = \frac{2\pi\hbar^2}{m_n} b \delta^{(3)}(\vec{r}). \tag{4.11}$$

To calculate the partial differential cross section of a scattering process, where the neutron is scattered from momentum $\hbar\vec{k_i}$ to $\hbar\vec{k_f}$, energy E_i to E_f and the

scattering system changes from state[2] ξ_i to ξ_f, we use Fermi's golden rule

$$\left(\frac{d^2\sigma}{d\Omega dE_f}\right)_{\xi_i,\xi_f} = \frac{k_f}{k_i}\left(\frac{m_n}{2\pi\hbar^2}\right)^2 \left|\left\langle \vec{k}_f, \xi_f \left| V \right| \vec{k}_i, \xi_i \right\rangle\right|^2 \delta\left(\hbar\omega + E_{\xi_i} - E_{\xi_f}\right), \quad (4.12)$$

where $\hbar\omega \equiv E_i - E_f$ is the energy transfer of the neutron and E_ξ is the energy of the system in state ξ. For a scattering system comprised of many nuclei, the potential is given by

$$V(\vec{r}) = \sum_i V_i^{(1)}\left(\vec{r} - \vec{R}_i\right), \quad (4.13)$$

where $V_i^{(1)}$ is the Fermi pseudo potential of the i'th nucleus with scattering length b_i and position $\vec{R}_i$. To calculate the nuclear scattering cross section of a crystal, we start by evaluating the matrix element in (4.12) with (4.13) which gives

$$\left\langle \vec{k}_f, \xi_f \left| V \right| \vec{k}_i, \xi_i \right\rangle = \frac{2\pi\hbar^2}{m_n}\left\langle \xi_f \left| \sum_i b_i e^{i\vec{\kappa}\cdot\hat{\vec{R}}_i} \right| \xi_i \right\rangle, \quad (4.14)$$

where $\hbar\vec{\kappa} \equiv \hbar\vec{k}_i - \hbar\vec{k}_f$ is the neutron momentum transfer and $\hat{\vec{R}}_i$ is the nuclear position operator. Summing over final states ξ_f and thermally averaging over initial states ξ_i, the coherent partial differential cross section can be expressed as [49, 50]

$$\left(\frac{d^2\sigma}{d\Omega dE_f}\right)_{\text{coh}} = \frac{k_f}{k_i} N \mathbb{S}_{\text{nuc}}^{\text{coh}}(\vec{\kappa}, \omega), \quad (4.15)$$

where the coherent nuclear scattering function is defined as

$$\mathbb{S}_{\text{nuc}}^{\text{coh}}(\vec{\kappa}, \omega) = \frac{1}{2\pi\hbar}\int \frac{1}{N}\sum_{j,j'} b_j b_{j'} \left\langle e^{-i\vec{\kappa}\cdot\hat{\vec{R}}_j(0)} e^{i\vec{\kappa}\cdot\hat{\vec{R}}_{j'}(t)} \right\rangle e^{-i\omega t} dt. \quad (4.16)$$

Here $\hat{\vec{R}}(t)$ is the nuclear position operator in the Heisenberg representation defined by

$$\hat{\vec{R}}(t) = e^{i\frac{H}{\hbar}t}\hat{\vec{R}}e^{-i\frac{H}{\hbar}t}, \quad (4.17)$$

where H is the Hamiltonian of the scattering system. In a crystal, the atomic positions can be written in the general form

$$\hat{\vec{R}}_{j,\delta}(t) = \vec{l}_j + \vec{\delta} + \hat{\vec{u}}_j^{\delta}(t), \quad (4.18)$$

where $\vec{l}_j$ is the origin of the j'th unit cell, $\vec{\delta}$ is the atomic position in the unit cell and $\hat{\vec{u}}_j^{\delta}$ is the atomic displacement from equilibrium due to thermal motion.

[2] For this calculation, the harmonic crystal approximation is used and therefore the states of the scattering system are defined by a collection of quantum numbers $n_{\vec{q},s}$ which denote the number of phonons with momentum $\vec{q}$ and polarization s.

In the harmonic crystal approximation [28], the displacement operator can be expanded in terms of phonon modes as

$$\hat{\vec{u}}_j^{\delta}(t) = \left(\frac{\hbar}{2M_\delta N}\right)^{\frac{1}{2}} \sum_{\vec{q},s} \frac{1}{\sqrt{\omega_{\vec{q},s}}} \left[\vec{e}_{\vec{q},s}^{\,\delta} a_{\vec{q},s} e^{i\left(\vec{q}\cdot\vec{l}_j - \omega_{\vec{q},s}t\right)} + \vec{e}_{\vec{q},s}^{\,*\delta} a_{\vec{q},s}^{\dagger} e^{-i\left(\vec{q}\cdot\vec{l}_j - \omega_{\vec{q},s}t\right)}\right], \tag{4.19}$$

where M_δ is the mass of the nucleus, $\vec{q}$ is the wavevector of the phonon mode, $\vec{e}$ is the phonon polarization vector, $s = 1, \ldots, 3\nu$ with ν being the number of atoms in the unit cell is the polarization index, and a and $a^\dagger$ are ladder operators for annihiliation and creation of phonons, respectively. Using (4.18) and (4.19) in (4.16) and retaining only the elastic term in the expansion of the thermal average [50], gives

$$\begin{aligned}
\mathbb{S}_{\text{nuc}}^{\text{coh}}(\vec{\kappa},\omega) &= \frac{1}{2\pi\hbar}\frac{1}{N}\sum_{j,j'} e^{-i\vec{\kappa}\cdot\left(\vec{l}_j - \vec{l}_j'\right)} \left|\sum_\delta b_\delta e^{-i\vec{\kappa}\cdot\vec{\delta}} e^{-W_\delta}\right|^2 \int e^{-i\omega t} dt \\
&= \frac{(2\pi)^3}{v_0} \left|\mathcal{F}(\vec{\kappa})\right|^2 \sum_{\vec{q}} \delta^{(3)}(\vec{\kappa} - \vec{q})\, \delta(\hbar\omega),
\end{aligned} \tag{4.20}$$

where v_0 is the unit cell volume, $\vec{q}$ runs over all reciprocal lattice vectors and $\mathcal{F}$ is the nuclear structure factor. The $\delta^{(3)}(\vec{\kappa} - \vec{q})$ term is obtained from the lattice summation and gives the Laue condition for diffraction from a crystal [27]. The nuclear structure factor $\mathcal{F}$ is defined analogously to (4.3) as

$$\mathcal{F}(\vec{\kappa}) = \sum_\delta b_\delta e^{-i\vec{\kappa}\cdot\vec{\delta}} e^{-W_\delta}, \tag{4.21}$$

where W_δ is the Debeye-Waller factor of nucleus δ and is given by

$$e^{-\frac{1}{3}\kappa^2\left\langle u_\delta^2\right\rangle} \equiv e^{-2W_\delta}, \tag{4.22}$$

where $\left\langle u_\delta^2\right\rangle$ denotes the mean squared displacement of atom δ. This term decreases the observed intensity of Bragg peaks in the diffraction profile due to the momentary deviation of a given nucleus from its ideal equilibrium position. The appeareance of κ^2 in the exponential means that this correction affects the scattering intensity of reflections which occur at higher κ values (or high scattering angles).

4.4.2 Magnetic neutron scattering

The magnetic interaction between the neutron spin and an unpaired electron in the crystal is given by [50, 51]

$$V_m = -\vec{\mu}_N \cdot \vec{B} = -\frac{\mu_0}{4\pi} g_n \mu_N g_e \mu_B \vec{\sigma} \cdot \left(\vec{\nabla} \times \left(\frac{\vec{s} \times \hat{R}}{R^2}\right) + \frac{1}{\hbar}\frac{\vec{p} \times \hat{R}}{R^2}\right), \tag{4.23}$$

where $g_n \approx 1.913$ is the neutron g-factor, $g_e \approx 2$ is the electron g-factor, $\vec{\sigma}$ and $\vec{s}$ are the neutron and electron spin operators, respectively, R is the distance between the neutron and electron, $\hat{R}$ is a unit vector along R and $\vec{p}$ is the momentum of the electron. The magnetic scattering cross section is calculated by following the same steps as in the nuclear case. First, we calculate the matrix element in (4.12) which gives

$$\left\langle \vec{k}_f \left| \frac{m_n}{2\pi\hbar^2} V_m \right| \vec{k}_i \right\rangle = -g_n r_0 \vec{\sigma} \cdot \vec{Q}_\perp, \tag{4.24}$$

where

$$\vec{Q}_\perp = \sum_j e^{i\vec{\kappa}\cdot\vec{r}_j} \left(\vec{\kappa} \times \vec{s}_j \times \vec{\kappa} + \frac{i}{\hbar\kappa} \vec{p}_j \times \vec{\kappa} \right) \equiv \vec{\kappa} \times \vec{Q} \times \vec{\kappa} \tag{4.25}$$

and r_0 is the classical electron radius given in Sec. (4.2). It can be shown [50] that $\vec{Q} = -\vec{M}(\vec{\kappa})/g_e\mu_\mathrm{B}$, where $\vec{M}(\vec{\kappa})$ is the Fourier transform of the magnetization density operator. $\vec{Q}_\perp$ is the component of $\vec{Q}$ perpendicular to the scattering vector, and therefore (4.24) signifies that only the perpendicular component of the magnetization produces scattering.

The partial differential scattering cross section can then be expressed in an analagous fashion to (4.15) by defining the magnetic scattering function

$$\begin{aligned} \mathbb{S}^{\mathrm{coh}}_{\mathrm{mag}}(\vec{\kappa},\omega) = (g_n r_0)^2 \sum_{\alpha\beta} (\delta_{\alpha\beta} - \hat{\kappa}_\alpha \hat{\kappa}_\beta) \frac{1}{2\pi\hbar} \int_{-\infty}^{\infty} \frac{1}{N} \sum_{j,j'} \left(\frac{1}{2} g_j \tilde{f}^*_j(\vec{\kappa}) \right) \left(\frac{1}{2} g_{j'} \tilde{f}_{j'}(\vec{\kappa}) \right) \\ \times \left\langle e^{-i\vec{\kappa}\cdot\hat{\vec{R}}_j(0)} e^{i\vec{\kappa}\cdot\hat{\vec{R}}_{j'}(t)} \right\rangle \left\langle S^\alpha_j(0) S^\beta_{j'}(t) \right\rangle e^{-i\omega t} dt \end{aligned} \tag{4.26}$$

where $\tilde{f}_j$ is the magnetic form factor of atom j which is defined in analogy with (4.6) as

$$\tilde{f}(\vec{\kappa}) = \int \tilde{n}(\vec{r}) e^{i\vec{\kappa}\cdot\vec{r}} d^3\vec{r}, \tag{4.27}$$

where $\tilde{n}(\vec{r})$ is the normalized density of unpaired electrons in the atom. From normalization, $\tilde{f}(\vec{\kappa}) = 1$. In the dipole approximation [50, 51], $\tilde{f}(\vec{\kappa})$ can be written as

$$\tilde{f}(\vec{\kappa}) = \mathrm{j}_0(\kappa) + \frac{g - g_S}{g} \mathrm{j}_2(\kappa), \tag{4.28}$$

where j_0 and j_2 are spherical Bessel functions of the first kind. $\vec{S}_j$ refers to the total angular momentum (spin and orbital) operator of atom j and

$$g = 1 + \frac{g_S}{2} \tag{4.29}$$

is the Landé g-factor with

$$g_S = \frac{\mathbb{J}(\mathbb{J}+1) - \mathbb{L}(\mathbb{L}+1) + S(S+1)}{\mathbb{J}(\mathbb{J}+1)}, \tag{4.30}$$

where $\mathbb{J}$, $\mathbb{L}$ and S are the total, orbital and spin angular momentum quantum numbers, respectively.

Comparison of (4.26) with (4.16) shows two main differences. First, the nuclear scattering length b is replaced by $\frac{g_n r_0}{2}\tilde{f}(\vec{\kappa})$. Unlike nuclear scattering, this term depends on the scattering direction which is a consequence of the long-range nature of the magnetic interaction (4.23). Second, the scattering also depends on the spin-spin correlation function $\left\langle S_j^{\alpha}(0) S_{j'}^{\beta}(t)\right\rangle$. As an example, the differential cross section for elastic scattering from a paramagnet is

$$\frac{d\sigma}{d\Omega} = \frac{2}{3}\left(g_n r_0\right)^2 N \sum_{\delta}\left|\frac{1}{2} g_\delta \tilde{f}_\delta(\vec{\kappa})\right|^2 e^{-2W_\delta} S_\delta\left(S_\delta+1\right), \tag{4.31}$$

where δ runs over all atoms in the unit cell and W_δ is the Debeye-Waller factor defined in (4.22). Equation (4.31) shows that magnetic scattering in the paramagnetic phase does not produce Bragg peaks and only contributes to the background counts. Unlike nuclear scattering, however, this background count depends on the scattering angle and is reduced once the material forms long-range magnetic order.

For a general magnetic structure which can be broken down into Fourier components (3.7), the magnetic scattering function is given by

$$\mathbb{S}_{\mathrm{mag}}^{\mathrm{coh}}(\vec{\kappa},\omega) = \frac{(2\pi)^3}{v_0}\sum_{\vec{q}_m}\left|\vec{\mathcal{F}}_{m\perp,\vec{q}_m}(\vec{\kappa})\right|^2 \sum_{\vec{q}_c}\delta^{(3)}\left(\vec{\kappa}-\vec{q}_c-\vec{q}_m\right)\delta(\hbar\omega), \tag{4.32}$$

where $\vec{q}_c$ is a reciprocal lattice vector and $\vec{q}_m$ are propagation vectors that describe the magnetic structure. The form of (4.32) is similar to its nuclear counterpart (4.20) apart from two differences. First, the lattice sum results in the term $\delta^{(3)}\left(\vec{\kappa}-\vec{q}_c-\vec{q}_m\right)$ instead of $\delta^{(3)}\left(\vec{\kappa}-\vec{q}_c\right)$ as in the nuclear case. This means that neutrons will scatter with momentum transfer given by $\vec{\kappa}=\vec{q}_c+\vec{q}_m$ and may therefore appear as satellite reflections of the base crystallographic reflections or, for $\vec{q}_m=0$, add to the intensity of the nuclear reflections. Second, the intensity of the magnetic reflections is proportional to the perpendicular component of the magnetic structure factor $\left|\vec{\mathcal{F}}_{m\perp,\vec{q}_m}\right|^2$ which is defined as

$$\vec{\mathcal{F}}_{m\perp,\vec{q}_m}(\vec{\kappa}) = \vec{\mathcal{F}}_{m,\vec{q}_m}(\vec{\kappa}) - \left(\vec{\mathcal{F}}_{m,\vec{q}_m}(\vec{\kappa})\cdot\hat{\kappa}\right)\hat{\kappa}, \tag{4.33}$$

with the magnetic structure factor given by

$$\vec{\mathcal{F}}_{m,\vec{q}_m}(\vec{\kappa}) = \frac{g_n r_0}{2}\sum_{\delta}\tilde{f}_\delta(\vec{\kappa})\,\vec{\mu}_{\vec{q}_m,\delta} e^{-i\vec{\kappa}\cdot\vec{\delta}} e^{-W_\delta}, \tag{4.34}$$

where $\hat{\kappa}$ is a unit vector along $\vec{\kappa}$, δ runs over all atoms in the unit cell and $\vec{\mu}_{\vec{q}_m,\delta}$ is the Fourier component of the magnetic moment on atom δ given in units of μ_{B}. Therefore, measuring the positions and intensities of magnetic Bragg peaks gives us direct information on the periodicity of the magnetic structure and the magnetic moments.

4.5 Muon spin rotation

Muon spin rotation [52] is a technique that allows to measure the magnetic field distribution inside a sample. Positive muons (μ^+) and neutrinos are produced via a weak decay from a pion $\pi^+ \rightarrow \mu^+ + \nu_\mu$. Since only left-handed neutrinos exist, a consequence of conservation of angular momentum is that the created muons are 100% polarized. When implanted into a sample, the muon spin component perpendicular to the internal magnetic field $\vec{B}$ is rotated with precession frequency

$$\omega = \gamma_\mu B, \tag{4.35}$$

where $\gamma_\mu \approx 850\,\mathrm{MHz/T}$ is the muon gyromagnetic ratio. Assuming the initial muon polarization is directed along z, the component of the polarization of the muon ensemble along z in a uniform magnetic field is given by

$$P_z(t) = \cos^2\theta + \sin^2\theta \cos(\gamma_\mu B t), \tag{4.36}$$

where $\cos\theta = \hat{z} \cdot \hat{B}$. For a general field distribution $f\left(\vec{B}\right)$, the polarization component is obtained by integrating Eq. (4.36) which gives

$$P_z(t) = \int f\left(\vec{B}\right) \left[\cos^2\theta + \sin^2\theta \cos(\gamma_\mu B t)\right] d^3\vec{B}. \tag{4.37}$$

To measure $P(t)$ along a given direction, the number of decay positrons $D(t)$ from muons stopped in the sample is recorded in two detectors D_1 and D_2, which are placed opposite to each other with the sample in between. The normals of both detectors are oriented along the desired measurement axis. The number of counts in each detector can be written as

$$D_i(t) = N_0 e^{-\frac{t \ln 2}{\tau_\mu}} P(t) + N_i^{\mathrm{BG}}, \tag{4.38}$$

where N_0 is the number of muons stopped in the sample, τ_μ is the half-life of the muon and N^{BG} is the background signal of the detector. $P(t)$ is then obtained from the detector asymmetry, which is defined by

$$A(t) \equiv \frac{\left[D_1(t) - N_1^{\mathrm{BG}}\right] - \alpha\left[D_2(t) - N_2^{\mathrm{BG}}\right]}{\left[D_1(t) - N_1^{\mathrm{BG}}\right] + \alpha\left[D_2(t) - N_2^{\mathrm{BG}}\right]}, \tag{4.39}$$

where α is a correction factor which compensates for the difference between detector efficiencies and solid angles and is determined experimentally.

4.5.1 Powders

For a powder sample, the direction of $\vec{B}$ is uniformly distributed in the unit sphere, and therefore integration gives

$$P_z(t) = \frac{1}{3} + \frac{2}{3} \int \rho(B) \cos(\gamma_\mu B t)\, B^2 dB, \tag{4.40}$$

where $\rho(B)$ is the distribution of field magnitudes. Equation (4.40) shows that $\rho(B)$ can be obtained by Fourier transforming the observed time dependent polarization signal. Two polarization functions for the cases encountered in this work are detailed below:

Collinear ferromagnet/antiferromaget: In this case, the muons experience a single magnetic field magnitude and the magnetic field distribution is given by

$$\rho(B) = \frac{1}{B^2}\delta(B - B_0). \tag{4.41}$$

The corresponding polarization function is therefore

$$P_z^{\mathrm{AFM}}(t) = \frac{1}{3} + \frac{2}{3}\cos(\gamma_\mu B_0 t). \tag{4.42}$$

Spin density wave: In this case, the magnetic field between different unit cells shows the same periodicity as the underlying magnetic structure (Figure 4.2). For a transverse SDW in one dimension, we have

$$B(x) = B_0 \cos(kx). \tag{4.43}$$

The magnetic field distribution of $|B|$ is found by using the rule for transformation of random variables

$$\rho(B)\, dB = 4f(x)\, dx. \tag{4.44}$$

Here x is uniformly distributed along $\left[0, \frac{2\pi}{k}\right]$ with $f(x) = \frac{k}{2\pi}$. The factor of 4 accounts for the fact that (4.44) is only valid when $B(x)$ is a monotonic function of x which occurs in one quarter of the interval $\left[0, \frac{2\pi}{k}\right]$ (Figure 4.2, shaded areas). The field distribution in case of an SDW is therefore given by

$$\rho(B) = 4f(x)\left.\frac{dx}{dB}\right|_{x(B)} = \frac{2}{\pi\sqrt{B_0^2 - B^2}} \tag{4.45}$$

with the corresponding polarization function

$$P_z^{\mathrm{SDW}}(t) = J_0(\gamma_\mu B_0 t), \tag{4.46}$$

where J_0 is a zero'th order Bessel function of the first kind.

In real samples, the magnetic field distribution is not as ideal as in equations (4.41) and (4.45). Local defects, impurities and lattice vibrations cause the muon polarization to lose coherence over time and P_z decays over time. Empirically, in this work, two decay rates are observed and are modeled by simple exponents $e^{-\lambda_F t}$ and $e^{-\lambda_S t}$, where F and S stand for fast and slow decay rates, respectively. The total μSR signal studied in this work is therefore of the form

$$P_z(t) = P_F e^{-\lambda_F t}\mathbb{F}(\gamma_\mu B_0 t) + P_S e^{-\lambda_S t}, \tag{4.47}$$

where $\mathbb{F}(x)$ depends on the type of oscillation observed and can be either $\cos(x)$, $J_0(x)$ or 1 if no oscillations are observed, and $P_F + P_S = 1$.

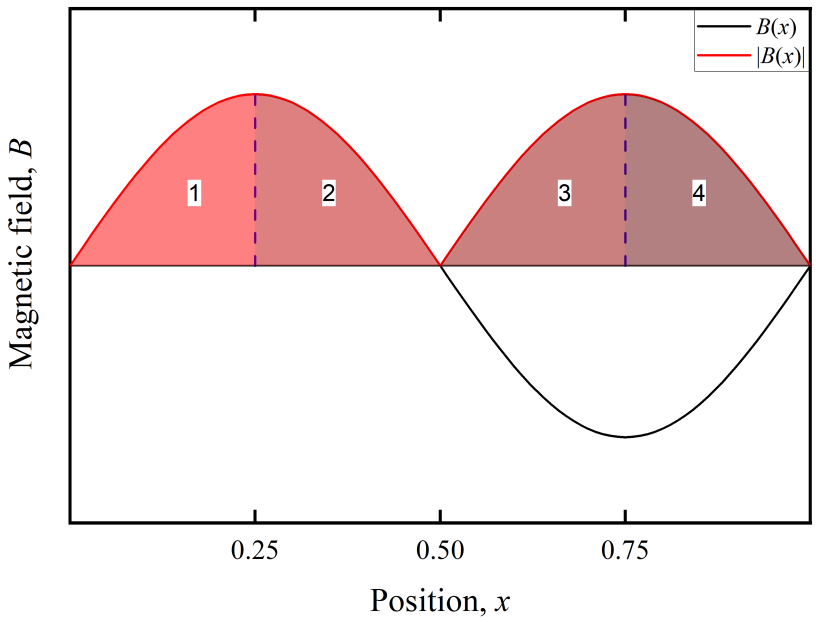

Figure 4.2: Graphical illustration of the magnetic field and its absolute value in the SDW case.

4.5.2 Single crystals

In a single crystal, the magnetic field is pointing along a constant direction

$$\vec{B} = B\sin\eta\cos\chi\hat{x} + B\sin\eta\sin\chi\hat{y} + B\cos\eta\hat{z}. \tag{4.48}$$

In the measurements performed in this work, the sample was measured using two perpendicular sets of detectors (Figure 4.3). The initial muon asymmetry is given by

$$\vec{A}_0 = A^0_{\mathrm{UD}}\sin\zeta\hat{x} + A^0_{\mathrm{FB}}\cos\zeta\hat{z}. \tag{4.49}$$

Here, A^0_{UD} and A^0_{FB} denote the maximal asymmetry along each pair of detectors.

In the following, it is assumed that the sample is made up of a large number crystal flakes which lie in the x-y plane. The flakes are not oriented and therefore χ is uniformly distrubuted along the unit circle. Time evolution of the asymmetry, given an arbitrary magnetic field is given by

$$\vec{A}(t;\zeta,\eta,\chi) = \vec{A}_{\parallel}e^{-\lambda_S t} + \vec{A}_{\perp,1}e^{-\lambda_F t}\cos(\gamma_\mu B t) + \vec{A}_{\perp,2}e^{-\lambda_F t}\sin(\gamma_\mu B t), \tag{4.50}$$

where $\vec{A}_{\parallel} = \left(\vec{A}_0\cdot\hat{B}\right)\hat{B}$ is the component of the asymmetry, parallel to the magnetic field; $\vec{A}_{\perp,1} = \vec{A}_0 - \vec{A}_{\parallel}$, and $\vec{A}_{\perp,2} = \hat{B}\times\vec{A}_{\perp,1}$ are the two perpendicular components. In this work, single crystal flakes of $\left(\mathrm{Mo}_{2/3}\mathrm{Gd}_{1/3}\right)_2\mathrm{AlC}$ with normals along the a_3^* direction were placed on the sample holder. The crystal

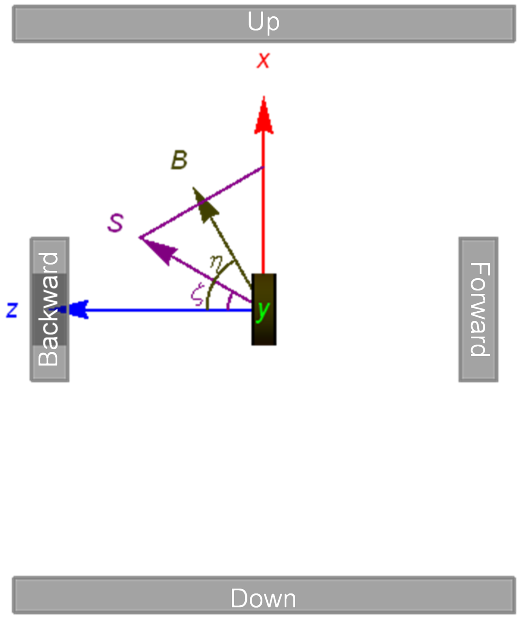

Figure 4.3: Schematic representation of the detector geometry. The different pairs of detectors are shown as grey rectangles, the sample as a dark yellow disk. Arrows indicate the x and z axes with the y axis pointing into the page. The magnetic field of the sample is shown as a dark yellow arrow and the direction of the muon spin as a purple arrow. The purple line shows the precession motion of the spin about the magnetic field.

a_3^* direction is therefore parallel to the z axis, however the flakes are randomly oriented in the x-y plane. Therefore, the total evolution of the asymmetry is obtained by averaging over χ

$$\vec{A}_{\text{avg}}(t;\zeta,\eta) = \frac{1}{2\pi}\int_0^{2\pi} \vec{A}(t;\zeta,\eta,\chi)\, d\chi. \tag{4.51}$$

The asymmetry along each pair of detectors is obtained by projecting $\vec{A}_{\text{avg}}$ along the corresponding axes. By plugging (4.48), (4.49) and (4.50) into (4.51), we obtain

$$A_{\text{UD}}(t) = \vec{A}_{\text{avg}} \cdot \hat{x} = \frac{1}{4} A_{\text{UD}}^0 \sin\zeta \left[e^{-\lambda_F t}\cos(\gamma_\mu B t)(3+\cos 2\eta) + 2e^{-\lambda_S t}\sin^2\eta\right] \tag{4.52}$$

$$A_{\text{FB}}(t) = \vec{A}_{\text{avg}} \cdot \hat{z} = A_{\text{FB}}^0 \cos\zeta \left[e^{-\lambda_F t}\cos(\gamma_\mu B t)\sin^2\eta + e^{-\lambda_S t}\cos^2\eta\right]. \tag{4.53}$$

If there is more than one muon site in the unit cell, the muons might feel different magnetic fields $\vec{B}_j$ where $j = 1 \ldots \nu$ labels the ν muon sites. The

observed asymmetry is then obtained by averaging over all muon sites with the final result

$$\overline{A}_{\mathrm{UD}}(t) = \frac{1}{4} A^0_{\mathrm{UD}} \sin\zeta \frac{1}{\nu} \sum_{j=1}^{\nu} \left[e^{-\lambda_F t} \cos(\gamma_\mu B_j t)(3 + \cos 2\eta_j) + 2e^{-\lambda_S t} \sin^2 \eta_j \right] + A^{\mathrm{BG}}_{\mathrm{UD}}(\zeta) \tag{4.54}$$

$$\overline{A}_{\mathrm{FB}}(t) = A^0_{\mathrm{FB}} \cos\zeta \frac{1}{\nu} \sum_{j=1}^{\nu} \left[e^{-\lambda_F t} \cos(\gamma_\mu B_j t) \sin^2 \eta_j + e^{-\lambda_S t} \cos^2 \eta_j \right] + A^{\mathrm{BG}}_{\mathrm{FB}}(\zeta). \tag{4.55}$$

The additional A^{BG} terms represent a background signal which comes from muons which missed the sample. Temperature dependentce of the muon asymmetry for both detector pairs is fitted empirically using

$$A(T,t) = A^D_F(T) \cos\left[\gamma_\mu B(T)\, t + \phi^D\right] e^{-\lambda_F(T)t} + A^D_S(T)\, e^{-\lambda_S(T)t} + A^D_{\mathrm{BG}} e^{-\lambda_{\mathrm{BG}}(T)t}, \tag{4.56}$$

where D denotes the pair of detectors UD or FB and T is the temperature.

5 Results and analysis of $(Fe_{1-x}Mn_x)_2AlB_2$ measurements

5.1 X-ray and neutron diffraction

Both XRD and NPD measurements are analyzed using Rietveld refinement [53] as implemented in the `FULLPROF` suite [54]. The observed number of counts N is modeled using

$$N(2\theta) = \sum_{hkl} I(2\theta_{hkl})\,\Omega(2\theta - 2\theta_{hkl}) + B(2\theta), \tag{5.1}$$

where $2\theta_{hkl}$ is the position of a reflection, $I(2\theta)$ is given by (4.2)[3] with the structure factors given by equations (4.3), (4.21) and (4.33) for X-ray, neutron and magnetic scattering, resepctively, Ω models the peak shape of the diffractometer and B represents the background. The structural model of the sample, resolution parameters of the diffractometer and background are obtained by minimizing the least squares distance between observed and calculated number of counts

$$\chi^2 = \sum_i w_i \left[N_{\text{obs}}(2\theta_i) - N_{\text{calc}}(2\theta_i)\right]^2 \tag{5.2}$$

with weights $w_i = 1/\sigma_i^2$, where σ_i are the measurement errors.

XRD measurements of different $(Fe_{1-x}Mn_x)_2AlB_2$ samples (Figure 5.1) show that the MAB phase is the dominant phase, with small amounts ($\approx 5\%$) of non-magnetic impurities. The identified impurities are α-Al_2O_3 (space group R-3c) and $(Fe_{1-y}Mn_y)_4Al_{13}$ (space group $C2/m$). The only exception is the $(Fe_{0.5}Mn_{0.5})_2Al^{11}B_2$ sample. The ^{11}B, which was used to make this sample contained SiO_2 contamination which resulted in a large amount of impurities. Refinement of the RT NPD measurements of the ^{11}B samples shows that the refined x (Table 5.1) agrees with the nominal x to within a relative error of 5%. This indicates that the $(Fe_{1-x}Mn_x)_2AlB_2$ system is thermodynamically stable in the entire x range.

At RT, the LPs of $(Fe_{1-x}Mn_x)_2AlB_2$ show a nonlinear and nonmonotonic dependence on x (Figure 5.2), which deviates from Vegard's law [55]. The unit cell volume (Table 5.1) expands from $\approx 92.5\,\text{Å}^3$ for Fe2AlB2 up to $\approx 93.5\,\text{Å}^3$ for Mn_2AlB_2. The a and c LPs expand before contracting, while the b LP contracts before expanding. The transition point in all cases is for x in the range 0.2–0.5. The deviation of the LPs from Vegard's law for large x correlates with magnetic transitions which are observed in the $(Fe_{1-x}Mn_x)_2AlB_2$ system and is therefore attributed to magnetostriction [27, 28].

Low temperature NPD measurements of $(Fe_{1-x}Mn_x)_2AlB_2$ (cf. Figure 5.3 for $x = 0.2$) show a number of main changes from the RT diffraction. For samples with $x \leq 0.2$, an increase in the intensity of the (001) reflection is observed when cooling below 310 K, 260 K and 220 K for $x = 0$, 0.1 and 0.2,

[3] For neutrons, the polarization factor is equal to unity.

Table 5.1: Refined unit cell volume (V), nominal and refined Mn occupancy (x), and weight percent (Wt%) of $(Fe_{1-x}Mn_x)_2AlB_2$ phase at room temperature obtained by XRD and NPD. Numbers in brackets indicate statistical 1σ uncertainties of the Rietveld refinement.

Method	Nominal x	Refined x	V (Å^3)	Wt%
XRD	0^a	N/A	92.568(5)	99(1)
	0.05^a		92.589(6)	98(3)
	0.1^a		92.905(5)	97(2)
	0.2^a		93.150(6)	98(2)
	0.25^a		93.195(2)	97.4(7)
	0.5^b		93.481(5)	96(2)
	0.75^b		93.657(8)	81(2)
	1^a		93.536(4)	97(2)
NPD	0^a	0	92.552(1)	99(1)
	0.1^a	0.096(4)	92.908(2)	99(1)
	0.2^a	0.190(2)	93.132(2)	99(1)
	0.25^a	0.228(4)	93.19(2)	98(1)
	0.5^a	0.461(3)	94.00(1)	59(1)
	1^a	1	93.22(4)	100

[a] ^{11}B sample

[b] Natural B sample

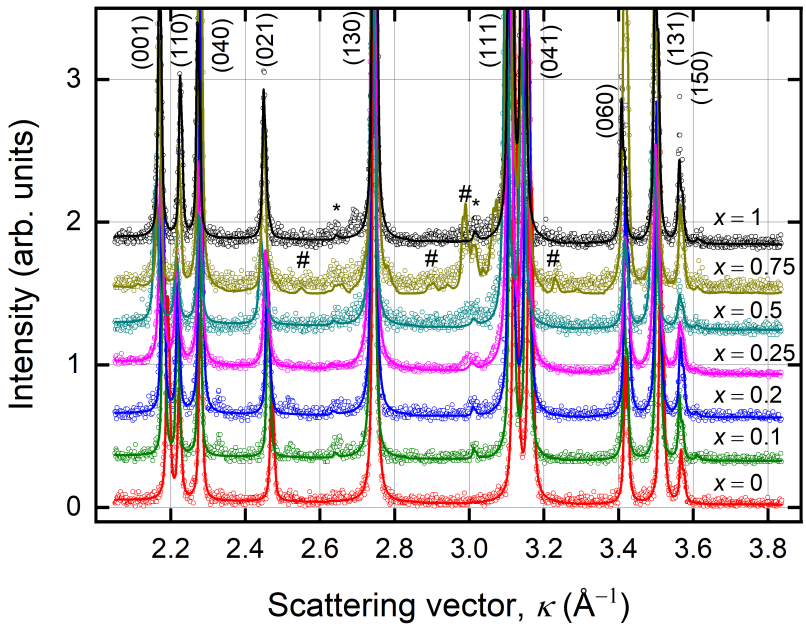

Figure 5.1: Observed XRD patterns (symbols) and the corresponding Rietveld refinement (solid lines) for different $(Fe_{1-x}Mn_x)_2AlB_2$ powders with various x values. Reflections are labeled by their Miller indices; impurity reflections are marked by * for α-Al_2O_3 and # for $(Fe_{1-y}Mn_y)_4Al_{13}$. The patterns for $x = 0.5$ and 0.75 were measured on a natural B sample.

respectively. This increase is consistent with an FM ordering of the MAB phase with the magnetic moments aligned along the a axis as observed previously [11]. For samples with $x \geq 0.2$, an additional reflection appears at $\kappa \approx 1.08\,\text{Å}^{-1}$ upon cooling. This reflection was identified to correspond to a magnetic unit cell, which is doubled along the c axis relative to the chemical unit cell of the MAB phase. This corresponds to an AFM magnetic structure with a propagation vector of $\vec{k} = (0, 0, 1/2)$. In addition, a slight decrease is observed in the neutron background at low κ values (compare the difference in background for $\kappa < 1.2$ with $\kappa > 2.1$ at different temperatures in Figure 5.3) indicating a decrease in the paramagnetic scattering [4] due to the onset of long-range magnetic ordering [50, 51].

Symmetry analysis of the irreducible representations of the little group of $\vec{k}$ (Appendix B) results in six allowed magnetic structures. Out of these six, only two magnetic structures correctly reproduce the observed intensity of the $(0, 0, 1/2)$ reflection. In these structures the magnetic moments in the chemical

[4] Since the cross section for paramagnetic scattering (4.31) is proportional to the magnetic form factor, it gives the most contribution at low κ values. Therefore, a decrease in background at low κ is an indication of a change in the magnetic ordering of the measured compound.

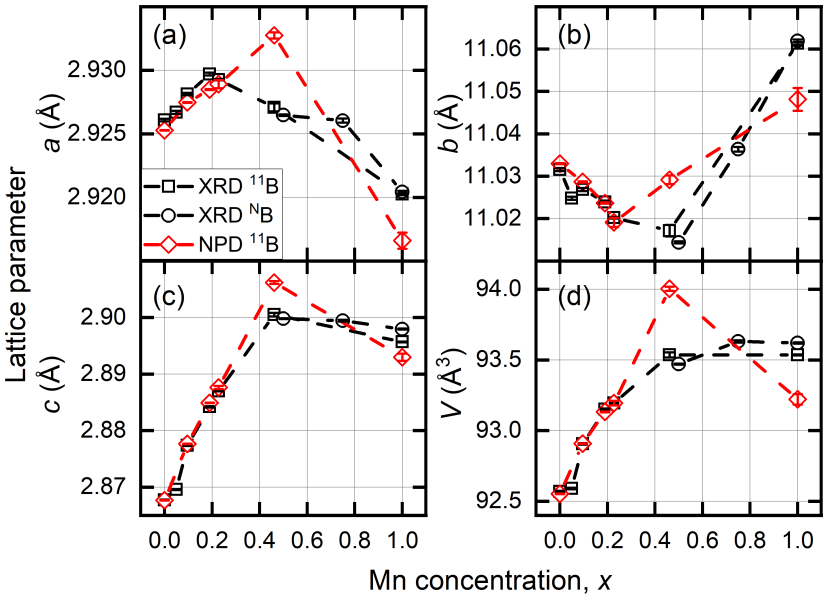

Figure 5.2: Refined LPs and unit cell volumes of $(Fe_{1-x}Mn_x)_2\,AlB_2$ powders at RT as function of x obtained from XRD (black symbols) and NPD (red symbols). (a), (b), and (c) show the a, b, and c LPs, respectively and (d) unit cell volume. Circles indicate measurements performed on natural B samples; squares indicate those performed on ^{11}B samples. Samples measured with NPD are plotted using the refined x.

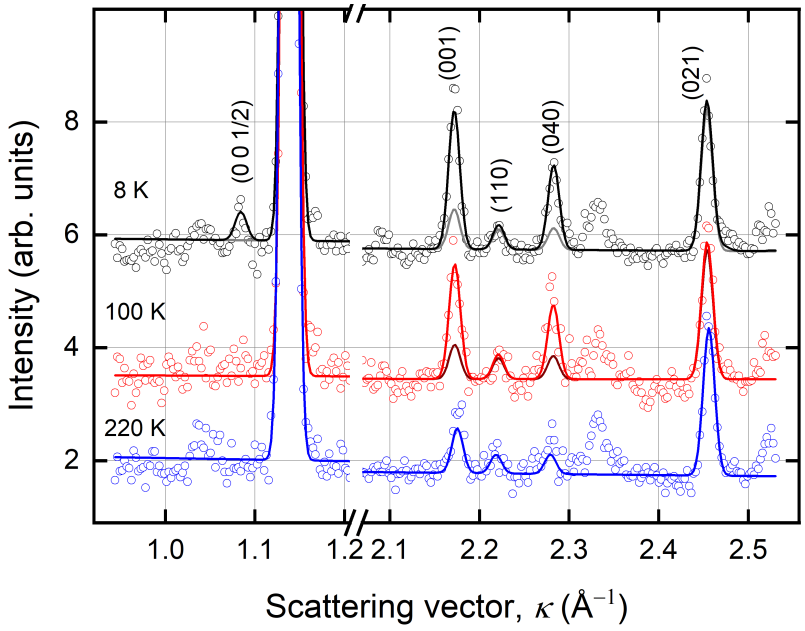

Figure 5.3: Observed NPD (symbols) of $(Fe_{0.8}Mn_{0.2})_2\,AlB_2$ at different temperatures and the corresponding Rietveld refinements (solid line). Solid gray and dark red lines at 8 K and 100 K, respectively, show the calculated profile due to the nuclear phase alone. Reflections are marked using their Miller indices and fractional Miller indices (for AFM reflections). The reflection at $\kappa \approx 2.35\,\text{Å}^{-1}$ belongs to an unidentified impurity phase and is excluded from the refinement.

unit cell are aligned ferromagnetically and can point either along the a (B_{3g}) or b (B_{2g}) axes. To decide which of the two structures has a better agreement with the data, the magnetic R-factors [53, 54, 56] of both structures are calculated using

$$R_{\text{mag}} = 100 \sum_{hkl} \frac{|I_{\text{obs}}\,(2\theta_{hkl}) - I_{\text{calc}}\,(2\theta_{hkl})|}{|I_{\text{obs}}\,(2\theta_{hkl})|}, \tag{5.3}$$

where hkl runs over magnetic reflections only, I_{obs} is the observed integrated intensity of a reflection and I_{calc} is the calculated integrated intensity given by (4.2). The advantage of using R_{mag} over the traditional χ^2 is that it is based only on the contributions of the magnetic phase, while χ^2 is dominated by reflections from the nuclear phase and the background. The calculated R-factors are 28 and 23 for moments directed along the a and b axes, respectively. This comparison gives the latter structure as the most likely solution. Indeed, magnetization measurements on Mn_2AlB_2 single crystals [57] have shown that the magnetic moments are aligned along the b axis.

Temperature evolution of the LPs for Fe_2AlB_2 [Figure 5.4(a)] shows an expansion of the c LP upon cooling below 310 K. Combined with the onset of FM

ordering below this temperature, it is reasonable to conclude that this anomalous thermal expansion originates from magnetostriction, as shown by Ke *et al* [12] using DFT calculations, which have shown a strong dependence of the magnetic moment in Fe_2AlB_2 on the c LP. The changes in the LPs over most of the x range are of the order of 0.25%. A similar behavior is observed for the $x = 0.1$ and 0.2 samples, while an expansion of the b LP upon cooling is observed for $x = 1$. For $x = 0.5$ [Figure 5.4(b)], the c LP contracts below 200 K and expands below 100 K. This change in behavior is attributed to the FM transition observed at ≈ 130 K. Except $x = 1$, the unit cell volume contracts below the ordering temperature, while for $x = 1$, the volume expands. The change of LPs with temperature is comparable to the change with x for the a and b LPs, however the c LP increases by 1% with increasing x, thus showing a stronger dependence on x.

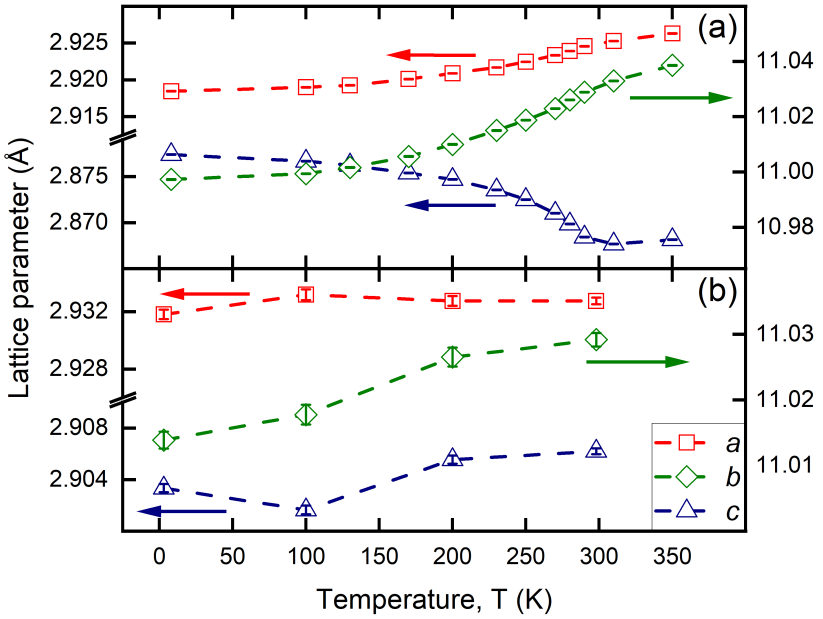

Figure 5.4: Temperature evolution of the a and c LPs (left ordinate) and b (right ordinate) of (a) Fe_2AlB_2 and (b) $(Fe_{0.5}Mn_{0.5})_2AlB_2$ as determined by NPD measurements.

5.2 Magnetization measurements

Temperature dependent magnetization curves (Figure 5.5) show varying magnetic responses for different x values. As temperature decreases, samples with $x < 0.5$ show an abrupt increase in magnetization, as expected for a FM. For $x = 0.5$, the increase in magnetization is not as abrupt, while for $x = 0.75$ and $x = 1$ the total magnetic moment is two orders of magnitude lower.

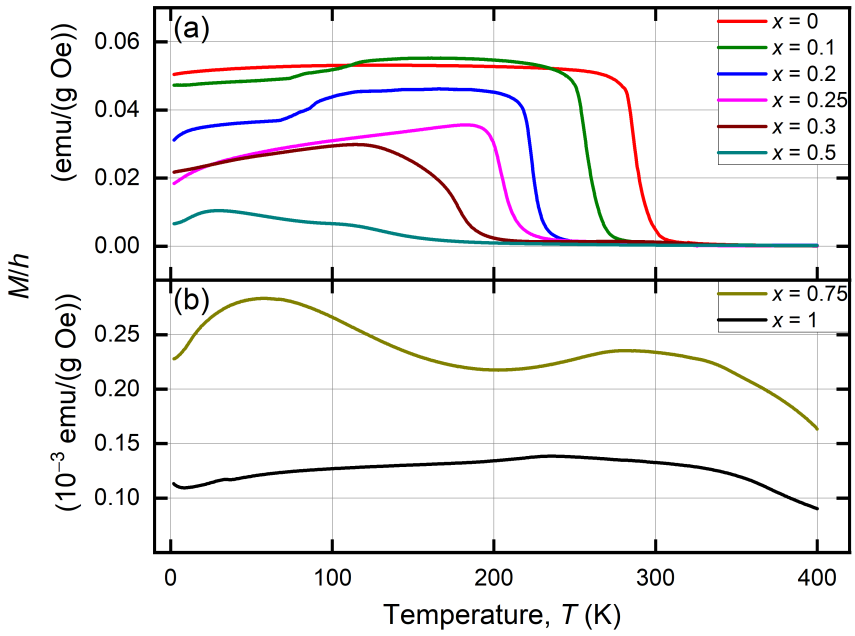

Figure 5.5: Zero field cooled magnetization of $(Fe_{1-x}Mn_x)_2\,AlB_2$ for (a) $x \leq 0.5$, and (b) $x > 0.5$.

Arrott plots (Figure 5.6) are used to determine the transition temperature of the FM component T_C [58]. In an Arrott plot, the field dependent magnetization is plotted as h/M vs M^2. By expanding the thermodynamic potential Φ to fourth order and including an external magnetic field, we can write

$$\Phi = \Phi_0 + aM^2 + bM^4 + O\left(M^6\right) - hM. \tag{5.4}$$

At equilibrium $\partial\Phi/\partial M = 0$ and therefore

$$2aM + 4bM^3 + O\left(M^5\right) = h. \tag{5.5}$$

This gives the relation

$$h/M = 2a + 4bM^2 + O\left(M^4\right). \tag{5.6}$$

By fitting the tail (large M part) of the Arrott plot to a straight line, we can remove higher order terms. Since $a = 0$ when $T = T_C$, we expect to obtain a straight line which passes through the origin in the Arrott plot. To find T_C, first, (5.6) is fitted to the tail of the Arrott plot at each temperature. Then, the temperature at which $a\,(T)$ goes through zero is found from linear interpolation. The obtained T_C's are given in Table 5.2. For $x = 0.5$, no field dependent measurements close to T_C were available and therefore extrema in dM/dT were used to identify temperatures of magnetic events. Bounds on T_N of the AFM phase

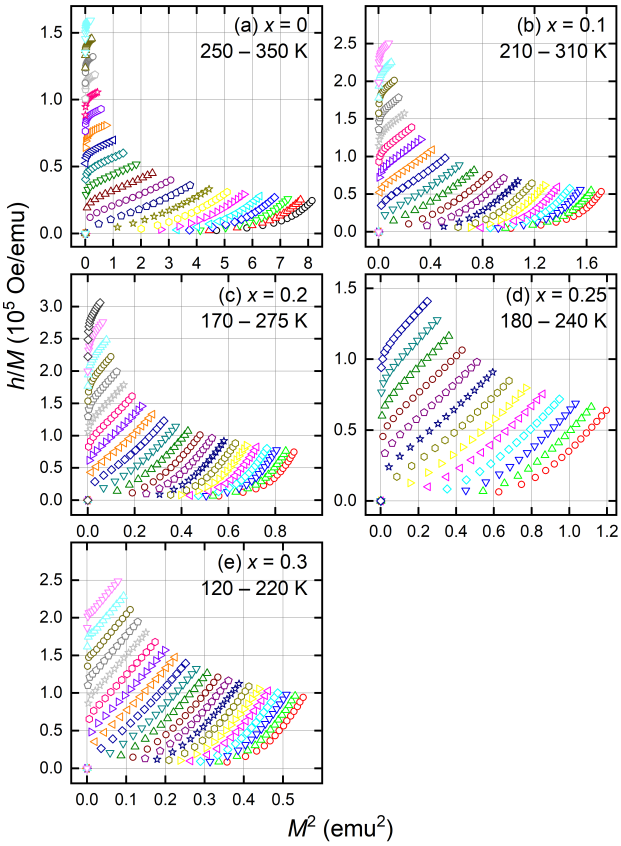

Figure 5.6: Arrott plots for $(Fe_{1-x}Mn_x)_2\,AlB_2$ with $x =$ (a) 0, (b) 0.1, (c) 0.2, (d) 0.25, and (e) 0.3. The temperature step in each sample is 5 K and the measured temperature range is written in each panel.

are obtained from NPD measurements as the FM phase completely dominates the bulk magnetization observed using magnetization measurements.

The saturated average magnetic moment at 2 K (Table 5.2) is obtained from high field magnetization [Figure 5.7(a)] by linear extrapolation of M as function of $1/h$ curves to $h = 0$ (not shown). The number of data points to include in the linear fit was reduced until the sum of squared residuals (χ^2) did not change. To estimate the magnetocaloric properties of the sample, the isothermal entropy change [Table 5.2, Figure 5.7(b)] is calculated by numerically integrating (3.26):

$$\Delta\mathcal{S}_m\,(T,h) \approx \sum_{i=0}^{n-1} \frac{M_i - M_{i-1}}{T_i - T_{i-1}}\,(h_i - h_{i-1})\,. \tag{5.7}$$

The maximum relative cooling power (RCP, Table 5.2) is estimated by mul-

tiplying the maximal value of $\Delta\mathcal{S}_m$ by the full width at half maximum (FWHM) of the measured $\Delta\mathcal{S}_m$ curve as a function of T [Figure 5.7(b)] [59]. The calculated RCP of Fe_2AlB_2 for a field change of 0-2 T and 0-5 T are 75 and 210 J/kg, respectively and are in agreement with results obtained in the literature [6, 60].

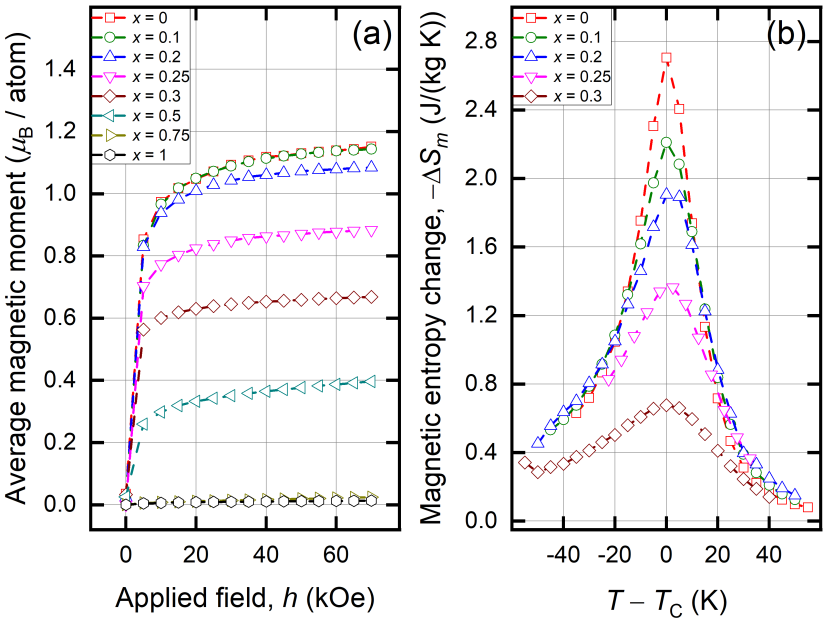

Figure 5.7: (a) Field dependent average magnetic moment of $(Fe_{1-x}Mn_x)_2\,AlB_2$ at 2 K as function of x. (b) Isothermal magnetic entropy change for a field change of 0–20 kOe as function of the relative temperature.

Table 5.2: Transition temperatures (T_{C} and T_{N}), saturated average magnetic moment at 2 K, magnetic entropy change ($\Delta\mathcal{S}_m$), and relative cooling power (RCP). Numbers in brackets indicate statistical 1σ uncertainties, while uncertainties denoted using $\pm$ indicate upper and lower bounds. Dashes indicate irrelevant data.

x	T_{C} (K)[a]	T_{N} (K)[b]	M_{sat} (μ_{B})	$-\Delta\mathcal{S}_m$ (J/kg K) 2 T/5 T	RCP (J/kg) 2 T/5 T
0[c]	292.4(2)	—	1.19(6)	2.7/5.7	75/210
0.096(4)[c]	264.6(3)	—	1.18(6)	2.2/4.6	79/218
0.190(2)[c]	231.4(3)	80 ± 20	1.12(6)	1.9/4.0	80/226
0.228(4)[c]	212.25(5)	150 ± 100	0.9(1)	1.4/2.9	70/190
0.30(2)[d]	183.16(6)	—	0.70(4)	0.7/1.4	41/117
0.461(3)[c]		350 ± 50			
0.50(5)[d]	130(5)		0.454(3)		
1[c] [14]	—	313 [57]			

[a] Critical temperature of the FM component as determined by Arrott plots.
[b] Critical temperature of the AFM component as estimated by NPD measurements.
[c] ^{11}B sample.
[d] Natural B sample.

5.3 Theoretical modelling based on mean field theory

The observed magnetic reflections in the NPD measurements (Figure 5.3) indicate that the magnetic structure of $(Fe_{1-x}Mn_x)_2\,AlB_2$ is composed of two parts. A FM moment, which points along the crystallographic a axis, and an AFM moment, which points along the crystallographic b axis with a propagation vector of $\vec{k} = (0, 0, 1/2)$. The temperature evolution of each magnetic moment [Figure 5.8(a), symbols] shows a gradual decrease, typical of a second order phase transition. The FM and AFM components, when present, have different critical temperatures and ground state magnitudes, that vary with x (Table 5.2). The phase diagram of $(Fe_{1-x}Mn_x)_2\,AlB_2$ [Figure 5.8(b), symbols] thus consists of three different phases. For $x < 0.23$ only a FM phase is present. For $0.23 < x \leq 0.46$, both FM and AFM phases are present, while for $0.46 < x \leq 1$ only an AFM phase is present. To investigate the magnetic moment as a function of x and T, we made use of the MFT results (3.22) adapted for $(Fe_{1-x}Mn_x)_2\,AlB_2$ (appendix C). The unknown parameters in the model are the g-factors and spins of the Fe and Mn atoms, and the exchange constants. Since the FM component is directed along the a axis, while the AFM component is directed along the b axis, we only need to consider the exchange constants along these directions.

This leaves us with 4 exchange constants, namely: $J^{xx}_{\text{Fe-Fe}}$, $J^{xx}_{\text{Fe-Mn}}$, $J^{yy}_{\text{Fe-Mn}}$, and $J^{yy}_{\text{Mn-Mn}}$. We assume the g-factors of the two atoms to be isotropic, i.e $g_X^{\alpha\beta} = g_X^0\delta^{\alpha\beta}$, where $X \in \{\mathrm{Fe}, \mathrm{Mn}\}$ and the fitting procedure is obtained

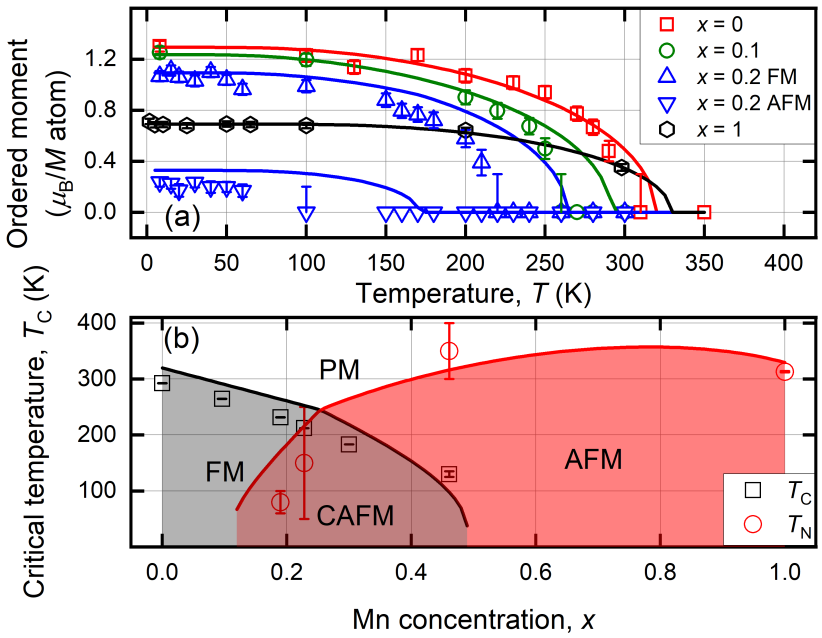

Figure 5.8: (a) Temperature evolution of observed ordered magnetic moment (symbols) in $(Fe_{1-x}Mn_x)_2\,AlB_2$. (b) Observed (symbols) and calculated (solid lines) critical temperature of the FM (black) and AFM (red) components as function of x. Different regions in the phase diagram are labeled by the magnetic phases present in them.

as follows. The values of S_{Fe} and S_{Mn} are scanned in the range $1/2 - 3$ in steps of $1/2$. For each pair $(S_{\mathrm{Fe}}, S_{\mathrm{Mn}})$, g_{Fe} and $J^{xx}_{\text{Fe-Fe}}$ are obtained by fitting $M\,(T)$ [Eq. (3.22)] to the observed oredered moment of Fe_2AlB_2, while g_{Mn} and $J^{yy}_{\text{Mn-Mn}}$ are obtained by fitting $M\,(T)$ to the observed moment of Mn_2AlB_2 [Figure 5.8(a)]. Next, $J^{xx}_{\text{Fe-Mn}}$ and $J^{yy}_{\text{Fe-Mn}}$ are fitted to best match $M\,(T)$ for $x = 0.1$, 0.2, 0.25, and 0.5 [Figure 5.8(a), solid line]. The χ^2 goodness of fit parameter is used to identify the best matching fit, while also requiring that the resulting values for the exchange parameters remain positive. The entire fitting procedure was performed twice where $J^{xx}_{\text{Fe-Mn}}$ and $J^{yy}_{\text{Fe-Mn}}$ were assumed to be FM or AFM for nearest neighbors along the c axis. Finally, the best matching parameters were obtained by calculating $M\,(x)$ at base temperature (BT, Figure 5.9). The only parameter set which predicted the existence of a non-zero FM moment for $x = 0.5$ was chosen as the best fit and is given in Table C.1. The sign of $J^{xx}_{\text{Fe-Fe}}$ and $J^{xx}_{\text{Fe-Mn}}$ is positive for nearest neighbors along all directions, while the sign of $J^{yy}_{\text{Fe-Mn}}$ and $J^{yy}_{\text{Mn-Mn}}$ is negative for nearest neighbors along the c axis.

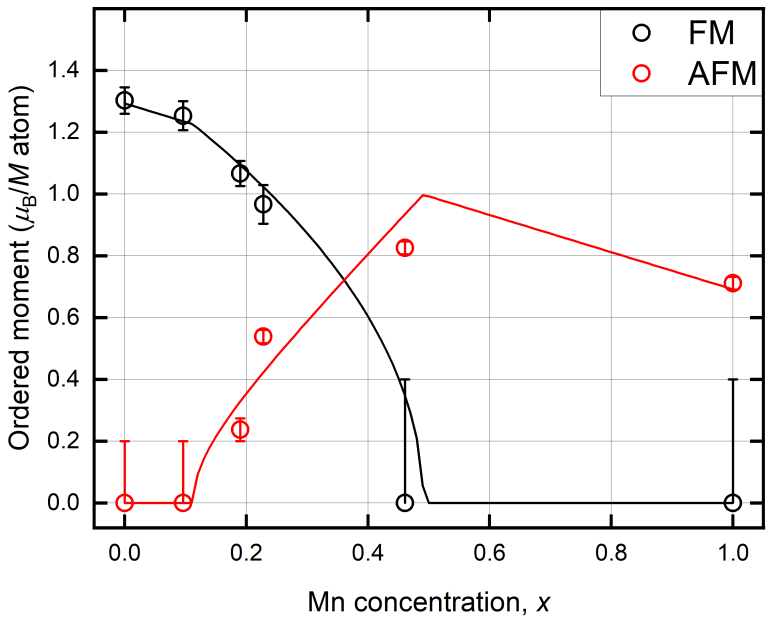

Figure 5.9: The observed ordered magnetic moment of $(Fe_{1-x}Mn_x)_2\,AlB_2$ at BT as function of x. Solid lines are fits to the data.

5.4 Discussion

The calculated magnetic phase diagram of the solid solution $(Fe_{1-x}Mn_x)_2\,AlB_2$ [Figure 5.8(b)] contains three types of ordered magnetic structures. A FM structure below a critical Mn concentration of $x_1 \approx 0.1$, an AFM structure above $x_2 \approx 0.5$ and a combination of both in between. This intermediate region is interpreted as a canted AFM. Because the LPs of Fe_2AlB_2 and Mn_2AlB_2 differ significantly (Figure 5.2), a separation of the sample into Fe-rich and Mn-rich clusters would produce two distinctly visible diffraction patterns. Since only a single diffraction pattern is observed, with no broadening of the crystallographic or magnetic reflections relative to the instrumental resolution, we conclude that the mixing of Mn in the sample is homogeneous and that the observed combination of a FM (along a) and AFM (along b) structures is to be interpreted as a canting of the FM moments.

The canting angles, in the a-b plane relative to the b axis, at BT are estimated to be 13(2) ° and 29(2) ° for $x = 0.19$ and 0.23, respectively. The general features of this phase diagram are qualitatively well described by MFT [Figure 5.8(b), solid lines], although quantitative agreement is far from perfect. Previous DFT calculations have concluded that the AFM configuration becomes more stable than the FM configurations for $x > 0.2$ [12]. This result agrees with the observed NPD results, but places a higher bound on the critical x than MFT. We note that unlike previous reports [8, 13], no evidence for a disordered magnetic phase

was found. The overestimation of T_C and T_N in the calculated model, may partly be a result of the mean field approximation, which is known for giving overestimates for critical temperatures [33].

The Fe-Mn and Mn-Mn couplings are found to be negative for neighbors along the c axis, which is also the shortest axis. This suggests that the magnetic interaction between the Fe and Mn atoms is a direct exchange interaction, since this interaction is known to change sign from FM to AFM with decreasing interatomic distance as described by the Bethe-Slater curve [61]. This suggestion is corroborated by DFT calculations which have shown that the Mn-Mn exchange coefficients are negative along the c axis but are positive along the a axis. Since the a axis is longer than the c axis by only 0.02 Å, we can obtain an estimate on the critical Mn-Mn distance to be in the 2.89–2.92 Å range.

The anomalous variation of the LPs with T (Figure 5.4) and x (Figure 5.2) indicates a strong magnetoelastic interaction. This variation in interatomic distances in turn influences the strength of the exchange interaction between the magnetic M atoms, giving rise to a complicated dependence of the ordered magnetic moment on T and x (Figure 5.8). These subtleties were not considered in our simplified model. In addition, the magnetoelastic interaction in these compounds is highly anisotropic, as can be seen from the qualitatively different temperature evolution of the LPs (Figure 5.4). For $x \leq 0.5$ the magnetic moment is highly affected by the c LP, causing an anomalous expansion upon cooling. A similar dependence was observed in Mn_2AlB_2 for the b LP and indicated a change in the anisotropy of the magnetoelastic interaction [14].

The addition of Mn into Fe_2AlB_2 decreases the ordered FM moment, that in turn decreases the overall magnetocaloric effect (Table 5.2). However, the maximum in the magnetic entropy change occurs over a broader temperature range [Figure 5.7(b)] resulting in a 6% increase in the estimated RCP (Table 5.2). The addition of Mn does not seem to broaden magnetic transition, as can be observed from the temperature evolution of the ordered magnetic moment [Fig 5.8(a)]. Additionally, since, as discussed above, the introduction of Mn does not produce multiple phases in the sample but is admixed homogeneously, we can conclude that the broadening of the MCE curve is not caused by chemical disorder but rather by the introduction of competing AFM interactions, which are theoretically known to broaden the range of the MCE [62]. Addition of 10% Mn decreases T_C from ≈ 290 K to ≈ 260 K while the effective temperature range (FWHM) of the MCE stays at ≈ 30 K. This enables control over T_C in the RT range without a substantial loss of cooling power. For example, mixing multiple $(Fe_{1-x}Mn_x)_2 AlB_2$ compounds with different x can form a combined MCE curve with a desired shape, which is controlled by the ratio of different compounds and their respective T_C's.

6 Results and analysis of RE-*i*-MAX measurements

6.1 Ground state neutron powder diffraction

NPD patterns of $\left(Mo_{2/3}RE_{1/3}\right)_2 AlC$ with RE = Nd, Tb, Ho, and Er are collected at temperatures that range from the available BT up to the magnetic transition temperature and into the PM phase. Upon cooling, additional reflections, originating from magnetic diffraction are observed for each compound. To isolate the magnetic contribution from the crystallographic reflections, the difference between BT and PM temperatures is calculated (Figures 6.1 and 6.2) and analyzed first.

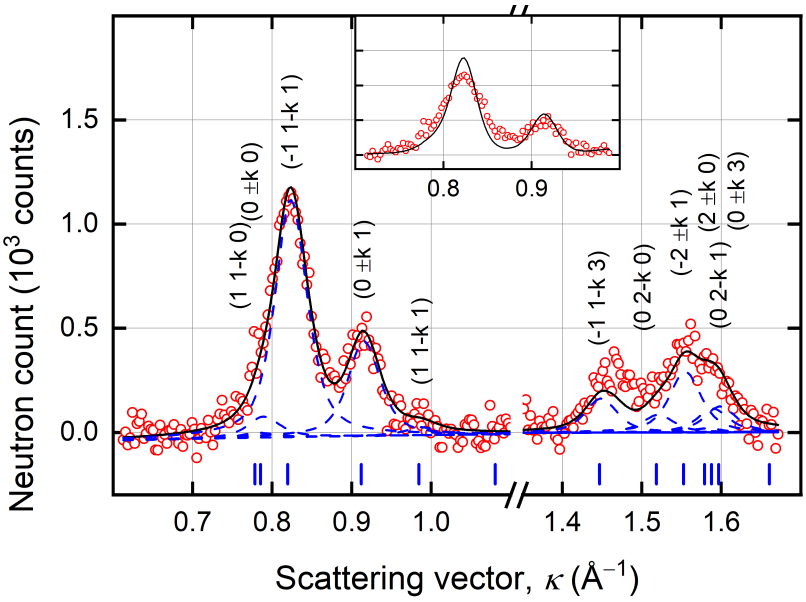

Figure 6.1: Difference in the observed (symbols) neutron count of $\left(Mo_{2/3}Er_{1/3}\right)_2 AlC$ between 1.6 K and 10 K and the Rietveld refined profile (solid black line). Magnetic reflections are labeled by Miller indices, with their contribution to the diffraction pattern shown as dashed lines and tick marks. Inset shows the calculated profile without including Lorentzian broadening (see text).

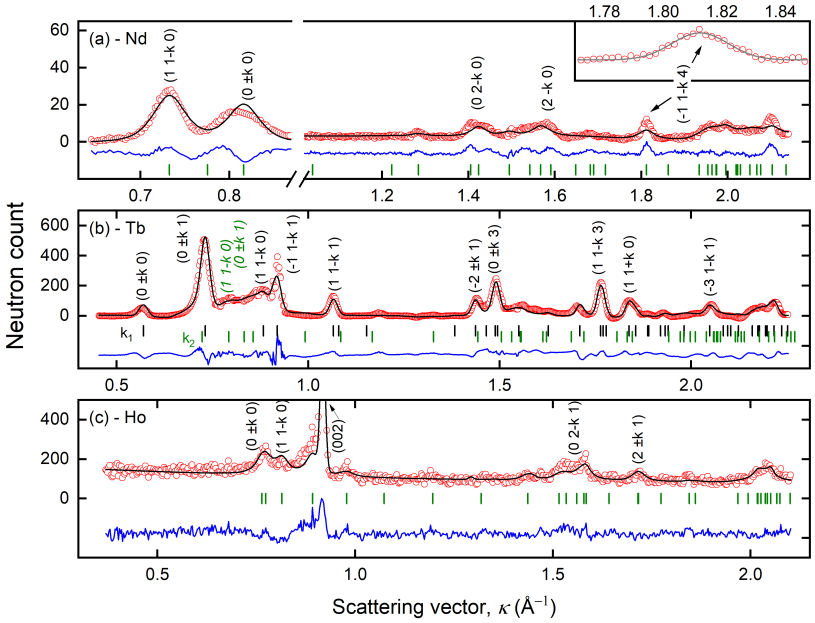

Figure 6.2: Neutron count difference (symbols) between (a) 1.5 K and 10 K for RE = Nd and (b) 3.5 K and 30 K for RE = Tb. (c) Observed neutron count for RE = Ho at 4 K. The Rietveld refined profile is shown as a solid black line and its difference from the observed data is given by a solid blue line. Magnetic reflections are denoted by Miller indices and shown as tick marks. Inset in (a) zooms in on the $(-1\ 1-k\ 4)$ reflection and shows a Gaussian fit used to obtain integrated intensity. RE = Tb contains reflections from both $\vec{k}_1$ and $\vec{k}_2$ (denoted using italics, and bottom tick marks). In (c) the crystallographic (002) reflection is also visible.

First, a propagation vector search on the difference pattern is performed using the `SARAh` package [63]. Due to the low symmetry and large unit cell of $\left(Mo_{2/3}RE_{1/3}\right)_2 AlC$, the magnetic reflections are strongly overlapping (Figure 6.1). This makes conventional indexing methods (such as the `k-search` routine implemented in the `FULLPROF` suite [53]), which require knowledge on the exact number of reflections and their position, unreliable. `SARAh` performs a brute force test of high symmetry points and lines in the Brillouin zone, which serve as likely candidates for the propagation vector. For each tested propagation vector, the magnetic structure is refined using a simulated annealing based χ^2 minimization instead of a gradient based method. Simulated annealing, which is monte-carlo based is better suited for problems with a large number of local minima, such as refinement of a magnetic structure with a large number of magnetic atoms without any symmetry constraints.

In the first step, only high symmetry points in the Brillouin zone of the *i*-MAX were tested and no matching results were found. In the next step, a

search along high symmetry lines with parameterization $(0, k, 0)$ and $(0, k, 0.5)$ is performed. The most likely candidates for k are those for which the χ^2 of the refinement is minimal. Possible magnetic structures for the k-vector candidates are obtained from symmetry analysis wich is given in detail in appendix D. The basis vector coefficients and k-vector are then refined to match the observed magnetic diffraction pattern.

Refinement of the BT magnetic structures reveals that the magnetic ground states of compounds with RE = Nd, Tb, Ho, and Er are SDWs with propagation vectors $\vec{k}_{\mathrm{RE}}$ parallel to the crystallographic b axis [Figure 6.3(a)]. The magnetic moments of the RE atoms are aligned perpendicular to $\vec{k}_{\mathrm{RE}}$ with magnetic directions varying with RE [Figure 6.3(b)]. Three different magnetic configurations in the unit cell are identified and labeled using Bertaut notation [64] as $\mathrm{F_xF_z}$ [Figure 6.3(b), RE = Nd], $\mathrm{C_xC_z}$ [Figure 6.3(b), RE = Tb, Er], and $\mathrm{C_xF_z}$ [Figure 6.3(b), RE = Ho]. All three configurations are obtained from the Γ_2 representation (appendix D), where the magnetic moments on RE atoms 1 and 2 [Figure 6.3(b)] are parallel and are oriented in the a-c plane.

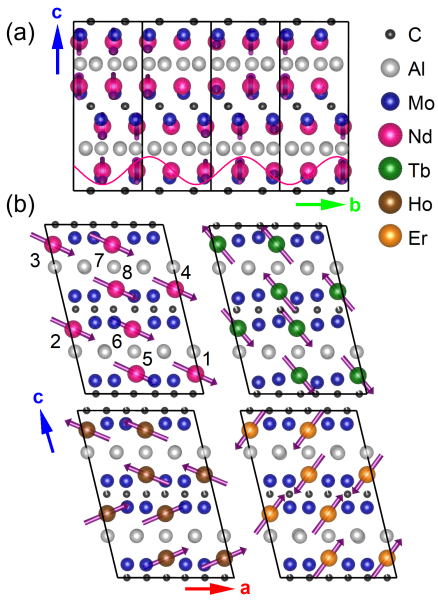

Figure 6.3: (a) Depiction of the SDW structure for $\left(\mathrm{Mo_{2/3}Nd_{1/3}}\right)_2\mathrm{AlC}$ in the b-c plane. (b) Unit cell spin configurations of $\left(\mathrm{Mo_{2/3}RE_{1/3}}\right)_2\mathrm{AlC}$ at base temperature. The spin configuration for $\left(\mathrm{Mo_{2/3}Tb_{1/3}}\right)_2\mathrm{AlC}$ shows the commensurate $\vec{k}_1 = (0, 0.5, 0)$ structure. The modulation in the magnetic moment magnitude acquired from the propagation vector (see text) is removed in this figure and all magnetic moments are rescaled for clarity. Numbers in (b) indicate order of magnetic atoms according to the international tables for crystallography.

Attempting to refine the BT profile of RE = Er and Ho using the instrumental resolution, resulted in calculated reflections which are narrower than the observed reflections (Figure 6.1, inset). To obtain a better fitting peak shape, an additional Lorentzian contribution is added to the magnetic reflections (`FULLPROF` Y parameter [54]). The magnetic correlation length ξ is then estimated using the Scherrer formula $\xi = 0.8\lambda/Y$ [65]. For RE = Nd and Tb, no additional broadening is observed within the limits of the instrumental resolution, and thus cannot be determined, and assumed to match the crystallographic correlation length. RE = Nd shows the weakest reflections and has the worst agreement factor (Table 6.1). To limit the number of refined parameters, the magnetic moments in RE = Nd are constrained to lie in the a-c plane in accordance with the other $\left(Mo_{2/3}RE_{1/3}\right)_2 AlC$ phases.

Table 6.1: Refined magnetic structure parameters for measured $\left(Mo_{2/3}RE_{1/3}\right)_2 AlC$ phases. T_N is the Néel temperature, BT is the base temperature at which the measurement is performed, m is the ordered magnetic moment per atom, θ is the orientation of the magnetic moment relative the z axis [see Figure 3(c)], k is the propagation vector component along the b axis, ξ is the magnetic correlation length and R_{mag} is the magnetic agreement factor given in (5.3). Numbers in parenthesis indicate statistical 1σ uncertainty, while $\pm$ indicates systematic uncertainty. Dash indicates that the data falls below the detection limit.

RE	T_N (K)[22]	BT (K)	m_{RE} (μ_B/RE)	θ_{RE} (deg)	k_{RE}	ξ_{RE} (nm)	R_{mag}
Nd	7.6	1.5	1.76(2)	115(2)	0.730(2)	—	40
Gd	26		6.6 ± 0.3	120 ± 7	0.5	—	—
Tb	20.1	3.5	5.63(3)	132(2)	0.5	—	14.7
	28		3.1(1)	126(2)	0.636(1)	—	29.2
Ho	7.8	4	8.7(2)	67(1)	0.6717(7)	16(1)	16.3
Er	3.6	1.6	6.54(6)	36.6(9)	0.6787(3)	20.8(9)	5.57

6.2 Ground state muon spin rotation

The asymmetry in the decay positrons (4.39) at BT and zero applied field of different $\left(Mo_{2/3}RE_{1/3}\right)_2 AlC$ samples is plotted in Figures 6.4(a) and 6.4(b). Three distinct behaviors are observed: a) RE = Nd shows oscillations which closely resemble a Bessel function. b) Similarly, RE = Gd shows oscillations which are well described by a cosine function. c) In contrast, other REs show exponential decay which is characterized by a fast component ($t < 0.1\,s$) and a slow component. For all compounds, the asymmetry signal decays to zero at long times ($\approx 3\,s$, not shown) and does not show the characteristic 1/3 component of powders, had there been a static magnetic field parallel to the muon spin [Eq. (4.40)]. Fourier transforms of the observed asymmetry in RE = Nd and Gd [Figure 6.4(c) and 6.4(d)] show one dominant field in each sample, namely 0.35 T and 1.4 T for RE = Nd and Gd, respectively. The broadened field spectrum of

RE = Nd is characteristic of an incommensurate magnetic structure [Eq. (4.45)], while a single well-defined peak in the RE = Gd field spectrum corresponds to a simple commensurate structure (FM or AFM) [(Eq. (4.41)]. The data is therefore fitted to (4.47) with $\mathbb{F}(x) = J_0(x)$ for RE = Nd, $\mathbb{F}(x) = \cos(x)$ for RE = Gd and $\mathbb{F}(x) = 1$ for the rest.

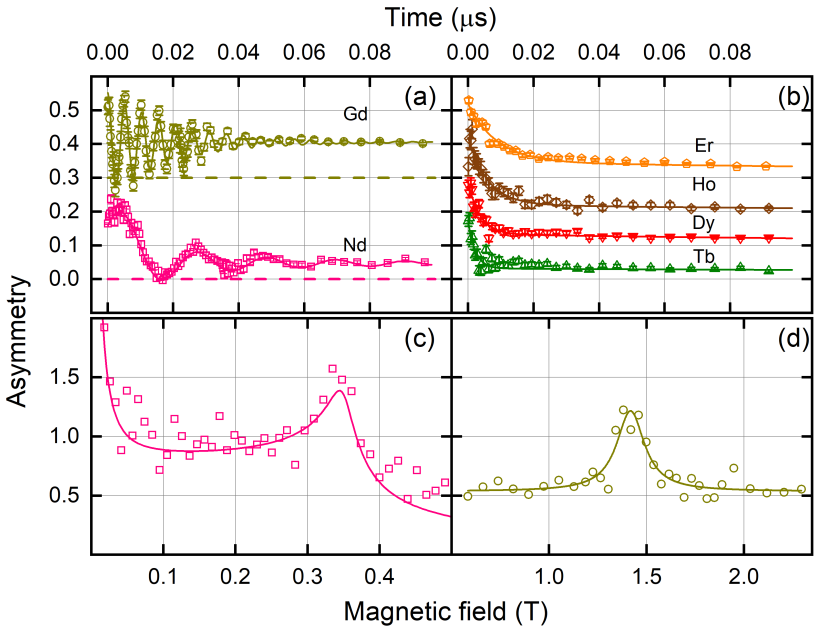

Figure 6.4: Observed BT asymmetry (symbols) of (a) RE = Nd and RE = Gd, (b) RE = Tb, Dy, Ho, and Er powder samples. Data in (a) and (b) is shifted for clarity (for RE = Gd by 0.3 and for RE = Dy, Ho and Er by 0.1, 0.2, and 0.3, respectively). Dashed lines in (a) indicate zero asymmetry for each data set. Magnetic field distribution for (c) RE = Nd and (d) RE = Gd obtained by Fourier transforming the data in (a). Solid lines show fits to the data.

Time dependence of the muon asymmetry of a single crystal sample of RE = Gd is recorded using two perpendicular pairs of detectors (Figure 4.3). The first, forward - backward (FB) detectors measure the muon polarization along the muon momentum direction (z axis). The second, up - down (UD) detectors measure the muon asymmetry perpendicular to the muon momentum (x axis). BT asymmetry of the RE = Gd single crystal sample is recorded for different initial muon spin angles ζ and is shown, after background subtraction, in Figure 6.5. Analysis of the single crystal data is described in Sec. 6.4 and 6.5.

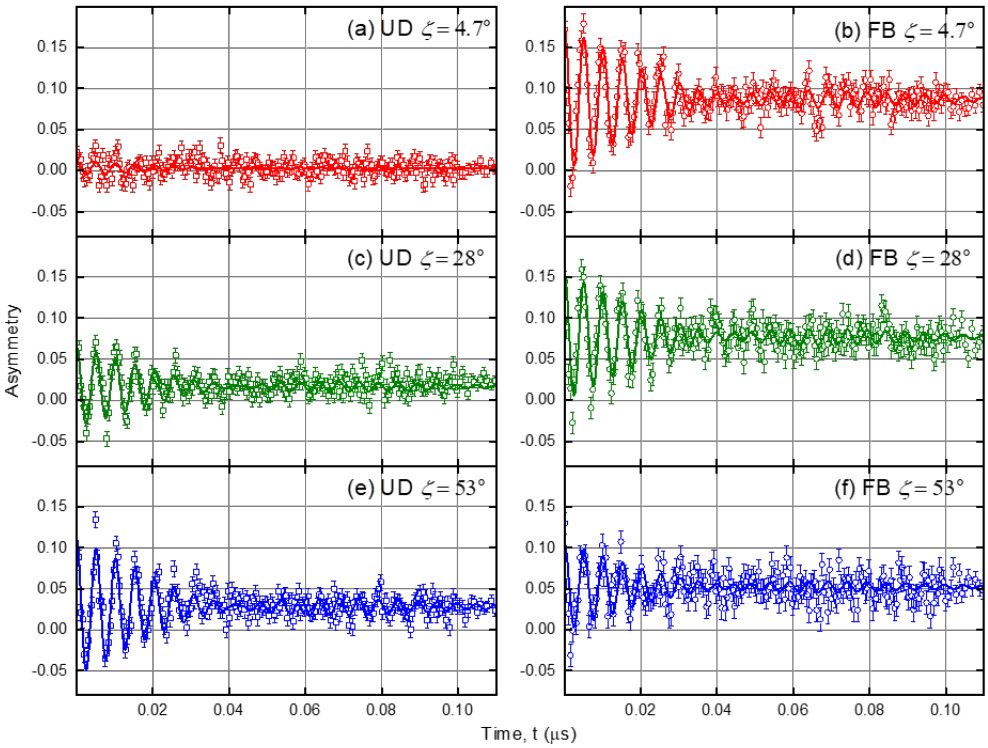

Figure 6.5: Time dependence of the BT asymmetry (after background subtraction) for different initial muon spin angles ζ. Left column shows the up-down detectors and right column – the forward-backward detectors. Solid lines are fits to equations (4.54) and (4.55).

6.3 Muon site determination

In order to convert the magnetic field distribution experienced by the muon into the magnetic moment distribution, the muon site has to be determined [66]. This is done in three steps. First, the stable muon site in RE = Nd is determined using an adaptation of DFT which allows relaxation of the lattice in the presence of the muon. Second, the expected magnetic moment is calculated using μSR results and compared to the NPD results to verify the validity of the DFT approach. Finally, the same procedure is applied to RE = Gd where the magnetic structure is not determined by NPD. The search for a candidate site is obtained by treating the (positive) muon as a hydrogen impurity. It is then implanted in 27 different positions in the asymmetric unit of the i-MAX unit cell and the atomic positions are relaxed by minimizing the forces (3.42) acting on them.

In RE = Nd, two candidate muon sites are obtained. They are labeled as A [Figure 6.6(a)] with fractional coordinates (0.438, 0.111, 0.250) and B [Figure 6.6(b)] with fractional coordinates (0.343, 0.114, 0.362). The two sites have nearly degenerate energy ($\approx 20\,\text{meV}$). In contrast, for RE = Gd site A with coordinates (0.448, 0.087, 0.250) has the lowest energy by a margin of more than 100 meV. DFT calculations for other REs yield site A as the lowest energy site as well.

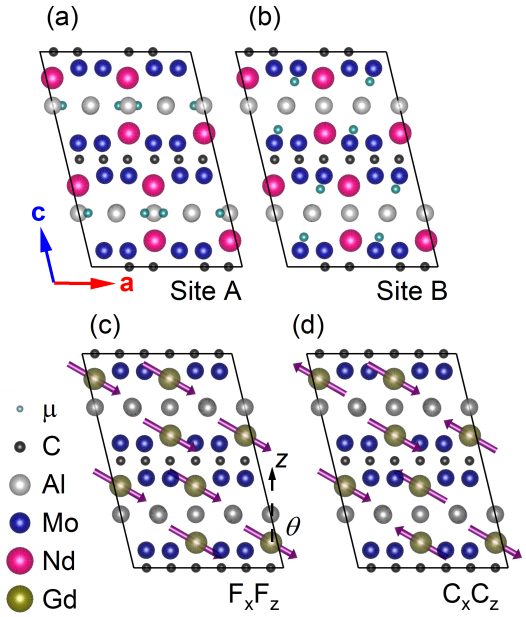

Figure 6.6: Lowest energy muon site A (a) and muon site B (b) shown as dark cyan spheres. (c) The magnetic F_xF_z configuration for RE = Gd in the a-c plane and the geometric definition of the magnetic angle θ. (d) The magnetic C_xC_z configuration.

After the determination of candidate muon sites in RE = Nd, the magnetic moment is calculated by assuming a given magnetic structure. The magnetic field at the muon site is calculated by summing dipolar contributions

$$\vec{B}_\mu = \sum_i \frac{3\hat{r}\,(\vec{m}_i \cdot \hat{r}) - \vec{m}_i}{r^3} \tag{6.1}$$

from neighboring atoms positioned around the muon site. In (6.1), $\hat{r}$ is a unit vector pointing from the muon site to the i'th atom and $\vec{m}_i$ is the magnetic moment of the i'th atom. Following the refinement strategy of the NPD data, four magnetic configurations, based on the basis vectors, namely F_xF_z [Figure 6.6(c)], G_xG_z, C_xC_z [Figure 6.6(d)], and A_xA_z, are considered. For each configuration, the moments are constrained to lie in the a-c plane. A magnetic moment at site i is then given by

$$\vec{m}_i = m_{\mathrm{SDW}}\,(\sin\theta_{\mathrm{RE}}\hat{x} + \cos\theta_{\mathrm{RE}}\hat{z})\cos\left(2\pi\vec{k}_{\mathrm{RE}}\cdot\vec{r}_i + \psi_{\mathrm{RE}}\right), \tag{6.2}$$

where m_{SDW} is the SDW amplitude, θ_{RE} is the magnetic moment angle relative to the Cartesian z axis [Figure 6.6(c)], $\vec{k}_{\mathrm{RE}}$ is the propagation vector, $\vec{r}_i$ is the

position of the i'th ion and ψ_{RE} is a global magnetic phase. Since the magnetic structure of RE = Nd is incommensurate, ψ_{RE} is arbitrary and can be set to zero. A scan over θ_{Nd} is performed and m_{SDW} corresponding to each θ_{Nd} is then calculated by matching the calculated magnetic field at the muon site to the observed field [Figure 6.4(c)]. Among the resulting m_{SDW}-θ_{Nd} curves for muon site A [Figure 6.7(a)], only the $\mathrm{F_xF_z}$ configuration contains a (m_{SDW}, θ_{Nd}) pair which matches the results obtained from NPD [Figure 6.7(a), pink rectangle]. For muon site B, all calculated curves [Figure 6.7(b)] require $m_{\mathrm{SDW}} > 2\,\mu_{\mathrm{B}}$/Nd and thus do not intersect the NPD result. This indicates that even in the RE = Nd compound, site A seems to be the stable muon site and, it is concluded that site A is the most likely muon site candidate in all $\left(\mathrm{Mo_{2/3}RE_{1/3}}\right)_2\mathrm{AlC}$.

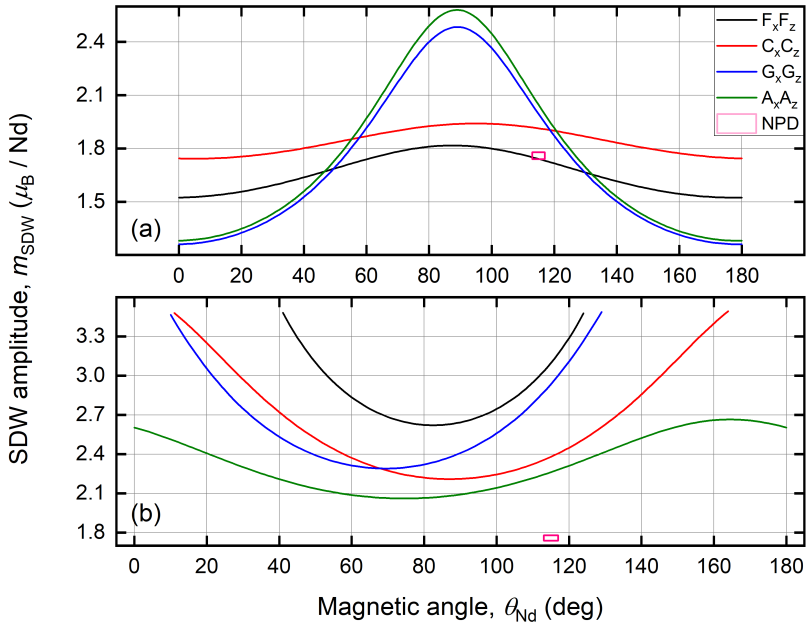

Figure 6.7: Calculated SDW amplitude for RE = Nd as function of moments' direction θ_{Nd} for different spin configurations assuming (a) muon site A and (b) muon site B. The NPD result (Table 6.1) is given as a pink rectangle indicating uncertainties on the refined value.

6.4 The magnetic structure of $\left(\mathrm{Mo_{2/3}Gd_{1/3}}\right)_2\mathrm{AlC}$

To determine the most likely magnetic structure for RE = Gd, a similar process to the one described for RE = Nd is performed. To limit the number of candidate magnetic structures, several constraints are placed on the magnetic moments in the RE = Gd unit cell. First, since there is only a single dominant frequency in the RE = Gd field spectrum [Figure 6.4(d)], it can be safely assumed that the periodicity of its magnetic structure is commensurate with

the crystal lattice. Because all $\left(Mo_{2/3}RE_{1/3}\right)_2 AlC$ phases in this study are isostructural, it is reasonable to assume that the propagation vector for RE = Gd has the same form as for the other compounds, i.e (0, k_{Gd}, 0). Moreover, a single magnetic field requires k_{Gd} to be either 0 or 1/2 as the magnetic moment magnitude must stay constant between adjacent unit cells.

Second, the possible spin configurations in the unit cell are limited to the four configurations tested for RE = Nd. These configurations ensure that atoms 1–4 in the unit cell [Figure 6.3(b)] have the same magnetic moment, as required to produce a single magnetic field in all muon sites and are compatible with both $k_{Gd} = 0$ and $k_{Gd} = 1/2$ periodicities. Third, since the magnetic moments in compounds with RE = Nd, Tb, Ho and Er are oriented within the a-c plane, the same constraint is imposed on RE = Gd. The magnetic structure of RE = Gd is therefore described by three parameters: m_{SDW}, θ_{Gd}, and ψ_{Gd} together with the magnetic configuration which describes the relative signs of the magnetic moments between different Gd atoms in the unit cell.

An attempt to directly fit m_{SDW}, θ_{Gd} and ψ_{Gd} to the powder data yields unstable results, since powder samples lose all information regarding the direction of the magnetic field, and therefore the fit is overparametrized. Instead, a brute force scan of θ_{Gd} and ψ_{Gd} in the ranges $0^\circ \leq \theta_{Gd} \leq 180^\circ$ and $-90^\circ \leq \psi_{Gd} \leq 90^\circ$ is performed. Results consistent with the asymmetry of the powder sample [Figures 6.4(a) and (d)] are selected based on two conditions, which are labeled as (i) and (ii). The physical magnetic moments on the Gd atoms m_{Gd} are given by $m_{SDW} \sin\psi_{Gd}$ or $m_{SDW} \cos\psi_{Gd}$ depending on the atomic position. Condition (i) is therefore $m_{Gd} \leq 7\,\mu_B$, which ensures physical magnetic moments on the Gd atoms. The second condition is obtained from the field distribution in the powder sample [Figure 6.4(d)]. The FWHM of the field distribution is obtained by fitting it to a Lorentzian and is approximately 0.05 T. Since muons positioned at different muon sites j can experience different magnetic fields B_j, condition (ii) is $\Delta B \equiv \max_j B_j - \min_j B_j \leq 0.05\,\mathrm{T}$. Magnetic structures, which give magnetic field distributions consistent with conditions (i) and (ii), are found only for the F_xF_z and C_xC_z configurations (Figure 6.8). For each configuration, conditions (i) and (ii) are obeyed in four branches in the θ_{Gd}–ψ_{Gd} plane. In general, the magnetic moment is found to vary between $5\,\mu_B$ and $7\,\mu_B$, θ_{Gd} varies between 0°–60° or 110°–180°, while ψ_{Gd} is centered around 45° and 50° for F_xF_z, and around 40° or 45° for C_xC_z.

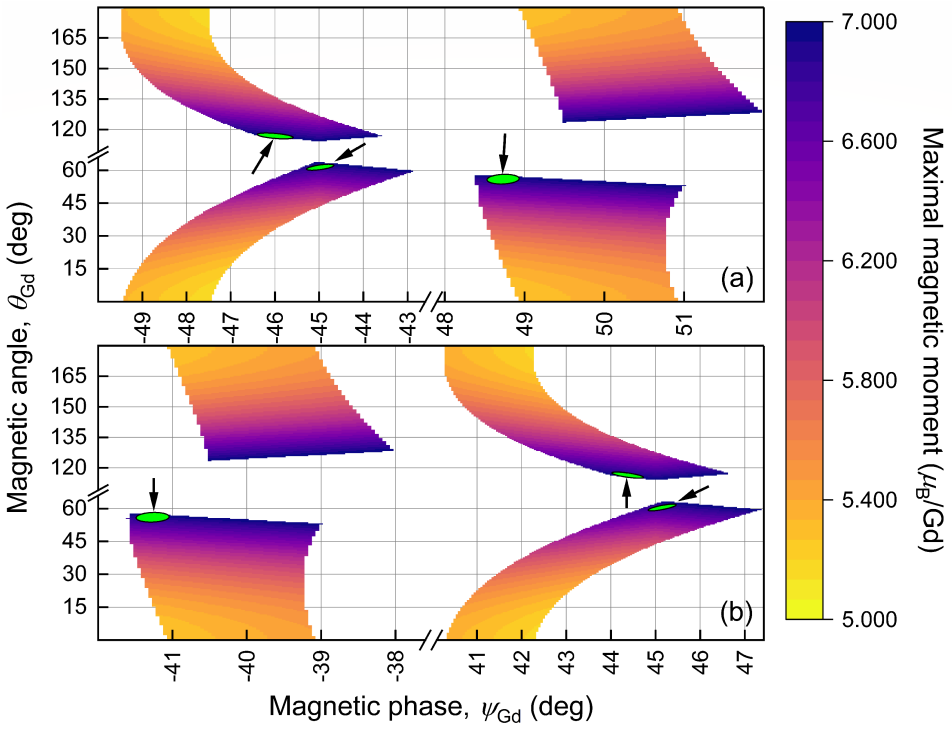

Figure 6.8: Calculated maximal magnetic moment for $\left(Mo_{2/3}Gd_{1/3}\right)_2 AlC$ as function of θ_{Gd} and ψ_{Gd}. The calculations are performed assuming magnetic configuration (a) $F_x F_z$ and (b) $C_x C_z$. Colored areas show regions consistent with conditions (i) and (ii) that are required to reproduce the observed magnetic field distribution (see text). Green ellipses show 95% confidence regions for magnetic structure parameters obtained by fitting the μSR data measured from RE = Gd single crystal sample (see text).

To fit the single crystal data (Figure 6.5), initial magnetic structure parameters are selected from one of the four branches in Figure 6.8 as a strating guess for the fit. Equations (4.54) and (4.55) are fitted to the data sets of both detector pairs and all measured muon spin angles simultaneously. The fit parameters are constrained with conditions (i) and (ii) to stay consistent with the powder results. Different initial magnetic configurations from each branch are tested to check the stability of the fit. The final fit results are shown as 95% confidence ellipses in Figure 6.8 and solid lines in Figure 6.5. Stable results are found in three out of the four branches for each magnetic configuration. The resulting magnetic moment for each fit result lies in the range 6.94–7 μ_B which matches the free ion moment of Gd^{3+}. The fitted values of ψ_{Gd} in the branches that include $\psi_{Gd} = \pm 45^\circ$ are found in the range $|\psi_{Gd}| = 45^\circ \pm 1^\circ$ for both magnetic configurations. This result suggests that the magnetic moments in the RE = Gd unit cell have equal magnitudes.

6.5 Temperature dependence

Temperature dependence of the RE magnetic moment is shown in Figure 6.9. Due to the weakness of the RE = Nd magnetic reflections, which results in a low fit quality, a more accurate temperature evolution of its magnetic moment is obtained by taking the integrated intensity of the $(-1\ 1-k\ 4)$ reflection [Figure 6.2(a), inset]. This reflection is chosen as it is strong and does not overlap with any nearby reflections. The magnetic moment is obtained by normalizing the integrated intensity at $T = 1.5\,\mathrm{K}$ to the magnetic moment obtained from Rietveld refinement of the full difference pattern.

Bounds on the magnetic moment of RE = Nd, which is obtained from μSR measurements, are calculated as the maximum and minimum values of the magnetic moment obtained in the θ_{Nd} scan assuming the $\mathrm{F_xF_z}$ magnetic configuration [Figure 6.7(a)]. Magnetic moments corresponding to $\theta_{\mathrm{Nd}} = 115^\circ$, as found from NPD (Table 6.1), are shown as symbols in Figure 6.9(a) and closely follow the values obtained from NPD. The agreement between the two methods validates the muon site and dipole field assumptions when calculating the magnetic moment from μSR.

Temperature dependece of the RE = Gd magnetic moment, as obtained from μSR, shows a non-zero slope as $T \to 0$, suggesting a 2D behavior. It is analyzed using a Schwinger boson mean field theory calculation (Sec. 3.7) based on the Hamiltonian of a layered AFM [44, 67, 68] (Appendix E)

$$H = J\left(\sum_{i,\delta_\parallel} \vec{S}_i \cdot \vec{S}_{i+\delta_\parallel} + \alpha \sum_{i,\delta_\perp} \vec{S}_i \cdot \vec{S}_{i+\delta_\perp}\right). \tag{6.3}$$

The magnetic moment is calculated by simultaneously solving equations (E.7) and (E.11) for h and Δ. The fit parameters and their best values are: $\alpha = 10^{-8.7\pm0.7}$, $m_0 = 6.9 \pm 0.3\,\mu_\mathrm{B}/\mathrm{Gd}$ and $T_\mathrm{N} = 29\,\mathrm{K}$. The exchange interaction strength is $J = 2.38 \pm 0.03\,\mathrm{meV}$. The best fit is presented in Figure 6.9(a) by the dark yellow solid line. The fit function is weakly sensitive to α and only its order of magnitude can be determined. Two additional calculations for $\alpha = 10^{-3}$ and 10^{-5} are added to demonstrate that as anisotropy decreases, $m(T)$ becomes T independent at low temperature, in contrast to the data. The smallness of α supports the 2D nature of the RE = Gd magnet.

The instantaneous magnetic moments as determined by NPD for compounds with RE = Tb, Ho, and Er are shown in Figure 6.9(b). In RE = Tb, two propagation vectors are required to fit the data well. The magnetic moment associated with each component is stable against increasing temperature suggesting a 3D behavior. Close to the first T_N, the strength of these different component switches accompanied with a rotation of the magnetic moments of the $\vec{k}_2$ structure from the $\mathrm{F_xC_z}$ configuration to the $\mathrm{C_xC_z}$ configuration (Figure 6.10). RE = Er resembles anisotropic behavior as in Figure 6.9(a), while the relatively high BT for RE = Ho does not allow clear determination of the $T \to 0$ behavior.

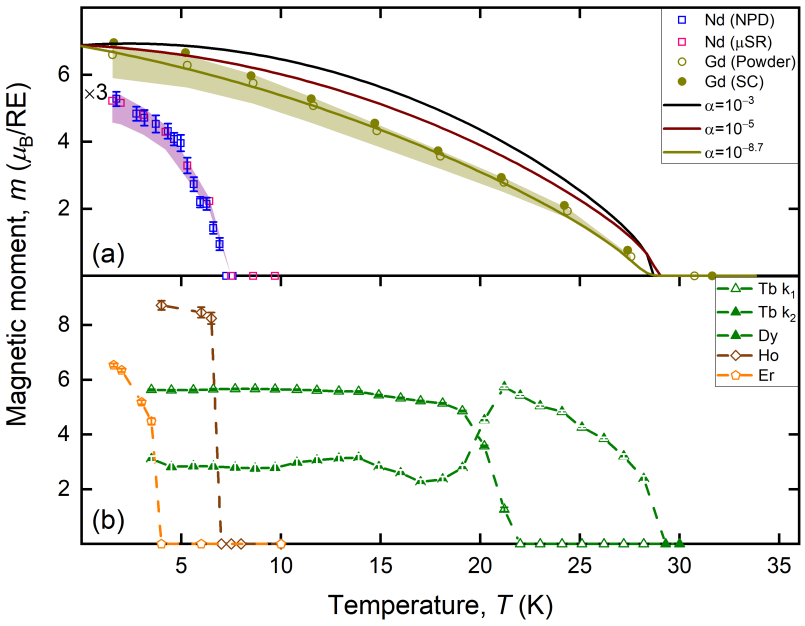

Figure 6.9: Temperature evolution of the magnetic moment for $\left(Mo_{2/3}RE_{1/3}\right)_2 AlC$ with (a) RE = Nd and RE = Gd and (b) RE = Tb, Ho and Er. Pink squares in (a) are obtained from μSR by taking $\theta_{Nd} = 115^\circ$ from the NPD measurements. Circles in (a) are calculated for $\theta_{Gd} = 120^\circ$, while full circles are obtained from single crystal measurements. The data for RE = Nd in (a) is multiplied by 3 for clarity. Solid lines show the calculated magnetic moment for RE = Gd for $\alpha = 10^{-3}$ (black line), $\alpha = 10^{-5}$ (dark red) and $\alpha = 10^{-8.7}$ (dark yellow, see text). Systematic uncertainties in the magnetic moments obtained from μSR measurements are shown as shaded areas.

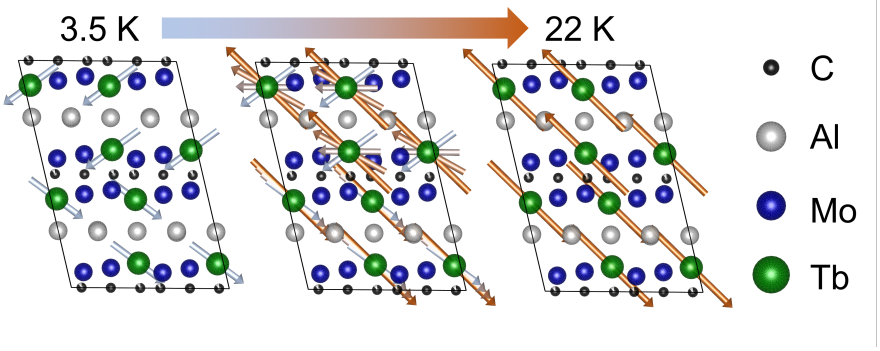

Figure 6.10: Depiction of the transition of the $\left(Mo_{2/3}Tb_{1/3}\right)_2 AlC$ k_2 structure from the C_xF_z structure at 3.5 K to the C_xC_z structure at 22 K. The color of the arrows represents different temperatures.

Temperature dependence of the relaxation rate of the μSR asymmetry is obtained by fitting the temperature dependent data to Equations (4.47) and (4.56) for powder and single crystal data, repsectively and shown in Figure 6.11. The muon relaxation rates in RE = Nd and Gd in Figure 6.11(a) show classical spin lattice relaxation peak at, or close to, T_N where the spin fluctuations are slow enough and their amplitude is large enough to effectively relax the muon polarization. For heavier REs, however, the situation is drastically different [Figure 6.11(b)]. The relaxation rate in RE = Tb is nearly 5 times larger than in RE = Gd and shows a monotonic increase with decreasing temperature. Similar trends can be observed in the remaining compounds as well.

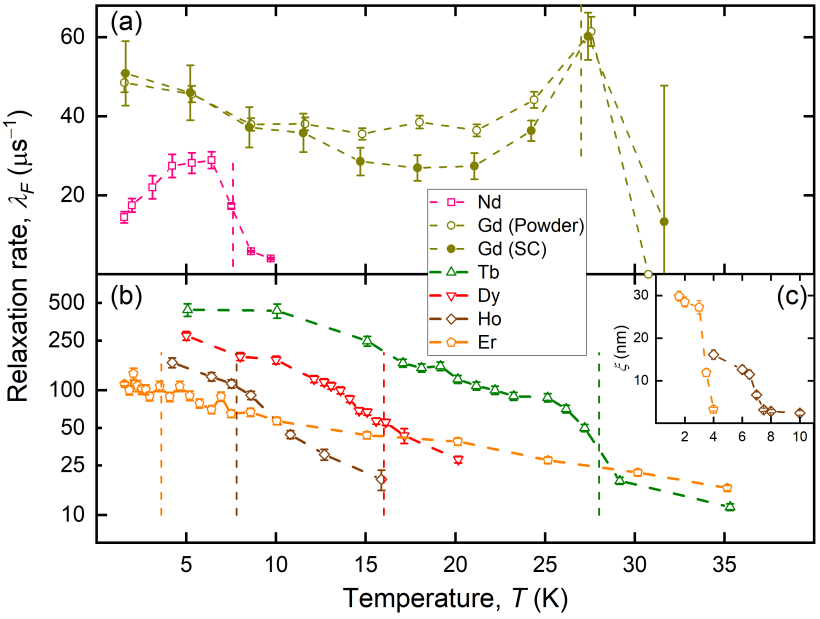

Figure 6.11: Temperature evolution of the muon relaxation rate for (a) RE = Nd and RE = Gd and (b) RE = Tb, Dy, Ho and Er. Dashed vertical lines show T_N for each compound. (c) Temperature evolution of the magnetic correlation length of RE = Ho and Er as determined by NPD measurements.

6.6 Discussion

The possible magnetic structures of RE = Gd [Figure 6.6(c), (d)] are found by combining the NPD and μSR techniques. This is made possible due to the availability of isostructural compounds with different RE atoms, as well as the similarity in magnetic structures for different RE's and the relatively simple magnetic structure found for RE = Gd. While μSR can be used to refine subtle details in magnetic structures [69, 70], which cannot be easily determined from neutron measurements alone, the technique requires at least a rough magnetic

structure to be known a priori. In this work, we have demonstrated an application of μSR which can predict a magnetic structure of a compound without any preliminary knowledge on the same compound.

Temperature evolution of the RE = Gd magnetic moment [Figure 6.9(a)] is well described by an SBMFT calculation up to and including T_N. This agreement indicates that critical fluctuations are either weak or occur in a very small temperature range around T_N as SBMFT does not hold for strong fluctuations [67]. The obtained value for α is smaller than values found for some layered CuO_2 based materials [67] and is close to a calculated value of 2×10^{-8} which was calculated for $Sr_2CuO_2Cl_2$ assuming magnetic dipole interaction between nearest neighbor layers [67]. This can indicate that interactions between planes in RE = Gd are also of dipole origin.

When some magnetic properties are plotted against the RE atom size (Figure 6.12), and show similar trends can be observed. $T_N/\langle T_N \rangle$, $\lambda_F/\langle \lambda_F \rangle$ and m/m_{ion}, measured at 1.5 K, where $\langle\rangle$ indicates average over RE and m_{ion} stands for the free ion moment, show a maximum for RE = Tb and follow an arc. The similarity in the RE dependence of m/m_{ion} and $T_N/\langle T_N \rangle$ suggests that the reduction in the observed magnetic moment is due to temperature and that 1.5 K is not low enough to obtain the free ion moment for RE with $T_N < 10$ K.

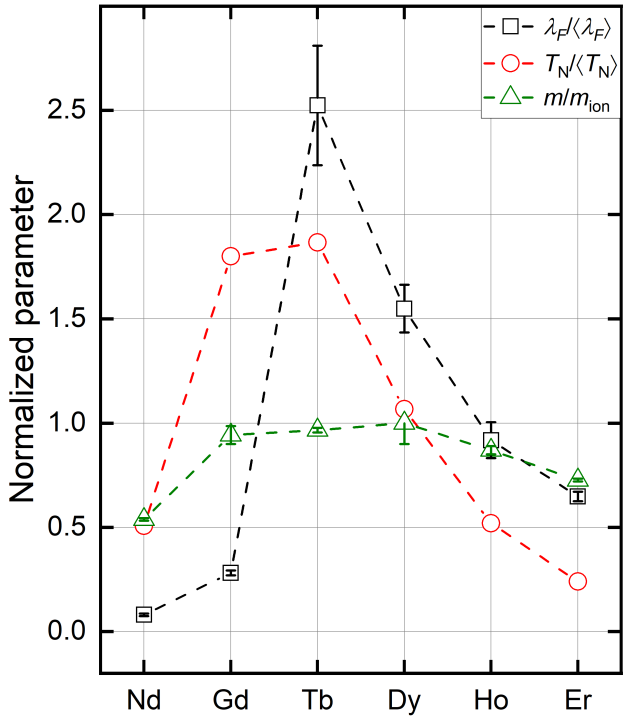

Figure 6.12: Dependence of μSR relaxation rate λ_F, Néel temperature T_N, and magnetic moment m measured at BT, on the RE element in $\left(Mo_{2/3}RE_{1/3}\right)_2 AlC$. For comparison, λ_F, and T_N are normalized relative to their average over RE, while m is normalized relative the free ion moment m_{ion}.

While the muon relaxation observed for RE = Tb, Ho and Er may seem contradictory with NPD results at first, the observation of short-range ordering in RE = Ho and Er via broadening of the magnetic reflections [Figure 6.1, inset] is evidence for a different nature in the magnetic ordering of the heavier lanthanides. The temperature dependence of the magnetic correlation length [Figure 6.11(c)] is similar to λ_F and shows that the slowing down of the magnetic fluctuations is accompanied with a gradual increase in the size of ordered magnetic domains.

The nearly one to one correspondence between λ_F and T_N for REs heavier than Gd also indicates that the relaxation of the μSR signal in these compounds occurs due to a gradual freezing of the dynamic magnetic structure. As T_N is lowered with increasing RE mass beyond Gd, the magnetic structure slows down less at 1.5 K resulting in shorter relaxation rates. The RE dependence of T_N, however, does not follow the well-known [71] de Gennes factor given by

$(g-1)^2 J(J+1)$, where g is the Landé g-factor and J is the total angular momentum of the RE ion, which has its maximum for RE = Gd. This suggests that the magnetic interactions in the $\left(Mo_{2/3}RE_{1/3}\right)_2 AlC$ phases are not described by RKKY interactions alone, but contain additional contributions, such as dipolar interactions between neighboring planes as mentioned for RE = Gd, which are also responsible for the emergence of spin fluctuations and short-range order in the heavy REs.

7 Conclusions

7.1 $(Fe_{1-x}Mn_x)_2AlB_2$ phases

The magnetic phase diagram of the quaternary boride, $(Fe_{1-x}Mn_x)_2AlB_2$, was studied using X-ray and neutron powder diffraction, and magnetization measurements. In agreement with mean field theory predictions, this system offers three magnetic ground states at different Mn concentrations: ferromagnetic (FM), anti-ferromagnetic (AFM), and a canted AFM [Figure 5.8(b)]. This comes about from the competing FM interactions between Fe atoms along the a axis and AFM interactions between Mn atoms along the b axis.

While the addition of Mn decreases the critical temperature [Figure 5.8(b)], FM moment (Figure 5.9), and magnetic entropy change [Figure 5.7(b)], it does increase the relative cooling power for Mn additions up to $x \approx 0.2$ (Table 5.2). This comes about due to the broadening of the temperature range, over which the magnetocaloric effect is significant. It is therefore possible to fine tune the transition temperature of Fe_2AlB_2 in the 274-294 K (0–20 ℃) range without a considerable loss of cooling power.

7.2 $(Mo_{2/3}RE_{1/3})_2AlC$ phases

A series of $(Mo_{2/3}RE_{1/3})_2AlC$ powders were studied using μSR and NPD, with complementary μSR measurements on single crystals of $(Mo_{2/3}Gd_{1/3})_2AlC$ performed as well. From NPD, the magnetic ground states for RE = Nd, Tb, Ho and Er (Figure 6.3) are identified to be transverse SDWs with a number of similar properties. The propagation vectors of the magnetic structure of each compound point along the crystal b axis, and the magnetic moments are aligned in the a-c plane. The magnetic moment size and critical temperature show a peak-like behavior when plotted agains the RE ion (Figure 6.12) with the highest values obtained for RE = Tb.

When the same compounds (including RE = Gd and Dy) are studied with μSR, a striking difference between the behavior of RE = Nd and Gd and RE = Tb, Dy, Ho and Er is observed (Figure 6.4). The muon asymmetry in RE = Nd and Gd shows oscillations, which indicate static magnetic moments on a scale of a few µs. For the heavier REs, however, only a relaxation of the μSR asymmetry is observed which hints at a dynamic behavior of the magnetic structures in these compounds.

The RE = Gd compound is identified as the most promising parent material for 2D MXenes as it has a static magnetic structure, a high magnetic moment of $\approx 7\,\mu_B$ and the highest T_N among the RE-i-MAX phases. Temperature evolution of the Gd magnetic moments is consistent with a nearly 2D AFM, having an anisotropy ratio of $10^{-8.7}$ between out-of-plane and in-plane interactions. This suggests that the magnetic structure can remain stable when exfoliated to a single MXene layer.

However, since Gd is a strong neutron absorber, performing neutron diffraction on this compound is not straightforward. Using the common properties of

the magnetic structures of other $\left(Mo_{2/3}RE_{1/3}\right)_2 AlC$ phases, as well as muon site calculations, significant constraints on the possible magnetic structures of RE = Gd can be placed [Figure 6.6(c), (d)]. Additional measurements on single crystals of RE = Gd are consistent with results obtained on powders, and put even further constraints on the direction and magnitude of the magnetic moments, condirming the validity of our approach.

A Thermodynamic identities

The adiabatic entropy change $\Delta\mathcal{S}_m$ under an application of a field h is directly given by

$$\Delta\mathcal{S}_m(T,h) = \mathcal{S}_{\text{tot}}(T,h) - \mathcal{S}_{\text{tot}}(T,0) = \int_0^h \left(\frac{\partial\mathcal{S}}{dh'}\right)_T dh'. \tag{A.1}$$

To express the integrand in terms of the magnetization we examine the Gibbs free energy

$$\mathcal{G} = E - T\mathcal{S} - Mh. \tag{A.2}$$

Taking the energy differential gives

$$d\mathcal{G} = dE - Td\mathcal{S} - \mathcal{S}dT - hdM - Mdh. \tag{A.3}$$

The change in energy dE is given by the heat flowing into the system $dQ = Td\mathcal{S}$ and the work done by the external field $w = hdM$. Inserting these terms into (A.3) gives

$$d\mathcal{G} = -\mathcal{S}dT - Mdh. \tag{A.4}$$

From (A.4), we can express the entropy and magnetization as

$$\mathcal{S} = -\left(\frac{\partial\mathcal{G}}{\partial T}\right)_h \qquad M = -\left(\frac{\partial\mathcal{G}}{\partial h}\right)_T. \tag{A.5}$$

Finally, using the symmetry of second derivatives together with (A.5), we can express the integrand in (A.1) as

$$\left(\frac{\partial\mathcal{S}}{\partial h}\right)_T = -\left(\frac{\partial}{\partial h}\right)_T\left(\frac{\partial\mathcal{G}}{\partial T}\right)_h = -\left(\frac{\partial}{\partial T}\right)_h\left(\frac{\partial\mathcal{G}}{\partial h}\right)_T = \left(\frac{\partial M}{\partial T}\right)_h. \tag{A.6}$$

Thus we have obtained (3.26). To obtain ΔT_{ad} we express the entropy $\mathcal{S}(T,h)$ and take its differential

$$d\mathcal{S} = \left(\frac{\partial\mathcal{S}}{\partial T}\right)_h dT + \left(\frac{\partial\mathcal{S}}{\partial h}\right)_T dh. \tag{A.7}$$

For an adiabatic field change, we have $d\mathcal{S} = 0$ and therefore

$$dT = -\left(\frac{\partial\mathcal{S}}{\partial T}\right)_h^{-1}\left(\frac{\partial\mathcal{S}}{\partial h}\right)_T dh. \tag{A.8}$$

Using the definition of specific heat

$$C(T,h) = T\left(\frac{\partial\mathcal{S}}{\partial T}\right)_h \tag{A.9}$$

and inserting (A.9) and (A.6) into (A.8) we find

$$dT = -\frac{T}{C(T,h)}\left(\frac{\partial M}{\partial T}\right)_h dh. \tag{A.10}$$

Integrating (A.10) gives (3.27).

B Representational analysis of the magnetic structures of M_2AlB_2 compounds

The M_2AlB_2 compounds crystallize in the $Cmmm$ space group, which has an orthorhombic base centered unit cell. The basis vectors of the primitive and reciprocal unit cells [Figure B.1(a), (b)] are given by

$$\begin{array}{ll} \vec{a}_1 = \begin{pmatrix} a & 0 & 0 \end{pmatrix}^T & \vec{a}_1^* = 2\pi \begin{pmatrix} \frac{1}{a} & -\frac{1}{b} & 0 \end{pmatrix}^T \\ \vec{a}_2 = \begin{pmatrix} \frac{a}{2} & \frac{b}{2} & 0 \end{pmatrix}^T & \vec{a}_2^* = 4\pi \begin{pmatrix} 0 & \frac{1}{b} & 0 \end{pmatrix}^T \\ \vec{a}_3 = \begin{pmatrix} 0 & 0 & c \end{pmatrix}^T & \vec{a}_3^* = 2\pi \begin{pmatrix} 0 & 0 & \frac{1}{c} \end{pmatrix}^T \end{array} . \tag{B.1}$$

The magnetic structures observed in Fe_2AlB_2 and Mn_2AlB_2 have propagation

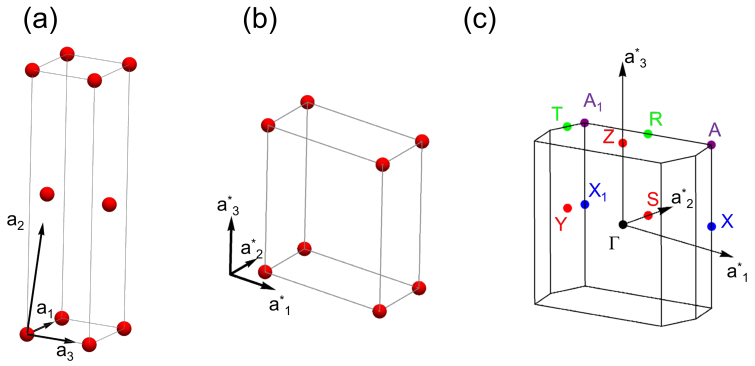

Figure B.1: (a) The conventional direct $Cmmm$ unit cell and the primitive lattice vectors. (b) The reciprocal unit cell of $Cmmm$ with the reciprocal lattice vectors. (c) The Brillouin zone of $Cmmm$ with its high symmetry points.

vectors $\vec{k}_{\text{Fe}} = \begin{pmatrix} 0 & 0 & 0 \end{pmatrix}^T$ and $\vec{k}_{\text{Mn}} = \begin{pmatrix} 0 & 0 & \frac{1}{2} \end{pmatrix}^T$, respectively. These vectors correspond to the Γ and Z points in the Brillouin zone of $Cmmm$ [Figure B.1(c)], respectively. By inspection, the propagation vector group (3.11) of both the Γ and Z points is mmm (D2h). This group has 8 symmetry elements, namely: The identity 1, three two-fold rotations 2_x, 2_y, 2_z, inversion $\bar{1}$ and three mirror planes m_{xy}, m_{xz}, m_{yz}. The magnetic atoms in M_2AlB_2 occupy the $4j$ site (Figure B.2), which has four inequivalent atoms. From Bloch's theorem (3.3), the ground state magnetic configurations have the following form:

$$\Psi_{\vec{k}}(\vec{r}) = \begin{pmatrix} \vec{\mu}_1 \\ \vec{\mu}_2 \\ \vec{\mu}_3 \\ \vec{\mu}_4 \end{pmatrix} e^{-i\vec{k}\cdot\vec{r}}, \tag{B.2}$$

where $\vec{\mu}_i$ is the magnetic moment on atom i in the $4j$ site. Performing a symmetry operation on $\Psi_{\vec{k}}$ exchanges the position of the atoms, as well as rotates the

magnetic moment of each atom. The representation Γ_{mag} of these symmetry operations is therefore given by

$$\Gamma_{\text{mag}} = \Gamma_{\text{perm}} \otimes \Gamma_{\text{axial}}, \tag{B.3}$$

where Γ_{perm} is the permutation representation and Γ_{axial} is the axial vector representation. We note however, that atoms 3 and 4 are related to atoms 1 and 2 by the base centering translation $\vec{t}_C = \begin{pmatrix} \frac{a}{2} & \frac{b}{2} & 0 \end{pmatrix}^T$. Therefore, we obtain the symmetry constraint

$$\vec{\mu}_{3,4} = \vec{\mu}_{1,2} e^{-i\vec{k}\cdot\vec{t}_C}. \tag{B.4}$$

From this constraint, we only need to look at the permutations of atoms 1 and 2, and thus the permutation representation is a two-dimensional representation. The explicit matrices of symmetry elements from mmm in the permutation and axial representations are given in Table B.1. To decompose Γ_{mag} into the

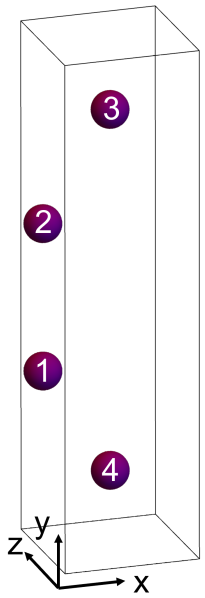

Figure B.2: The positions of magnetic atoms in the $4j$ site of $Cmmm$.

irreducible representations of mmm and obtain the possible magnetic configurations, we need to calculate the character (3.13) of Γ_{mag}. From Table B.1 the characters of Γ_{perm} and Γ_{axial} are

$$\begin{aligned} \chi_{\Gamma_{\text{perm}}} &= \{2, 0, 2, 0, 0, 2, 0, 2\} \\ \chi_{\Gamma_{\text{axial}}} &= \{3, -1, -1, -1, 3, -1, -1, -1\}. \end{aligned} \tag{B.5}$$

Table B.1: The representations of symmetry elements of mmm in the permutation (Γ_{perm}) and axial vector (Γ_{axial}) representation.

Element	Γ_{perm}	Γ_{axial}	Element	Γ_{perm}	Γ_{axial}
1	$\begin{pmatrix} 1 & 0 \\ 0 & 1 \end{pmatrix}$	$\begin{pmatrix} 1 & 0 & 0 \\ 0 & 1 & 0 \\ 0 & 0 & 1 \end{pmatrix}$	$\overline{1}$	$\begin{pmatrix} 0 & 1 \\ 1 & 0 \end{pmatrix}$	$\begin{pmatrix} 1 & 0 & 0 \\ 0 & 1 & 0 \\ 0 & 0 & 1 \end{pmatrix}$
2_x	$\begin{pmatrix} 0 & 1 \\ 1 & 0 \end{pmatrix}$	$\begin{pmatrix} 1 & 0 & 0 \\ 0 & -1 & 0 \\ 0 & 0 & -1 \end{pmatrix}$	m_{xy}	$\begin{pmatrix} 1 & 0 \\ 0 & 1 \end{pmatrix}$	$\begin{pmatrix} -1 & 0 & 0 \\ 0 & -1 & 0 \\ 0 & 0 & 1 \end{pmatrix}$
2_y	$\begin{pmatrix} 1 & 0 \\ 0 & 1 \end{pmatrix}$	$\begin{pmatrix} -1 & 0 & 0 \\ 0 & 1 & 0 \\ 0 & 0 & -1 \end{pmatrix}$	m_{xz}	$\begin{pmatrix} 0 & 1 \\ 1 & 0 \end{pmatrix}$	$\begin{pmatrix} -1 & 0 & 0 \\ 0 & 1 & 0 \\ 0 & 0 & -1 \end{pmatrix}$
2_z	$\begin{pmatrix} 0 & 1 \\ 1 & 0 \end{pmatrix}$	$\begin{pmatrix} -1 & 0 & 0 \\ 0 & -1 & 0 \\ 0 & 0 & 1 \end{pmatrix}$	m_{yz}	$\begin{pmatrix} 1 & 0 \\ 0 & 1 \end{pmatrix}$	$\begin{pmatrix} 1 & 0 & 0 \\ 0 & -1 & 0 \\ 0 & 0 & -1 \end{pmatrix}$

The character of Γ_{mag} is then given by multiplying the terms of $\chi_{\Gamma_{\mathrm{perm}}}$ and $\chi_{\Gamma_{\mathrm{axial}}}$ and therefore

$$\chi_{\Gamma_{\mathrm{mag}}} = \{6, 0, -2, 0, 0, -2, 0, -2\}\,. \tag{B.6}$$

To decompose this character into representations of mmm we examine the character table of mmm (Table B.2). Using the direct product of characters (3.14)

Table B.2: The character table of mmm point group.

	1	2_x	2_y	2_z	$\overline{1}$	m_{xy}	m_{xz}	m_{yz}
$\mathrm{A_g}$	1	1	1	1	1	1	1	1
$\mathrm{B_{1g}}$	1	−1	−1	1	1	1	−1	−1
$\mathrm{B_{2g}}$	1	−1	1	−1	1	−1	1	−1
$\mathrm{B_{3g}}$	1	1	−1	−1	1	−1	−1	1
$\mathrm{A_u}$	1	1	1	1	−1	−1	−1	−1
$\mathrm{B_{1u}}$	1	−1	−1	1	−1	−1	1	1
$\mathrm{B_{2u}}$	1	−1	1	−1	−1	1	−1	1
$\mathrm{B_{3u}}$	1	1	−1	−1	−1	1	1	−1

we find the following decomposition:

$$\Gamma_{\mathrm{mag}} = \mathrm{B_{1g}} \oplus \mathrm{B_{2g}} \oplus \mathrm{B_{3g}} \oplus \mathrm{A_u} \oplus \mathrm{B_{1u}} \oplus \mathrm{B_{3u}}. \tag{B.7}$$

The possible magnetic ground states are then obtained using projection operators (3.16) onto each irreducible representation and are given in Table B.3.

Table B.3: Projected basis vectors for each irreducible representation of the magnetic representation for M_2AlB_2.

Representation	B_{1g}	B_{2g}	B_{3g}	A_u	B_{1u}	B_{3u}
Basis vector	$\begin{pmatrix}0\\0\\1\\0\\0\\1\end{pmatrix}$	$\begin{pmatrix}0\\1\\0\\0\\1\\0\end{pmatrix}$	$\begin{pmatrix}1\\0\\0\\1\\0\\0\end{pmatrix}$	$\begin{pmatrix}0\\1\\0\\0\\-1\\0\end{pmatrix}$	$\begin{pmatrix}1\\0\\0\\-1\\0\\0\end{pmatrix}$	$\begin{pmatrix}0\\0\\1\\0\\0\\-1\end{pmatrix}$

C Mean field calculation of $(Fe_{1-x}Mn_x)_2AlB_2$

To build a MFT model of $(Fe_{1-x}Mn_x)_2AlB_2$ we first note that the four magnetic atoms in the unit cell [Figure C.1(a)-(c)] are equal in magnitude by symmetry restrictions (Table B.3). We thus average them into a single supermoment so that we do not need to include multiple sites in the unit cell. Next, we note that in case multiple coordination shells are included in the interaction term, the MFT results will not depend individually on the exchange coefficient of each coordination shell, but rather on the sum of all coordination shells [Eq. (3.21)]. We therefore take the magnitude of the exchange interactions in all directions to be equal and focus only on the first coordination shell.

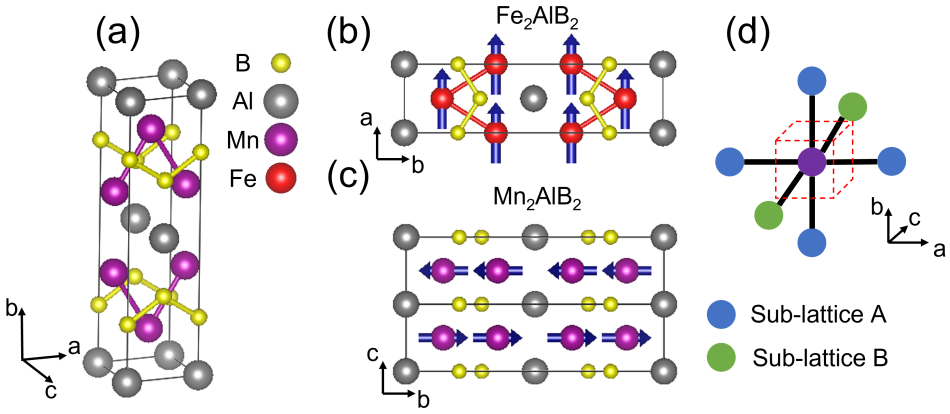

Figure C.1: (a) The chemical unit cell of M_2AlB_2, (b) FM structure of Fe_2AlB_2, (c) AFM structure of Mn_2AlB_2, and (d) sublattice structure of simplified mean-field model of M_2AlB_2.

Since the ground state of Mn_2AlB_2 has a propagation vector $\begin{pmatrix}0 & 0 & \frac{1}{2}\end{pmatrix}^T$,

it splits the magnetic moments into two sublattices along the c axis [Figure C.1(c)]. Our simplified lattice is then a simple cubic lattice, with atoms along the c axis split into two sublattices [Figure C.1(d)] labeled A and B. Next, we need to take into account the fact that there are two possible types of atoms, Fe and Mn. With these considerations in mind, our spin operators are labeled with $X = \mathrm{Fe}, \mathrm{Mn}$ and $\delta = \mathrm{A}, \mathrm{B}$. In the zeroth approximation of MFT [72], we treat one central atom of each kind and on each sublattice exactly, while taking the average spin on all other atoms. With these new considerations in mind, equations (3.19)–(3.22) become

$$\vec{M}_{X,\delta} = -\mu_{\mathrm{B}} \overleftrightarrow{g_X} \left\langle \vec{S}_{X,\delta} \right\rangle, \tag{C.1}$$

$$H^{\mathrm{MF}}_{X,\delta} = \mu_{\mathrm{B}} \vec{S}_{X,\delta} \overleftrightarrow{g_X} \vec{B}^{\mathrm{eff}}_{X,\delta}, \tag{C.2}$$

$$\vec{B}^{\mathrm{eff}}_{X,\delta} = \vec{B} + \sum_{\substack{X' = \mathrm{Fe},\mathrm{Mn} \\ \delta' = \mathrm{A},\mathrm{B}}} p_{X'} \overleftrightarrow{\Lambda}^{\delta,\delta'}_{X,X'} \vec{M}_{X',\delta'}, \tag{C.3}$$

$$\overleftrightarrow{\Lambda}^{\delta,\delta'}_{X,X'} = (\mu_{\mathrm{B}} \overleftrightarrow{g_X})^{-1} \left(z^{\delta,\delta'} \overleftrightarrow{J}^{\delta,\delta'}_{X,X'} \right) (\mu_{\mathrm{B}} \overleftrightarrow{g_X})^{-1}$$

and

$$\vec{M}_{X,\delta} = \mu_{\mathrm{B}} \overleftrightarrow{g_X} S_X \mathrm{B}_S \left(\beta \mu_{\mathrm{B}} S_X \left| \overleftrightarrow{g_X} \vec{B}^{\mathrm{eff}}_{X,\delta} \right| \right) \frac{\overleftrightarrow{g_X} \vec{B}^{\mathrm{eff}}_{X,\delta}}{\left| \overleftrightarrow{g_X} \vec{B}^{\mathrm{eff}}_{X,\delta} \right|}. \tag{C.4}$$

In equations (C.1)–(C.4) we have defined $\overleftrightarrow{g_X}$ the g-factor of atom X, p_X the concentration of atom X, S_X the spin of atom X, $z^{\delta,\delta'}$ the number of nearest neighbors of an atom on sublattice δ, which belong to sublattice δ' and $\overleftrightarrow{J}^{\delta,\delta'}_{X,X'}$ the exchange integral between atom X on sublattice δ and atom X' on sublattice δ'. The total on-site magnetization is calculated by

$$\vec{M}_{\delta} = \sum_{X} p_X \vec{M}_{X,\delta}. \tag{C.5}$$

The values for each parameter in our model were obtained by fitting (C.5) to the ordered magnetic moment obtained by neutron diffraction and are given in Table C.1.

Table C.1: The value for the parameters required in the mean-field calculation of $(Fe_{1-x}Mn_x)_2AlB_2$. For matrix parameters g and J, only the non-zero elements are given. Values in parentheses indicate the statistical 1σ uncertainties of the fit.

Parameter	Value
$g_{\mathrm{Fe}}^{xx} = g_{\mathrm{Fe}}^{yy}$	0.86 (2)
$g_{\mathrm{Mn}}^{xx} = g_{\mathrm{Mn}}^{yy}$	1.38(1)
p_{Fe}	$1-x$
p_{Mn}	x
S_{Fe}	3/2
S_{Mn}	1/2
$z^{\mathrm{A,A}} = z^{\mathrm{B,B}}$	4
$z^{\mathrm{A,B}} = z^{\mathrm{B,A}}$	2
$\left(J_{\mathrm{Fe,Fe}}^{\mathrm{A,A}}\right)^{xx} = \left(J_{\mathrm{Fe,Fe}}^{\mathrm{A,B}}\right)^{xx}$	3.67 (8) meV
$\left(J_{\mathrm{Fe,Mn}}^{\mathrm{A,A}}\right)^{xx} = \left(J_{\mathrm{Fe,Mn}}^{\mathrm{A,B}}\right)^{xx}$	2.3 (5) meV
$\left(J_{\mathrm{Fe,Mn}}^{\mathrm{A,A}}\right)^{yy} = -\left(J_{\mathrm{Fe,Mn}}^{\mathrm{A,B}}\right)^{yy}$	11.7 (4) meV
$\left(J_{\mathrm{Mn,Mn}}^{\mathrm{A,A}}\right)^{yy} = -\left(J_{\mathrm{Mn,Mn}}^{\mathrm{A,B}}\right)^{yy}$	18.9 (2) meV

D Representation analysis of the magnetic structures of RE-*i*-MAX

$\left(Mo_{2/3}RE_{1/3}\right)_2 AlC$ compounds crystallize in the $C2/c$ space group with the RE atoms occupying the $8j$ position. The direct and reciprocal cells and their axes [Figure D.1(a) and (b)] are given by

$$\begin{aligned} \vec{a}_1 &= \begin{pmatrix} \frac{a}{2} & \frac{b}{2} & 0 \end{pmatrix}^T & \vec{a}_1^* &= 4\pi \begin{pmatrix} \frac{1}{a} & 0 & -\frac{1}{a\tan\beta} \end{pmatrix}^T \\ \vec{a}_2 &= \begin{pmatrix} 0 & b & 0 \end{pmatrix}^T & \vec{a}_2^* &= 2\pi \begin{pmatrix} -\frac{1}{a} & \frac{1}{b} & \frac{1}{a\tan\beta} \end{pmatrix}^T \\ \vec{a}_3 &= \begin{pmatrix} c\cos\beta & 0 & c\sin\beta \end{pmatrix}^T & \vec{a}_3^* &= 2\pi \begin{pmatrix} 0 & 0 & \frac{1}{c\sin\beta} \end{pmatrix}^T \end{aligned} . \tag{D.1}$$

All observed magnetic structures of $\left(Mo_{2/3}RE_{1/3}\right)_2 AlC$ have propagation vectors $\vec{k} = (0,k,0)^T$, which do not pass through any special points in the Brillouine zone [Figure D.1(c)]. Since $\vec{k}$ is not equivalent to $-\vec{k}$ for $k \neq 0$, the propagation vector group of $\vec{k}$ is 2 (C_2) and contains two elements: The identity 1 and a two-fold rotation 2_y. There are 8 magnetic atoms in the unit cells, however atoms 5–8 are related to atoms 1–4 by the translation $\vec{t}_C = (0.5, 0.5, 0)$ and therefore have a relative phase of $2\pi\vec{k}\cdot\vec{t}_C = \pi k$. The permutation and axial vector representations of the propagation vector group are therefore considered only for the first 4 atoms and are given in Table D.1.

We note that the Γ_{perm} representation is block diagonal and composed of two 2×2 matrices. This means that atoms 1, 2 and atoms 3, 4 transform

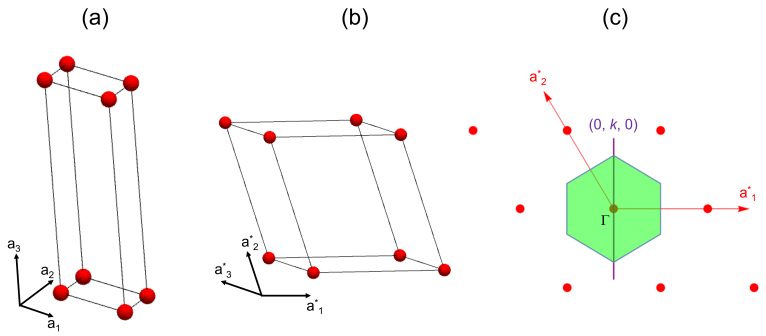

Figure D.1: (a) The primitive direct $C2/c$ unit cell and the primitive lattice vectors. (b) The reciprocal unit cell of $C2/c$ with the reciprocal lattice vectors. (c) Projection of the Brillouin zone of $C2/c$ in the a_1^*-a_2^* plane.

Table D.1: The representations of symmetry elements of 2 in the permutation (Γ_{perm}) and axial vector (Γ_{axial}) representation.

Element	Γ_{perm}	Γ_{axial}
1	$\begin{pmatrix} 1 & 0 & 0 & 0 \\ 0 & 1 & 0 & 0 \\ 0 & 0 & 1 & 0 \\ 0 & 0 & 0 & 1 \end{pmatrix}$	$\begin{pmatrix} 1 & 0 & 0 \\ 0 & 1 & 0 \\ 0 & 0 & 1 \end{pmatrix}$
2_y	$\begin{pmatrix} 0 & 1 & 0 & 0 \\ 1 & 0 & 0 & 0 \\ 0 & 0 & 0 & 1 \\ 0 & 0 & 1 & 0 \end{pmatrix}$	$\begin{pmatrix} -1 & 0 & 0 \\ 0 & 1 & 0 \\ 0 & 0 & -1 \end{pmatrix}$

independently under the symmetry operations of the propagation vector group and therefore split into two orbits. We threfore have to obtain the magnetic representation for a single orbit, as both orbits are identical. We denote the permutation representation of a single orbit as Γ_{orb} which contains the matrices $1 = \begin{pmatrix} 1 & 0 \\ 0 & 1 \end{pmatrix}$ and $2_y = \begin{pmatrix} 0 & 1 \\ 1 & 0 \end{pmatrix}$. The required characters are therefore

$$\begin{aligned} \chi_{\Gamma_{\text{orb}}} &= \{2, 0\} \\ \chi_{\Gamma_{\text{axial}}} &= \{3, -1\} \end{aligned} \tag{D.2}$$

and the character of the magnetic representation of a single orbit $\Gamma_{\text{mag, orb}} = \Gamma_{\text{orb}} \otimes \Gamma_{\text{axial}}$ is

$$\chi_{\Gamma_{\text{mag, orb}}} = \{6, 0\}\,. \tag{D.3}$$

To decompose $\chi_{\Gamma_{\text{mag}}}$ into the irreducible representations we use the character table of point group 2 (Table D.2). The resulting decomposition of the magnetic

representation into the irreducible representations is

$$\Gamma_{\text{mag, orb}} \sim 3\text{A} \oplus 3\text{B}.$$

Table D.2: The character table of point group 2.

	1	2_y
A	1	1
B	1	-1

In the main text, we define $\Gamma_1 = \text{A}$ and $\Gamma_2 = \text{B}$ for convenience. Since each representation appears 3 times in $\Gamma_{\text{mag, orb}}$, there are 3 basis vectors associated with each representation and they are given in Table D.3. Finally, the full magnetic representation is obtained by combining both orbits which gives

$$\Gamma_{\text{mag}} \sim \Gamma_{\text{mag, orb}} \oplus \Gamma_{\text{mag, orb}} \sim (3\Gamma_1 \oplus 3\Gamma_2) \oplus (3\Gamma_1 \oplus 3\Gamma_2) \sim 6\Gamma_1 \oplus 6\Gamma_2. \quad \text{(D.4)}$$

The basis vectors of Γ_{mag} are obtained by combining the basis vectors of a single orbit for atoms 1,2 and 3,4. The final basis vector set is given in Table D.4 and they are labeled using Bertaut notation [64].

Table D.3: Projected basis vectors for each irreducible representation of the magnetic representation for $\left(\text{Mo}_{2/3}\text{RE}_{1/3}\right)_2\text{AlC}$.

Representation	Γ_1			Γ_2		
Basis vector	V_1	V_2	V_3	V_1	V_2	V_3
Basis vector	$\begin{pmatrix} 1 \\ 0 \\ 0 \\ -1 \\ 0 \\ 0 \end{pmatrix}$	$\begin{pmatrix} 0 \\ 1 \\ 0 \\ 0 \\ 1 \\ 0 \end{pmatrix}$	$\begin{pmatrix} 0 \\ 0 \\ 1 \\ 0 \\ 0 \\ -1 \end{pmatrix}$	$\begin{pmatrix} 1 \\ 0 \\ 0 \\ 1 \\ 0 \\ 0 \end{pmatrix}$	$\begin{pmatrix} 0 \\ 1 \\ 0 \\ 0 \\ -1 \\ 0 \end{pmatrix}$	$\begin{pmatrix} 0 \\ 0 \\ 1 \\ 0 \\ 0 \\ 1 \end{pmatrix}$

Table D.4: Basis vectors of the full magnetic representation for $\vec{k} = (0, k, 0)$ in $\left(Mo_{2/3}RE_{1/3}\right)_2 AlC$ compounds. The basis vectors are labeled using Bertaut notation.

(a) Basis vectors of Γ_{mag} which belong to irreducible representation Γ_1.

Representation	Γ_1					
Basis vector	G_x	F_y	G_x	A_x	C_y	A_x
Basis vector	$\begin{pmatrix} 1 \\ 0 \\ 0 \\ -1 \\ 0 \\ 0 \\ 1 \\ 0 \\ 0 \\ -1 \\ 0 \\ 0 \end{pmatrix}$	$\begin{pmatrix} 0 \\ 1 \\ 0 \\ 0 \\ 1 \\ 0 \\ 0 \\ 1 \\ 0 \\ 0 \\ 1 \\ 0 \end{pmatrix}$	$\begin{pmatrix} 0 \\ 0 \\ 1 \\ 0 \\ 0 \\ -1 \\ 0 \\ 0 \\ 1 \\ 0 \\ 0 \\ -1 \end{pmatrix}$	$\begin{pmatrix} 1 \\ 0 \\ 0 \\ -1 \\ 0 \\ 0 \\ -1 \\ 0 \\ 0 \\ 1 \\ 0 \\ 0 \end{pmatrix}$	$\begin{pmatrix} 0 \\ 1 \\ 0 \\ 0 \\ 1 \\ 0 \\ 0 \\ -1 \\ 0 \\ 0 \\ -1 \\ 0 \end{pmatrix}$	$\begin{pmatrix} 0 \\ 0 \\ 1 \\ 0 \\ 0 \\ -1 \\ 0 \\ 0 \\ -1 \\ 0 \\ 0 \\ 1 \end{pmatrix}$

(b) Basis vectors of Γ_{mag} which belong to irreducible representation Γ_2.

Representation	Γ_2					
Basis vector	F_x	G_y	F_x	C_x	A_y	C_x
Basis vector	$\begin{pmatrix} 1 \\ 0 \\ 0 \\ 1 \\ 0 \\ 0 \\ 1 \\ 0 \\ 0 \\ 1 \\ 0 \\ 0 \end{pmatrix}$	$\begin{pmatrix} 0 \\ 1 \\ 0 \\ 0 \\ -1 \\ 0 \\ 0 \\ 1 \\ 0 \\ 0 \\ -1 \\ 0 \end{pmatrix}$	$\begin{pmatrix} 0 \\ 0 \\ 1 \\ 0 \\ 0 \\ 1 \\ 0 \\ 0 \\ 1 \\ 0 \\ 0 \\ 1 \end{pmatrix}$	$\begin{pmatrix} 1 \\ 0 \\ 0 \\ 1 \\ 0 \\ 0 \\ -1 \\ 0 \\ 0 \\ -1 \\ 0 \\ 0 \end{pmatrix}$	$\begin{pmatrix} 0 \\ 1 \\ 0 \\ 0 \\ -1 \\ 0 \\ 0 \\ -1 \\ 0 \\ 0 \\ 1 \\ 0 \end{pmatrix}$	$\begin{pmatrix} 0 \\ 0 \\ 1 \\ 0 \\ 0 \\ 1 \\ 0 \\ 0 \\ -1 \\ 0 \\ 0 \\ -1 \end{pmatrix}$

E Analysis of the layered antiferromagnet using Schwinger boson mean field theory

We start from the Hamiltonian of a layered antiferromagnet (6.3)

$$H = J\left(\sum_{i,\delta_\parallel} \vec{S}_i \cdot \vec{S}_{i+\delta_\parallel} + \alpha \sum_{i,\delta_\perp} \vec{S}_i \cdot \vec{S}_{i+\delta_\perp}\right). \tag{E.1}$$

The first step is to treat the interlayer interaction using a mean field theory. To make the notation clearer, we separate the general spin index i into an intra-layer position vector $\vec{R}$ and a layer index l. Then, the inter-layer interaction term is given by $\sum_{\vec{R},l} \vec{S}_{\vec{R}.l} \cdot \vec{S}_{\vec{R},l+1}$. To obtain a mean field theory, we write

$$\vec{S}_{\vec{R},l} = \left\langle \vec{S}_{\vec{R},l} \right\rangle + \delta\vec{S}_{\vec{R},l}, \tag{E.2}$$

where $\left\langle \vec{S}_{\vec{R},l} \right\rangle$ is the expectation value of the spin and $\delta\vec{S}_{\vec{R},l}$ is a fluctuation around the mean. Plugging (E.2) into the inter-layer interaction, neglecting the second order fluctuation term and restoring $\vec{S}_{\vec{R},l}$ gives

$$\sum_{\vec{R},l} \vec{S}_{\vec{R}.l} \cdot \vec{S}_{\vec{R},l+1} \approx \sum_{\vec{R},l} \left[\left\langle \vec{S}_{\vec{R},l} \right\rangle^2 + \left(\vec{S}_{\vec{R},l+1} - \vec{S}_{\vec{R},l}\right) \cdot \left\langle \vec{S}_{\vec{R},l} \right\rangle\right], \tag{E.3}$$

where we have used the fact that in the AFM ground state $\left\langle \vec{S}_{\vec{R},l} \right\rangle = (-1)^l e^{2\pi i \vec{q}\cdot\vec{R}} \left\langle \vec{S}_{\vec{R}} \right\rangle$ with $\vec{q} = \left(\frac{1}{2}, \frac{1}{2}\right)$. The first term in (E.3) does not depend on the lattice site and gives a constant energy term. The second term defines an effective mean field via

$$\begin{aligned} &\sum_{\vec{R},l} \left(\vec{S}_{\vec{R},l+1} - \vec{S}_{\vec{R},l}\right) \cdot \left\langle \vec{S}_{\vec{R},l} \right\rangle \\ &= -\sum_{\vec{R},l} \vec{S}_{\vec{R},l+1} \cdot \left\langle \vec{S}_{\vec{R},l+1} \right\rangle - \sum_{\vec{R},l} \vec{S}_{\vec{R},l} \cdot \left\langle \vec{S}_{\vec{R},l} \right\rangle \\ &= -2\sum_{\vec{R},l} \vec{S}_{\vec{R},l} \cdot \left\langle \vec{S}_{\vec{R},l} \right\rangle. \end{aligned} \tag{E.4}$$

Plugging back (E.4) into (E.1) gives

$$H = J\left(\sum_{\vec{R},l,\vec{\delta}_\parallel} \vec{S}_{\vec{R},l} \cdot \vec{S}_{\vec{R}+\vec{\delta}_\parallel,l} - 2\alpha \sum_{\vec{R},l} \vec{S}_{\vec{R},l} \cdot \left\langle \vec{S}_{\vec{R},l} \right\rangle\right). \tag{E.5}$$

We next assume the magnetization is directed out of plane so that only the z component of the effective field remains. The effective Hamiltonian can then be

written as

$$H = J \sum_{\vec{R}} \left(\frac{1}{2} \sum_{\vec{\delta}_{\parallel}} \vec{S}_{\vec{R}} \cdot \vec{S}_{\vec{R}+\vec{\delta}_{\parallel}} - 2\alpha h_{\vec{R}} S^z_{\vec{R}} \right). \tag{E.6}$$

In (E.6), the layers are decoupled using an effective field

$$h_{\vec{R}} = -2\alpha \left\langle S^z_{\vec{R}} \right\rangle. \tag{E.7}$$

In MFT, the average spin is proportional to the magnetization and is site independent. We denote $-\left\langle S^z_{\vec{R}} \right\rangle = M$ and obtain the mean field self-consistency equation

$$h = 2\alpha M. \tag{E.8}$$

We can now use the results from Sec. 3 to calculate M for the 2D antiferromagnet. M is given by (3.59) which requires solving equations (3.55) and (3.56). By treating the spin-wave velocity c as fixed to its result from spin wave theory $2.32J$ [67], we remain with two equations which need to be solved. Those are (E.8), where

$$M = S + \frac{1}{2} - 2\mathbb{F}\left(\Delta, h, t\right) \tag{E.9}$$

and

$$\mathbb{F}\left(\Delta, h, t\right) = 2.32 \int_0^1 \frac{1 + \Delta + h}{\omega\left(\Delta, h, \gamma'\right)} \left[n\left(\omega, t\right) + \frac{1}{2} \right] \varrho\left(\gamma'\right) d\gamma'. \tag{E.10}$$

The dispersion is given by $\omega\left(\Delta, h, \gamma'\right) = 2.32\sqrt{\left(1 + \Delta + h\right)^2 - \gamma'^2}$, $t = T/J$ is the reduced temperature and n and ϱ are defined in equations (3.57) and (3.60), respectively. Finally, we are left with the constraint equation (3.56) which takes the form

$$\mathbb{F}\left(\Delta, h, t\right) + \mathbb{F}\left(\Delta, 0, t\right) = S + \frac{1}{2}. \tag{E.11}$$

References

[1] S. Kota, M. Sokol, and M.W. Barsoum. A progress report on the MAB phases: atomically laminated, ternary transition metal borides. *International Materials Reviews*, 65(4):226–255, 2020.

[2] H.J. Becher, K. Krogmann, and E. Peisker. Über das ternäre Borid Mn_2AlB_2. *Zeitschrift für anorganische und allgemeine Chemie*, 344(3-4):140–147, 1966.

[3] W. Jeitschko. The crystal structure of Fe_2AlB_2. *Acta Crystallographica Section B*, 25:163–165, 1969.

[4] N.F. Chaban and Yu.B. Kuz'ma. TERNAERE SYSTEME CR-AL-B UND MN-AL-B. *Chemischer Informationsdienst*, 5(4), 1974.

[5] M. ElMassalami, D. da S. Oliveira, and H. Takeya. On the ferromagnetism of $AlFe_2B_2$. *Journal of Magnetism and Magnetic Materials*, 323(16):2133–2136, 2011.

[6] X. Tan, P. Chai, C.M. Thompson, and M. Shatruk. Magnetocaloric Effect in $AlFe_2B_2$: Toward Magnetic Refrigerants from Earth-Abundant Elements. *Journal of the American Chemical Society*, 135(25):9553–9557, 2013.

[7] P. Chai, S.A. Stoian, X. Tan, P.A. Dube, and M. Shatruk. Investigation of magnetic properties and electronic structure of layered-structure borides AlT_2B_2 (T = Fe, Mn, Cr) and $AlFe_{2-x}Mn_xB_2$. *Journal of Solid State Chemistry*, 224:52–61, 2015.

[8] Q. Du, G. Chen, W. Yang, J. Wei, M. Hua, H. Du, C. Wang, S. Liu, J. Han, and Y. Zhang. Magnetic frustration and magnetocaloric effect in $AlFe_{2-x}Mn_xB_2$ ($x = 0 - 0.5$) ribbons. *Journal of Physics D: Applied Physics*, 48(33):335001, 2015.

[9] S. Hirt, F. Yuan, Y. Mozharivskyj, and H. Hillebrecht. $AlFe_{2-x}Co_xB_2$ ($x = 0 - 0.30$): TC Tuning through Co Substitution for a Promising Magnetocaloric Material Realized by Spark Plasma Sintering. *Inorganic Chemistry*, 55(19):9677–9684, 2016.

[10] R. Barua, B.T. Lejeune, B.A. Jensen, L. Ke, R.W. McCallum, M.J. Kramer, and L.H. Lewis. Enhanced room-temperature magnetocaloric effect and tunable magnetic response in Ga-and Ge-substituted $AlFe_2B_2$. *Journal of Alloys and Compounds*, 777:1030–1038, 2019.

[11] J. Cedervall, M.S. Andersson, T. Sarkar, E.K. Delczeg-Czirjak, L. Bergqvist, T.C. Hansen, P. Beran, P. Nordblad, and M. Sahlberg. Magnetic structure of the magnetocaloric compound $AlFe_2B_2$. *Journal of Alloys and Compounds*, 664:784–791, 2016.

[12] L. Ke, B.N. Harmon, and M.J. Kramer. Electronic structure and magnetic properties in T_2AlB_2 (T = Fe, Mn, Cr, Co, and Ni) and their alloys. *Physical Review B*, 95(10):104427, 2017.

[13] J. Cedervall, M.S. Andersson, D. Iuşan, E.K. Delczeg-Czirjak, U. Jansson, P. Nordblad, and M. Sahlberg. Magnetic and mechanical effects of Mn substitutions in $AlFe_2B_2$. *Journal of Magnetism and Magnetic Materials*, 482:54–60, 2019.

[14] D. Potashnikov, E.N. Caspi, A. Pesach, A. Hoser, S. Kota, L. Verger, M.W. Barsoum, I. Felner, A. Keren, and O. Rivin. Magnetic ordering in the nanolaminar ternary Mn_2AlB_2 using neutron and X-ray diffraction. *Journal of Magnetism and Magnetic Materials*, 471:468–474, 2019.

[15] D. Potashnikov, E.N. Caspi, A. Pesach, S. Kota, M. Sokol, L.A. Hanner, M.W. Barsoum, H.A. Evans, A. Eyal, A. Keren, and O. Rivin. Magnetic properties of $(Fe_{1-x}Mn_x)_2AlB_2$ and the impact of substitution on the magnetocaloric effect. *Physical Review Materials*, 4(8):084404, 2020.

[16] V. Franco, J.S. Blázquez, J.J. Ipus, J.Y. Law, L.M. Moreno-Ramírez, and A. Conde. Magnetocaloric effect: From materials research to refrigeration devices. *Progress in Materials Science*, 93:112–232, 2018.

[17] M.W. Barsoum. The $M_{N+1}AX_N$ phases: A new class of solids: Thermodynamically stable nanolaminates. *Progress in Solid State Chemistry*, 28(1–4):201–281, 2000.

[18] M. Sokol, V. Natu, S. Kota, and M.W. Barsoum. On the Chemical Diversity of the MAX Phases. *Trends in Chemistry*, 1(2):210–223, 2019. Special Issue Part Two: Big Questions in Chemistry.

[19] M.W. Barsoum and M. Radovic. Elastic and Mechanical Properties of the MAX Phases. *Annual review of materials research*, 41:195–227, 2011.

[20] M. Naguib, M. Kurtoglu, V. Presser, J. Lu, J. Niu, M. Heon, L. Hultman, Y. Gogotsi, and M.W. Barsoum. Two-Dimensional Nanocrystals Produced by Exfoliation of Ti_3AlC_2. *Advanced Materials*, 23(37):4248–4253, 2011.

[21] Q. Tao, M. Dahlqvist, J. Lu, S. Kota, R. Meshkian, J. Halim, J. Palisaitis, L. Hultman, M.W. Barsoum, P.OÅ. Persson, and J. Rosen. Two-dimensional $Mo_{1.33}C$ MXene with divacancy ordering prepared from parent 3D laminate with in-plane chemical ordering. *Nature communications*, 8(14949):1–7, 2017.

[22] Q. Tao, J. Lu, M. Dahlqvist, A. Mockute, S. Calder, A. Petruhins, R. Meshkian, O. Rivin, D. Potashnikov, E.N. Caspi, H. Shaked, A. Hoser, C. Opagiste, R. Galera, R. Salikhov, U. Wiedwald, C. Ritter, A.R. Wildes, B. Johansson, L. Hultman, M. Farle, M.W. Barsoum, and J. Rosen. Atomically Layered and Ordered Rare-Earth *i*-MAX Phases: A New Class of

Magnetic Quaternary Compounds. *Chemistry of Materials*, 31(7):2476–2485, 2019.

[23] I. Persson, A. El Ghazaly, Q. Tao, J. Halim, S. Kota, V. Darakchieva, J. Palisaitis, M.W. Barsoum, J. Rosen, and P.OÅ. Persson. Tailoring Structure, Composition, and Energy Storage Properties of MXenes from Selective Etching of In-Plane, Chemically Ordered MAX Phases. *Small*, 14(17):1703676, 2018.

[24] D. Potashnikov, E. N. Caspi, A. Pesach, Q. Tao, J. Rosen, D. Sheptyakov, H. A. Evans, C. Ritter, Z. Salman, P. Bonfa, T. Ouisse, M. Barbier, O. Rivin, and A. Keren. Magnetic structure determination of high-moment rare-earth-based laminates. *Phys. Rev. B*, 104(17):174440, 2021.

[25] C. Giacovazzo, H.L. Monaco, F. Viterbo, G. Scordari, G. Gilli, G. Zanotti, and M. Catti. Fundamentals of crystallography. IUCr texts on crystallography no. 2. *Acta Crystallogr. A Found. Crystallogr*, 49:373–374, 1993.

[26] M.S. Dresselhaus, G. Dresselhaus, and A. Jorio. *Group theory: application to the physics of condensed matter*. Springer Science & Business Media, 2007.

[27] C. Kittel. *Introduction to solid state physics*. John Wiley & Sons, New York, 1976.

[28] N.W Ashcroft and D.N. Mermin. *Solid state physics*. Holt, Rinehart and Winston, New York London, 1976.

[29] R. Elliott. *Magnetic properties of rare earth metals*. Springer Science & Business Media, 2013.

[30] A. Narath. Antiferromagnetism in $CoCl_2{\cdot}2H_2O$ I. Magnetic Structure. *Physical Review*, 136(3A):A766, 1964.

[31] A. Narath. Magnetic Properties of $FeCl_2{\cdot}2H_2O$. *Physical Review*, 139(4A):A1221, 1965.

[32] F. Matsubara and S. Inawashiro. Magnetic Properties of Solid Solution $Co_xFe_{1-x}Cl_2{\cdot}2H_2O$. *Journal of the Physical Society of Japan*, 46(6):1740–1747, 1979.

[33] James Samuel Smart. *Effective field theories of magnetism*. Saunders, 1966.

[34] V.K. Pecharsky and K.A. Gschneidner Jr. Magnetocaloric effect and magnetic refrigeration. *Journal of magnetism and magnetic materials*, 200(1–3):44–56, 1999.

[35] A.M. Tishin, K.A. Gschneidner Jr, and V.K. Pecharsky. Magnetocaloric effect and heat capacity in the phase-transition region. *Physical Review B*, 59(1):503, 1999.

[36] D. Sholl and J.A. Steckel. *Density functional theory: a practical introduction*. John Wiley & Sons, 2011.

[37] P. Hohenberg and W. Kohn. Inhomogeneous electron gas. *Physical review*, 136(3B):B864, 1964.

[38] R.G. Parr. Density functional theory of atoms and molecules. In *Horizons of quantum chemistry*, pages 5–15. Springer, 1980.

[39] J.P. Perdew, K. Burke, and M. Ernzerhof. Generalized gradient approximation made simple. *Physical review letters*, 77(18):3865, 1996.

[40] W. Kohn and L.J. Sham. Self-Consistent Equations Including Exchange and Correlation Effects. *Phys. Rev.*, 140:A1133–A1138, 1965.

[41] R.P. Feynman. Forces in Molecules. *Phys. Rev.*, 56:340–343, 1939.

[42] P. Giannozzi et al. QUANTUM ESPRESSO: a modular and open-source software project for quantum simulations of materials. *Journal of physics: Condensed matter*, 21(39):395502, 2009.

[43] A. Auerbach. *Interacting electrons and quantum magnetism*. Springer Science & Business Media, 2012.

[44] C. Lacroix, P. Mendels, and F. Mila. *Introduction to frustrated magnetism: materials, experiments, theory*, volume 164. Springer Science & Business Media, 2011.

[45] J. Als-Nielsen and D. McMorrow. *Elements of modern X-ray physics*. John Wiley & Sons, 2011.

[46] A.J.C. Wilson and V. Geist. International Tables for Crystallography. Volume C: Mathematical, Physical and Chemical Tables, 1993.

[47] V. Franco and B. Dodrill. *Magnetic Measurement Techniques for Materials Characterization*. Springer, 2021.

[48] G.E. Bacon. *Neutron diffraction*. Clarendon Press, 1975.

[49] S.W. Lovesey. Theory of neutron scattering from condensed matter. Vol. 1. Nuclear scattering. 1984.

[50] G.L. Squires. *Introduction to the theory of thermal neutron scattering*. Courier Corporation, 1996.

[51] S.W. Lovesey. Theory of neutron scattering from condensed matter. Vol 2. Polarization effects and magnetic scattering. 1984.

[52] A. Yaouanc and P.D. De Reotier. *Muon spin rotation, relaxation, and resonance: applications to condensed matter*, volume 147. Oxford University Press, 2011.

[53] J. Rodríguez-Carvajal. Recent advances in magnetic structure determination by neutron powder diffraction. *Physica B: Condensed Matter*, 192(1-2):55–69, 1993.

[54] J. Rodríguez-Carvajal. An introduction to the program FullProf. *Laboratoire Leon Brillouin (CEA-CNRS)*, 2001.

[55] L. Vegard. The constitution of the mixed crystals and the filling of space of the atoms. *Zeitschrift Fur Physik*, 5:17–26, 1921.

[56] B.H. Toby. R factors in Rietveld analysis: How good is good enough? *Powder diffraction*, 21(1):67–70, 2006.

[57] T.N. Lamichhane, K. Rana, Q. Lin, S.L. Bud'ko, Y. Furukawa, and P.C. Canfield. Near room temperature antiferromagnetic ordering with a potential low-dimensional magnetism in $AlMn_2B_2$. *Physical Review Materials*, 3(6):064415, 2019.

[58] M. Földeàki, R. Chahine, and T.K. Bose. Magnetic measurements: A powerful tool in magnetic refrigerator design. *Journal of applied physics*, 77(7):3528–3537, 1995.

[59] A. El Boukili, N. Tahiri, E. Salmani, H. Ez-Zahraouy, M. Hamedoun, A. Benyoussef, M. Balli, and O. Mounkachi. Magnetocaloric and cooling properties of the intermetallic compound $AlFe_2B_2$ in an AMR cycle system. *Intermetallics*, 104:84–89, 2019.

[60] Q. Du, G. Chen, W. Yang, Z. Song, M. Hua, H. Du, C. Wang, S. Liu, J. Han, Y. Zhang, et al. Magnetic properties of $AlFe_2B_2$ and $CeMn_2Si_2$ synthesized by melt spinning of stoichiometric compositions. *Japanese Journal of Applied Physics*, 54(5):053003, 2015.

[61] A. Sommerfeld and H. Bethe. Handbuch der physik. *Verlag Julius Springer, Berlin*, 1, 1933.

[62] N.A. De Oliveira and P. J. von Ranke. Theoretical aspects of the magnetocaloric effect. *Physics Reports*, 489(4-5):89–159, 2010.

[63] A.S. Wills. Indexing magnetic structures and crystallographic distortions from powder diffraction: Brillouin zone indexing. *Z. Kirstallogr. Suppl.*, 30:39–44, 2009.

[64] E.F. Bertaut. Representation analysis of magnetic structures. *Acta Crystallographica Section A: Crystal Physics, Diffraction, Theoretical and General Crystallography*, 24(1):217–231, 1968.

[65] A.L. Patterson. The Scherrer formula for X-ray particle size determination. *Physical review*, 56(10):978, 1939.

[66] P. Bonfà, F. Sartori, and R. De Renzi. Efficient and reliable strategy for identifying muon sites based on the double adiabatic approximation. *The Journal of Physical Chemistry C*, 119(8):4278–4285, 2015.

[67] B. Keimer, A. Aharony, A. Auerbach, R.J. Birgeneau, A. Cassanho, Y. Endoh, R.W. Erwin, M.A. Kastner, and G. Shirane. Néel transition and sublattice magnetization of pure and doped La_2CuO_4. *Physical Review B*, 45(13):7430, 1992.

[68] R. Ofer, G. Bazalitsky, A. Kanigel, A. Keren, A. Auerbach, J.S. Lord, and A. Amato. Magnetic analog of the isotope effect in cuprates. *Physical Review B*, 74(22):220508, 2006.

[69] P. Dalmas de Réotier, A. Maisuradze, A. Yaouanc, B. Roessli, A. Amato, D. Andreica, and G. Lapertot. Determination of the zero-field magnetic structure of the helimagnet MnSi at low temperature. *Physical Review B*, 93(14):144419, 2016.

[70] S.M. Disseler. Direct evidence for the all-in/all-out magnetic structure in the pyrochlore iridates from muon spin relaxation. *Physical Review B*, 89(14):140413(R), 2014.

[71] P.G. De Gennes. Interactions indirectes entre couches 4f dans les métaux de terres rares. *Journal de Physique et le Radium*, 23(8-9):510–521, 1962.

[72] D.G. Rancourt, M. Dubé, and P.R.L. Heron. General method for applying mean field theory to disordered magnetic alloys. *Journal of magnetism and magnetic materials*, 125(1-2):39–48, 1993.

תקציר

חומרים מגנטיים פונקציונליים משמשים למספר יישומים שונים החל מאכסון מידע, ספינטרוניקה וכלה בקירור מגנטי. בעתיד, טווח היישומים עלול לגדול וחומרים מגנטיים דו ממדיים יוכלו למצא שימושים כחלק מהטרומבנים מבוססי וון דר וולס (Van der Waals based heterostructures). בעבודה זו, מצבי היסוד המגנטיים והתכונות המגנטיות של שתי משפחות חומרים מגנטיים שכבתיים נחקרות באמצעות בדיקות נפחיות (bulk) ומיקרוסקופיות. כל אחת מהמשפחות שמוצגות בעבודה זו הינה נושא בפני עצמו, כאשר המכנה המשותף לשתיהן הינה שיטת אפיון המבנה המגנטי באמצעות דיפרקציית ניטרונים.

המשפחה הראשונה, הינה משפחת פאזות ה־MAB - קבוצה של בורידים טרנריים עם נוסחה כימית מהסוג $M_2\mathrm{AlB}_2$, כאשר M הינה מתכת מעבר. עניין רב בחומרים אלו התעורר לאחרונה בעקבות גילוי של אפקט מגנטו־כלורי קרוב לטמפרטורת החדר ב־$\mathrm{Fe}_2\mathrm{AlB}_2$. אפקט זה, מוגדר על ידי שינוי הטמפרטורה ΔT של חומר תחת הפעלה של שדה מגנטי H וערכו המרבי מתקבל קרוב לטמפרטורה בה מתרחש מעבר פאזה מגנטי בחומר. בעוד שהתכונות המגנטוכלוריות של $\mathrm{Fe}_2\mathrm{AlB}_2$ כבר היו ידועות, לא היה מספיק מידע ניסיוני על תרכובות $\mathrm{Fe}_2\mathrm{AlB}_2$ שכוללות ערבוב של אטומי הברזל עם אטומי מנגן. חישובים תיאורטיים מבוססי תורת פונקציונל הצפיפות (ctional־ theory ,DFT density fun) נבאו שהוספת מנגן לתרכובת תוסיף אינטרקציות אנטיפרו־מגנטיות ותוריד את טמפרטורת מעבר הפאזה המגנטי של $\mathrm{Fe}_2\mathrm{AlB}_2$.

בעבודה זו, דיאגרמת הפאזות המגנטית של התרכובת $(\mathrm{Fe}_{1-x}\mathrm{Mn}_x)_2\,\mathrm{AlB}_2$ נחקרה באמצעות דיפרקציית ניטרונים ומדידות מגנוט. נמצא כי למערכת שלושה מצבי יסוד שונים בתלות ב־x: מצב פרומגנטי עבור $x \leq 0.1$, מצב אנטיפרומגנטי מוטה (canted antiferrmagonet) עבור $0.1 < x \leq 0.5$ ואנטיפרו־מגנט פשוט עבור $x > 0.5$. דיאגרמת הפאזות במישור x-T משוחזרת באופן איכותי באמצעות חישוב מבוסס על תורת השדה הממוצע. נמצא, כי הוספת Mn לתרכובת מחלישה את האפקט המגנטו־כלורי, אך מרחיבה את טווח

הטמפרטורות שלו ובכך מתאפשרת שליטה ועידון של יכולות הקירור של החומר. מבוא לפאזות ה־MAB מופיע בפרק 1.1 בעוד שהתוצאות מופיעות בפרק 5 יחד עם ניתוחן.

משפחת החומרים השנייה הינה פאזות i-MAX המכילות עפרה נדירה. משפחה זו מורכבת מחומרים קרמיים שכבתיים בעלי הנוסחה הכימית $\left(\mathrm{Mo}_{2/3}\mathrm{RE}_{1/3}\right)_2\mathrm{AlC}$, כאשר RE הינה עפרה נדירה. חומרים אלו הינם חומרים חדשים שהתגלו לאחרונה והינם בעלי פוטנציאל לשמש כחומרי אב לנגזרות דו ממדיות. מטרת עבודה זו הינה לתת אפיון ראשוני לתכונות המגנטיות של חומרים אלו לרבות זיהוי מצב היסוד המגנטי שלהם ולתת ניבוי לחומר בעל הפונציאל לשמש כחומר אב למגנט דו ממדי.

מצבי היסוד המגנטיים עבור $\left(\mathrm{Mo}_{2/3}\mathrm{RE}_{1/3}\right)_2\mathrm{AlC}$ כאשר RE הינו Nd, Tb, Ho ו־Er זוהו כגלי צפיפות ספין אנכיים (transverse spin density wave) באמצעות דיפרקציית ניטרונים על דגמי אבקה, אולם שיטה זו לא ישימה עבור $\mathrm{RE}=\mathrm{Gd}$ מכיוון שהוא בולע ניטרונים חזק. כדי להתגבר על קושי זה, פותחה שיטה חלופית לאפיון המבנה המגנטי של חומר המבוססת על מדידות סיבוב ספין מיואונים (muon spin rotation, μSR). מדידות μSR על אבקות של פאזות ה־i-MAX לרבות $\mathrm{RE}=\mathrm{Gd}$ מראות כי רק כאשר RE הינו Nd או Gd, המומנטים המגנטיים הינם סטטיים בקנה מידה זמני של מספר מיקרושניות. המבנים המגנטיים האפשריים של $\mathrm{RE}=\mathrm{Gd}$ מתקבלים משילוב של התוצאות ממדידות μSR עם חישוב מבוסס DFT עבור אתר המיואון בחומר, אנליזת סימטריה מגנטית ותוצאות של דיפרקציית ניטרונים על חומרים בעלי RE שונה. באמצעות שילוב המידע מכל המדידות על דגמי אבקה, שני מבנים מגנטיים אפשריים נמצאים עבור $\mathrm{RE}=\mathrm{Gd}$ בעלי מומנט מגנטי של $6.5\pm0.5\mu_\mathrm{B}$ בטמפרטורה של $1.5\,\mathrm{K}$. בנוסף, מוצגות מדידות μSR על גבישים יחידים של $\mathrm{RE}=\mathrm{Gd}$ שבוצעו עבור זוויות שונות של הכיוון ההתחלתי של קיטוב המיואון. שיטת מדידה זו אינה שגרתית והייתה נחוצה עקב מגבלות הדגם הגבישי. מדידה זו מוסיפה אילוצים על כיוון המומנטים המגנטיים של אטומי ה־Gd

שלא יכלו להיקבע בדיוק גבוה ממדידות של דגמי אבקה בלבד. ניתוח של תלות המומנט המגנטי בטמפרטורה מניב יחס של $\approx 10^{-9}$ בין אנרגיית האינטרקציה הבין מישורית לבין אנרגיית האינטרקציה בתוך המישור, ובכך $\mathrm{RE} = \mathrm{Gd}$ מזוהה בקירוב כאנטיפרומגנט דו ממדי. מתוצאת אלו, החומר בעל $\mathrm{RE} = \mathrm{Gd}$ מזוהה בתור המועמד המתאים ביותר שיכול לשמש כחומר אב למגנטי דו ממדי בעל מומנט מגנטי גבוה מבין כל חומרי ה־i-MAX שקיימים כיום. הרקע אודות פאזות ה־i-MAX מופיע בפרק 1.2, בעוד שהתוצאות מופיעות בפרק 6 יחד עם ניתוחן.

המחקר נעשה בהנחיית פרופסור עמית קרן בפקולטה לפיזיקה
בטכניון וד"ר אולג ריבין מהקיריה למחקר גרעיני נגב

חלק מהמימון למחקר זה התקבל מקרן פזי

אפיון המצב המגנטי של

מגנטים שכבתיים באמצעות

דיפרקציית ניטרונים ו־μSR

חיבור על מחקר

לשם מילוי חלקי של הדרישות לקבלת התואר מגיסטר
למדעים בפיסיקה

דניאל פוטשניקוב

הוגש לסנט הטכניון ־ מכון טכנולוגי לישראל

שבט התשפ"ב, חיפה, ינואר 2022

אפיון המצב המגנטי של

מגנטים שכבתיים באמצעות

דיפרקציית ניטרונים ו־μSR

דניאל פוטשניקוב